Remote sensing using open-path dual-comb spectroscopy

Kevin C. Cossel[1], Eleanor M. Waxman[1], Esther Baumann[1], Fabrizio R. Giorgetta[1], Sean Coburn[2], Caroline Alden[2], and Brian R. Washburn[3]

[1]Applied Physics Division, NIST, Boulder, CO USA
[2]Department of Engineering, University of Colorado, Boulder, CO USA
[3]Time and Frequency Division, NIST, Boulder, CO USA

Abstract

Open-path dual-comb spectroscopy (DCS) is an emerging technique for long open-path measurements across km-scale paths. It provides both broad spectral coverage over hundreds of wavenumbers with high spectral resolution and negligible instrument lineshape. In this chapter we discuss the principle of open-path DCS; provide an overview of the necessary technology and analysis techniques; review field applications including near-infrared measurements of urban CO_2 emissions, CH_4 emissions from drilling and agricultural operations, measurements to a UAV, and recent measurements of volatile organic compounds in the mid-infrared; and finally provide an outlook especially on how this technique can move to additional spectral regions beyond the near- and mid-infrared.

Contents

1 Introduction **3**
1.1 Long open-path atmospheric measurements . . . 3
1.2 Current techniques . . . 4
1.3 Advantages of open-path DCS . . . 4

2 Open-path DCS technology **5**
2.1 Dual-comb spectroscopy history . . . 5
2.2 Dual-comb spectroscopy principle . . . 6
2.3 Dual-comb sources and spectral coverage . . . 11
2.4 Open-path sensing configuration . . . 13
2.4.1 Telescope design . . . 14
2.4.2 Telescope efficiency . . . 15
2.5 Signal-to-noise (SNR) considerations . . . 16
2.6 Data acquisition and coherent averaging . . . 17
2.7 Extraction of species concentrations . . . 19
2.7.1 Line parameters . . . 20
2.7.2 Spectral fitting of ro-vibrationally resolved species . . . 21
2.7.3 More complex fitting cases . . . 21
2.8 Comparability . . . 23
2.9 Long term operation and field deployment challenges . . . 24

3 Applications **26**
3.1 Emission rate determination . . . 26
3.2 Urban greenhouse gas emissions . . . 28
3.3 Industrial oil & gas methane emissions . . . 30
3.4 DCS with an airborne retroreflector . . . 32
3.5 Agricultural emissions . . . 33
3.6 Volatile organic compound (VOC) measurements . . . 35

4 What is next in DCS based sensing? 38
4.1 Extending the spectral region beyond 1.5 μm and 3 μm 38
4.2 Instrument performance 39
4.3 Data analysis 40
4.4 Summary 40

5 Acronyms 41

1 Introduction

Optical frequency combs are a unique class of lasers that combine the advantages of continuous-wave (cw) laser technology – tight spatial coherence and high spectral resolution – with broadband spectral coverage approaching that of white light lamps [1]. The spectrum of a frequency comb is composed of individual modes or "comb teeth" that behave very much like an array of many thousands to millions of individual, perfectly evenly spaced cw laser lines spanning the entire comb spectrum – typically tens to hundreds of nanometers of bandwidth – all with a high level of mutual phase coherence[1]. Optical frequency combs were originally developed two decades ago to count the cycles of optical atomic clocks [2–6] but have since found their way into a broad field of other applications [7–9]. Their development resulted in one-half of the Nobel Prize in Physics in 2005 [10, 11].

Frequency combs are well-suited for atmospheric sensing, in part because they can probe many atmospheric species simultaneously, covering entire molecular bands at very high spectral resolution. This is illustrated in Figure 1, which shows a broad spectrum before and after gas absorption as well as the underlying closely spaced comb teeth. Additionally, frequency combs are a high brightness, minimally divergent source that can measure integrated gas concentrations over distances exceeding ten kilometers in both daytime and nighttime. In order to preserve the high spectral resolution during data acquisition, the spectrometer needs to resolve each comb tooth. This can be accomplished using a technique called dual-comb spectroscopy (DCS) [12], which uses a second optical frequency comb to read-out the first comb. There exist other techniques to perform spectroscopy using frequency combs, see [13–16] for reviews, but DCS is the only measurement technique so far to have used frequency combs in field environments for long open-path atmospheric measurements, and thus we focus on DCS for the rest of the chapter. We first motivate the use of DCS for open-path spectroscopy, then describe frequency combs and in particular dual frequency comb spectroscopy, including a discussion of hardware components and spectral analysis with a focus on the instruments used by the authors of this chapter. The next section discusses several recent applications of open-path measurements using DCS. The final section looks at potential future improvements in the DCS technology.

1.1 Long open-path atmospheric measurements

A significant advantage of long open-path measurements on the hundreds of meters to kilometers scale is that they also allow for characterization of trace gas emissions from potentially heterogeneous source types including area-sources and multiple distributed sources [17–19]. For example, methane emissions from multiple wells in a square kilometer area can be monitored with a single open-path spectrometer. By integrating signals in a horizontal "atmospheric column", an aggregate signal can be derived, which makes long open-path measurements less likely to miss the plume from a source compared to a point measurement. In particular, point measurements are subject to local or near-field features in emission source characteristics and atmospheric dispersion caused, e.g., by turbulence or buildings. Plumes from point sources can be hard to reliably detect downwind with a point measurement, and semi-stochastic variability in local micrometeorological conditions can make predictability of plume locations problematic. Path-integrated measurements over large distances relax this dimension of uncertainty due to the plume needing only to intersect a portion of the beam path. This enables open-path systems to make continuous measurements of heterogenous sources, which allows for better determination of temporal variability of the sources. Open-path measurements can also be applied to both point and area sources because of the much larger measurement footprint relative to a point sensor (see also Section 3.1) enabling detection of full plumes from area sources.

There are several other advantages to long open-path measurements. First, the long path length provides high precision for trace gas retrievals. This is important for gases such as volatile organic compounds (VOCs), which are present in small quantities, as well as for greenhouse gases (GHGs), which are challenging to measure because their signals are often very small changes on a very large background. For example, a typical enhancement for *in situ* CO_2 measurements in the planetary boundary layer (PBL) could be 2 ppm on a 400 ppm background. Another advantage of open-path measurements is the ability to measure so-called "sticky" molecules. These include species like NH_3 and H_2O which can strongly adhere to sampling

[1]Note that these statements about bandwidth, number of comb modes, and phase coherence strictly only apply to traditional frequency combs based on mode-locked lasers. They do not necessarily apply to newer sources.

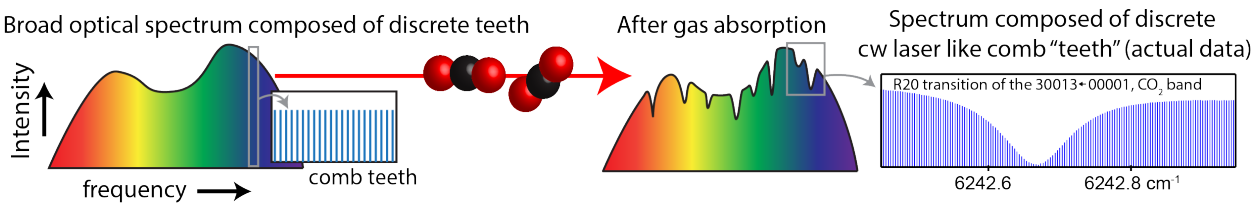

Figure 1: Overview of frequency comb spectroscopy. Light from the comb, made up of tens- to hundreds-of-thousands of individual "comb teeth," passes through a sample resulting in absorption.

tubes via electrostatic and dispersion interactions, potentially introducing biases in retrieved concentrations. Open-path measurements such as the ones described in this chapter do not require a sampling line and thus enable more accurate measurements of these trace gases. Finally, measurements from long open-path sensors are inherently better matched to the resolution of meteorological models, which reduces the representation error of the measurements [20]. The applications described in Section 3 take advantage of one or more of these open path advantages.

1.2 Current techniques

Well-established techniques for long open-path measurements typically fall into two categories: those that use broadband spatially-incoherent light sources, and those that use lasers in very narrow spectral regions. The first category primarily includes Fourier-transform infrared (FTIR) and differential optical absorption spectroscopy (DOAS) spectrometers, which use active incoherent light sources such as a thermal sources or light emitting diode (LED), or passive scattered solar sunlight as the light source. Spatially incoherent light is difficult to send over long distances, especially at eye-safe levels, so open-path FTIR [21–23] and active DOAS [24, 25] measurements are typically limited to a few hundred meters of path length, or require large telescopes and bulky light sources as done in [26]. Spectrometers relying on the sun are only operational during daytime and are typically limited to vertical column measurements rather than horizontal column measurements which make them less well-suited to many of the applications discussed later in the chapter. Tunable laser systems with narrow spectral coverage include differential absorption LIDAR (DIAL) where the laser is first tuned online to the center of a gas absorption line and then offline to a nearby baseline wavelength [27–29], and tunable diode laser absorption spectroscopy (TDLAS) or the related tunable laser dispersion spectroscopy, both of which scan across one or a couple of gas lines, see e.g., [30–35]. These conventional laser systems can be launched over long distances but can only analyze a few carefully chosen absorption lines without adding substantial complexity to the systems, for example an additional laser to measure an additional molecule. Further, to ensure a meaningful gas concentration extraction, wavelength calibration of the instruments is critical, which is unnecessary for DCS instruments (see Section 2.2).

The DCS technique combines the best of the above techniques: it combines broad spectral coverage that can measure entire absorption bands of multiple trace gases simultaneously with spatially coherent light that can be sent over long paths. Open-path DCS is presently used in a monostatic configuration, with a local transceiver and detector and a retro reflector located at some distance from the transceiver/detector which folds the light path back on itself. This is identical to how open-path TDLAS, open-path FTIR, and active DOAS operate and similar to LIDAR-based gas sensing such as DIAL, where the scattered light from a high-power laser is back reflected and collected.

1.3 Advantages of open-path DCS

There are several other advantageous features of DCS that make it optimal for long open-path measurements at an unprecedented high resolution and accuracy[2]. First, as compared to FTIR spectroscopy, the spectral resolution in DCS measurements is not given by the length of a very well-aligned, moving arm, but instead

[2]Typically resolution is determined in part by instrument lineshape. DCS with stabilized comb sources does not add an inherent instrument lineshape, so what matters is the measurement point spacing. When we refer to DCS "resolution", we are referring to this instrument measurement point spacing.

the point spacing for the frequency axis is determined by properties of the frequency comb as discussed more in Section 2.2. This enables dual-comb spectroscopy to have high spectral resolution (for the measurements discussed here, the resolution was usually 200 MHz or 0.0067 cm^{-1}) in a small package – an individual comb is approximately the size of a tablet and the entire system, including electronics, is about the size of a small desk. Further, frequency combs can be built with off-the-shelf all-polarization-maintaining fiber components making them environmentally robust. In fact, fiber-based comb systems have remained mode-locked with sustained 0.5 g acceleration on a shaker table and while being driven around on dirt roads and on a sounding rocket [36, 37].

Another key advantage is that DCS adds no instrument lineshape contribution to the measured absorption feature. For fully stabilized frequency combs, the shape of each comb tooth is essentially a delta function with a width much smaller than the spacing between the individual teeth, as shown in Figures 1 and 8. For example, the systems discussed here have tooth line widths on the order of a kilohertz and tooth spacings of ∼200 MHz. Thus, the comb tooth width is ∼100,000 times narrower than the point spacing. By resolving the absorption at each comb tooth, the DCS instrument lineshape is given just by the comb tooth width and thus is negligible. This can also be seen in [38] where the difference between the spectra from two comb systems shows no instrument line shape residual. In addition, the underlying frequency combs have a frequency axis that is absolutely calibrated against a microwave reference as discussed in Section 2.2. Therefore, it is unnecessary to use an external wavelength calibration such as a line lamp or a solar spectrum.

DCS instruments are also immune to potential systematic effects from atmospheric turbulence because they collect a single shot spectrum at very high temporal resolution – typically a few to ten milliseconds. Of course, for high signal-to-noise ratio (SNR) many of these individual spectra must be added together, so the time resolution is typically on the order of a half-minute to a few minutes. Because the single-shot sampling rate is faster than any turbulence fluctuations, the measured spectrum is not distorted due to intensity changes during the measurement time. This is in contrast to some other open-path techniques, which can suffer from turbulence-induced intensity fluctuations during the time required to obtain a single spectrum.

Finally, the broad spectral coverage enables measurements of many lines from multiple species simultaneously, which minimizes potential spectral interference effects. For example, open-atmosphere measurements are subject to potentially large and rapid shifts in atmospheric water vapor. The ability to directly measure H_2O spectroscopically, with high spectral resolution, means that DCS measurements are less influenced by changes in water vapor concentration. This could happen in other techniques due to crosstalk between spectral features or shifts in the absorption baseline due to changing water lines and thus could result in biases in retrieved trace gas concentrations [39–46].

In summary, open-path DCS combines broad spectral coverage with high accuracy spectroscopy in a stable and precise technique for km-scale, path-integrated measurements. These features make open-path DCS an ideal technique for performing atmospheric trace-gas measurements.

2 Open-path DCS technology

This section gives a short overview of the history of DCS (Section 2.1), then discusses the theory behind DCS (Section 2.2), technical details on light sources (Section 2.3), measurements (Section 2.4), and data acquisition and processing (Sections 2.5 to 2.9).

2.1 Dual-comb spectroscopy history

The concept of DCS was based on similar work in the rf [47] as well as electro-optic sampling techniques in the THz/infrared [48–50]. It was proposed using optical frequency combs in 2001 [51]. Related work using two combs for optical coherence tomography was published concurrently [52]. DCS was first demonstrated in 2003 [53] with a set of unstabilized Ti:sapphire frequency combs. A year later, this setup was used for the first DCS measurement of molecular lines by measuring NH_3 plumes at 800-1100 cm^{-1} from a 22 m stand-off distance with a low spectral resolution of 2 cm^{-1} (∼60 GHz) [54]. Other early work included a demonstration of DCS in the THz region in 2006 based on rectification of Ti:sapphire combs [55]. Further work starting in 2008 demonstrated comb-tooth resolution with high SNR for precision molecular spectroscopy [56] using Er:fiber frequency combs. The same year phase correction of interferograms from DCS was first introduced [57], which

helps to alleviate some of the stringent phase-control and phase-noise requirements. The first high-accuracy line center measurements with DCS were performed in 2010 using Er:fiber combs that were down-converted from 1.5 µm to 3.4 µm using difference frequency generation (DFG) [58]. This highly coherent DCS was demonstrated with an all-fiber approach using amplification and nonlinear broadening in highly nonlinear fibers to cover ∼1400 cm^{-1}(43 THz) of bandwidth in the near-infrared [59].

The first long open-path DCS measurements of GHGs were demonstrated in 2014 using lab-based Er:fiber combs. Over the last six years, open-path DCS has evolved rapidly from this demonstration system to prototype mobile systems in both the near-infrared (NIR) and mid-infrared (MIR) that have been used to identify methane leaks from oil and gas infrastructure and to measure even larger molecules in the atmosphere. DCS has also been used for time-resolved acquisition of reaction kinetics in shock tubes and for hyperspectral imaging. These developments are summarized in Table 1.

There are also a limited number of open-path comb sensing demonstrations relying on a single comb, see for including open-path CH_4 and H_2O at 3.25µm over a 26 meter path using a dispersive spectrometer for detection [72], another demonstration of open-path CH_4 and H_2O at 2.9-3.4 µm from a DFG source over a 3.3-meter path relying on a grating spectrometer for detection [73], and a CH_4, C_2H_6, and H_2O demonstration over an open path of up to 70 meters using an optical parametric oscillator (OPO)-based comb and a Michelson interferometer for detection [74]. Additionally, the combination of a single comb and a CW laser was recently demonstrated for fast and photon efficient CO_2 and HCN sensing [75]. However, all of these demonstrations have substantially lower spectral resolution than what is achievable with a dual-comb spectrometer system.

2.2 Dual-comb spectroscopy principle

At its core, a frequency comb as discussed in this work is a pulsed, mode-locked laser. Figure 2 shows the time-domain (a) and frequency-domain (b) pictures of a such a frequency comb. Comb sources based on other technologies are emerging, see Section 2.3, and do not necessarily behave the same as a frequency comb based on a passively mode-locked laser. In the time domain, a mode-locked laser emits pulses precisely spaced as $T_r = 2L/v_g = 1/f_r$ where L is the length of the cavity, v_g is the pulse group velocity in the cavity and $f_r = 1/T_r$ is the pulse repetition rate. These pulses result from the coherent addition of all of the optical longitudinal modes supported in the laser cavity. The emitted pulses are very short, on the order of 100 femtoseconds, resulting in a broad frequency domain spectrum spanning many THz. Analogous to the time-domain pulse train with a T_r periodicity, the frequency-domain spectrum consists of a series of discrete frequencies or laser modes, called comb teeth, which are separated by the repetition rate $f_r = 1/T_r$. This series of discrete frequencies is what gives rise to the description "comb". Each comb tooth or optical mode frequency ν_n is described by the comb equation:

$$\nu_n = n \cdot f_r + f_0 \tag{1}$$

where the two radio frequencies f_r and $f_0 < f_r$ are the pulse repetition rate and the offset frequency of the first tooth from 0 Hz, respectively, and n is the comb mode number. Because the frequency of each comb tooth is known precisely through equation (1), a comb is essentially a frequency ruler where each comb mode represents a frequency tick similar to a length tick on a length ruler, and it maps the optical frequencies ν_n from the THz domain which are inaccessible to electronics to more manageable rf frequencies (f_0, f_r) in the MHz to GHz domain.

In the absence of any stabilization, f_0 and f_r and thus also ν_n can drift and wander [9]. The key to enabling high frequency accuracy and coherent averaging for broadband spectroscopy is phase noise suppression of the two rf frequencies f_0 and f_r, which results in low-phase-noise, narrow-linewidth individual comb teeth. By stabilizing these two frequencies, the comb is locked and prevented from drifting or from having the spacing between the teeth change. For phase locking, f_0 is usually measured and stabilized by the so-called f-to-$2f$ self-referencing method proposed in 1999 [2, 3]. f_r can either be measured directly with a photodiode or by heterodyning one comb tooth to a frequency-stable cw laser at ν_{cw} as shown in Figure 3c. The offset between ν_{cw} and the comb tooth is locked, thus stabilizing f_r. f_0 and f_r can also be extracted by heterodyning two separate comb teeth against two frequency-stable cw lasers at ν_{cw2} and ν_{cw} [56].

To access the full frequency accuracy of a comb as described by (1) for spectroscopy, one needs a read-out technique to detect and distinguish each comb tooth. As shown in Figure 3, DCS uses two frequency combs

Year/Ref	Comb Architecture	Resolution (MHz)	Averaging time Operation time	Wavelength (μm)	Molecules	Path length (m)	Notes
2005 [54]	Ti:sapph., DFG in GaSe	60 000	70 μs 3.15 s	8.8 - 12	NH_3	44	First open path demonstration
2013 [60]	Er:fiber	100	200 ps 45 min.	1.56	HCN	20	Aerosol backscatter instead of reflector
2014 [61]	Er:fiber	100	5 min. 3 days	1.6	CO_2, CH_4, H_2O, HDO, temperature	2000	First long open-path DCS over folded path to mirror
2015 [62]	Er:fiber	100	5 min. 11 hours	1.6	CO_2, CH_4, H_2O	2000	First phase & ampl. DCS over folded path to mirror
2016 [63]	Er:fiber	200	10-60 sec. 5 hours	1.440	H_2O, CO_2 temperature	7.23	16 MW gas turbine exhaust
2017 [64]	Yb:fiber, OpGaP OPO	102	≥120 ms ≥120 ms	6-12	CH_4, H_2O	2.5	CH_4 in cell, H_2O ambient
2017 [65]	Er:fiber	200	10 sec. 15 min.	1.6	CO_2, CH_4, H_2O	2000	Spectroscopy to a UAV
2017 [38]	Er:fiber	200	30 sec. 2 weeks	1.6	CO_2, CH_4, H_2O HDO, temperature	2000	Intercomparison between two DCS instruments
2018 [66]	Er:fiber	200	2 min. months	1.6	CH_4, H_2O	up to 2200	First field deployed system for regional trace-gas det.
2019 [67]	Er:fiber, DFG in PPLN	200	1 min. 4 hrs. (tot.)	3.2 - 3.6	CH_4, H_2O, VOCs	162 - 2000	MIR measurements over long open paths
2019 [68]	Er:fiber	200	30 sec. 7 weeks	1.6	CO_2, CH_4, H_2O, HDO, temperature	2000 - 6700	Over-city flux measurements
2020 [69]	QCL comb	9 860	4 μs	8.11-8.52	C_3H_4	0.14	Time resolved DCS in shock tube
2020 [70]	EO comb	10 000	1 sec. 7 sec.	1.5	NH_3	1.2	Dual-comb hyperspectral imaging with 5 teeth
2020 [71]	QCL comb	9 720	1 sec. 1 hour	9.9-10.25	Methanol, Ethanol, R134a Acetic acid, Isopropanol	460	Open-path QCL comb

Table 1: Overview of open-path DCS demonstrations.

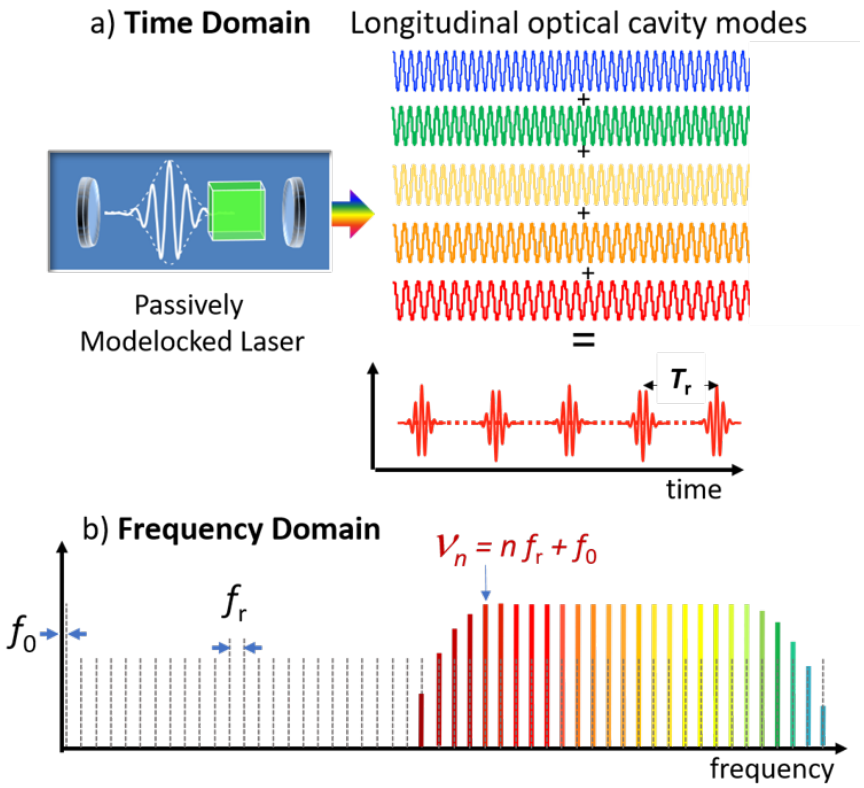

Figure 2: Time and frequency domain picture of an optical frequency comb based on a passively mode-locked laser. a) A non-linear element in an optical laser cavity (schematically depicted in green) acts as a saturable absorber which has higher transmittance at higher optical power. This favors phase-locked addition of all longitudinal optical modes inside the cavity (hence the name mode-locked), resulting in short, high peak power pulses exiting the cavity compared to incoherent modes with low peak power, quasi-cw output. The emitted pulse train has a pulse period $T_r = 1/f_r$, where f_r is the pulse repetition rate. b) The Fourier transform of the time domain pulse train produces the frequency domain comb spectrum. It is composed of a series of evenly-spaced "teeth" separated by f_r. The frequency of each comb tooth ν_n can be calculated by the comb equation (1).

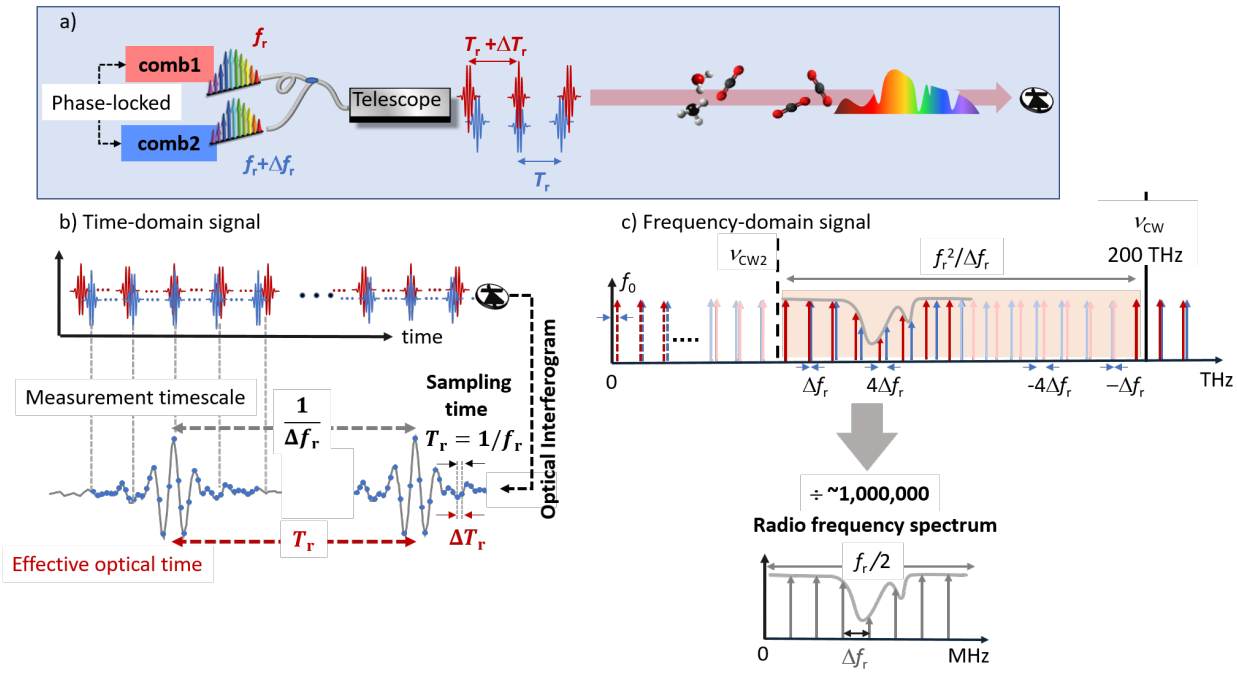

Figure 3: Dual-comb spectroscopy. a) Physical setup for open-path DCS. Two combs are overlapped and light is sent from the combs to a telescope where it is launched through free-space and light is absorbed by trace gases in the atmosphere. The light is detected at the far end of the path with a single photo detector. b) Time domain pictures of the measurement. Pulses with different spacing walk across each other (here, red and blue pulses). The result is an interferogram or cross-correlation of the pulses. The time domain is converted to the frequency domain by a Fourier transform. c) In the frequency domain, each laser produces a comb spectrum with teeth in slightly different locations (red and blue comb teeth). The two combs are phase locked in such a way that they have comb tooth pairs overlapping at multiple places in the spectrum. The spectrum in between these overlapping teeth is sometimes called the Nyquist zone, or twice the unambiguity range, and the spectral region of interest is situated in this unambiguity range (see text for more detail). This is schematically depicted as the lower half of the frequency span between ν_{cw2} and ν_{cw}. The comb tooth pairs between the two combs interfere to produce a beat note that appears at the difference in the comb tooth frequencies, which results in a comb in the rf domain with a spacing of Δf_r. There is a compression factor on the order of 1 million when mapping the optical frequency combs to the rf domain in DCS.

with repetition rates slightly offset by Δf_r to rapidly read out the spectrum with comb-tooth resolution. Similar to an FTIR spectrometer, illuminating a photodetector with overlapped light from both pulse trains results in a voltage proportional to the cross-correlation (the interferogram) between the combs. However, instead of a mechanical Michelson interferometer changing the inter-pulse delay, the DCS interferogram (IGM) is formed by the pulses walking across each other due to the difference in comb repetition rates, as shown in Figure 3b. The update time of the IGM equals one DCS measurement and is $1/\Delta f_r$, which can be orders of magnitudes faster than what is achievable with a scanning moving arm of an FTIR spectrometer. The time offset between the red and blue pulses advances by $\Delta T_r = 1/f_r - 1/(f_r + \Delta f_r) = \Delta f_r / [f_r(f_r + \Delta f_r)]$ every $1/(f_r + \Delta f_r)$, resulting in an effective downsampling of $f_r/\Delta f_r$. This downsampling maps the measurement timescale to the effective time of the optical pulses. In DCS, typical values of $f_r/\Delta f_r$ are around 10^6 (this is also called the "compression factor"), mapping sub-picosecond optical signals to microsecond voltages that can be processed with off-the-shelf MHz-bandwidth photodetectors and electronics.

Another way to understand DCS is to consider the frequency domain as shown in Figure 3c. Here, both combs are self referenced with the f-to-$2f$ scheme. Both combs are also locked to a reference laser at a frequency ν_{cw}; comb 1 at the $(N + \Delta N)$th comb tooth and comb 2 at the Nth tooth:

$$\nu_{cw} = (N + \Delta N) f_r + f_0 = N(f_r + \Delta f_r) + f_0 \quad (2)$$

$$\Delta f_r = f_r \frac{\Delta N}{N} \quad (3)$$

While the two f_0 and two ν_{cw} locks each have a separate rf lock frequency, they are assumed to be equal and drop out for this DCS discussion. Assuming N is an integer multiple of ΔN, this locking conditions forces tooth pairs of comb 1 and 2 spaced by $f_r(N + \Delta N)/\Delta N$ to overlap in frequency. Within the spectral region between two adjacent tooth overlaps, the distance between adjacent comb 1,2 tooth pairs increases by Δf_r, resulting in an rf comb with teeth separated by Δf_r after square-law photodetection as shown in Figure 3c.

One major feature of DCS is that there is a one-to-one amplitude and phase correspondence between detected rf comb teeth spanning some MHz and optical comb teeth spanning multiple THz, fully preserving the exquisite frequency accuracy of the frequency combs. To achieve this unambiguous mapping between one rf comb tooth and a specific pair of optical comb teeth, the comb-mode-number difference between adjacent optical teeth must be constant across the measured optical spectrum. In general, one cannot distinguish between positive rf frequencies (comb 2 tooth frequency > comb 1 tooth frequency) and negative rf frequencies (comb 2 tooth frequency < comb 1 tooth frequency); therefore the spectrum has to be restricted to half of the region between overlapping comb teeth for unambiguous mapping. This is shown in Figure 3c as the lower half of spectral region between overlapped comb teeth adjacent to ν_{cw2} and ν_{cw}. This spectral span is often referred to as the unambiguity range and equals $f_r(N + \Delta N)/(2\Delta N) = f_r(f_r + \Delta f_r)/(2\Delta f_r) \approx f_r^2/(2\Delta f_r)$ in the optical frequency domain. In the rf domain, this corresponds to $f_r/2$, or the Nyquist frequency for a sampling frequency f_r. This is why the unambiguity range is also sometimes referred to as Nyquist zone. While not discussed here, tuning the lock frequencies can be used to fine tune the Nyquist zone to overlap precisely with the optical span of interest [76].

More precisely, the amplitude of each rf comb tooth corresponds to the geometric mean of the two adjacent optical teeth's amplitude and the rf comb tooth phase corresponds to the optical teeth's phase difference. The optical frequency ν_{opt} of two individual optical comb teeth is calculated from the corresponding rf comb tooth's frequency f_{rf} through

$$\nu_{opt} = p \times f_r \frac{f_r + \Delta f_r}{\Delta f_r} + \frac{f_r}{\Delta f_r} \times f_{\mathrm{rf}} \quad (4)$$

where p is an integer that is determined through a-priori knowledge of the spectrum's location (it is sufficient to know the spectral location to within $f_r^2/\Delta f_r$, typically tens of THz) [77].

For all of the open-path DCS applications discussed here, robust fiber frequency combs were used with f_r usually $\approx 200\,\mathrm{MHz}$ [78, 79]. These combs are referenced to either a kHz-linewidth cw laser or an rf reference, resulting in teeth-lineshapes $\sim$100,000$\times$ narrower than the $\sim$200 MHz or $0.0067\,\mathrm{cm}^{-1}$ spacing between comb teeth. The difference in repetition rate and thus the measurement rate is usually on the order of of 100 Hz to kHz, resulting in a spectral coverage (or Nyquist zone) of $f_r^2/(2\Delta f_r)$ between 20 THz to 200 THz and a downsampling factor $N/\Delta N = f_r/\Delta f_r$ of up to millions.

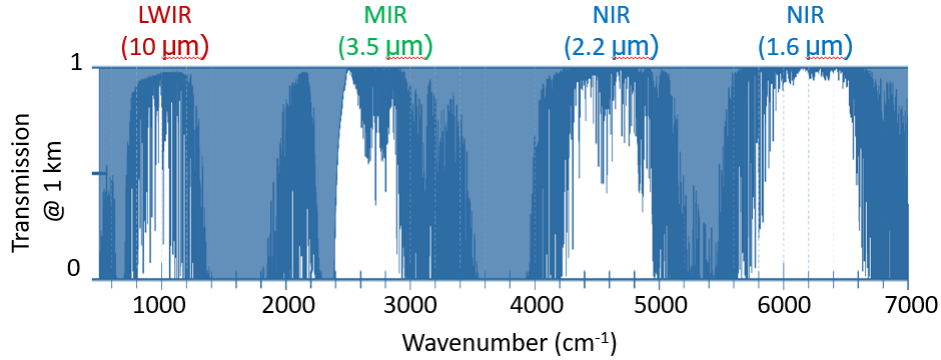

Figure 4: Simulated atmospheric transmission in the near- and mid-infrared for a 1-km-long open-air path. The main transmission windows are indicated: NIR, near-infared; MIR, mid-infrared; LWIR, long-wave infrared.

2.3 Dual-comb sources and spectral coverage

The laser used to create the comb is the most fundamental part of the DCS system. The choice of laser determines, among other things, the wavelength region in which measurements can be made. In the lab, the molecular absorption region of the target species determines the choice of laser, but in open-path measurements the atmospheric absorption of other gases, such as H_2O, must also be considered as illustrated in Figure 4. This figure shows the simulated atmospheric transmission of a ∼1 km free-space open path. The shaded regions represent regions of low transmission where atmospheric gas species, mostly water but also CO_2 and CH_4, absorb the light. Regions with few absorbers and thus relatively high transmission are called atmospheric windows and four of these are labeled in Figure 4. In the NIR, where comb sources are readily available, mostly GHGs such as CO_2 and CH_4 and their isotopes can be targeted. To measure less prevalent trace gases at lower concentrations, such as VOCs, a source situated at longer wavelengths in the MIR or long-wave infrared (LWIR) is necessary to target the much stronger fundamental ro-vibrational bands. In addition, not shown, there is a window in the visible to UV that provides access to strong electronic transitions in some molecules and is used in DOAS [25].

At the time of writing, dual-comb sources are available spanning significant swaths of the NIR, MIR, and LWIR spectral range [59, 80–83], but to date no single source is a comprehensive solution to every spectroscopic problem. While most atmospheric DCS sensing has relied on mode-locked Er:fiber lasers [84], there are a large array of frequency comb platforms that might also be attractive for such work. However, many of these sources are still being developed and are not yet robust enough for field deployment. In addition, the trade-space in terms of mode spacing, spectral coverage, total power, and noise performance for these platforms can be complicated. A long discussion of these platforms can be found in [12] and [9], which we will summarize here.

Mode-locked laser frequency combs based on solid-state lasers or fiber lasers have long been the workhorses of the frequency comb world. These systems have several features that are attractive for spectroscopy such as high coherence – allowing for long averaging times – and a typical tooth spacing of 100 MHz - 1 GHz, which is nicely matched to the few-GHz collisionally-broadened atmospheric absorption lines of small molecules. Er:fiber-based frequency combs, emitting in the telecommunication band around 1550 nm are the most common mode-locked laser source for open-path DCS. This is largely driven by the fact that Er:fiber systems strongly leverage the massive industrial investment in fiber communications and the favorable dispersion of silica glass at these wavelengths, giving them a significant edge in technological maturity [37, 78, 85]. However, Yb:fiber lasers around 1 µm and Tm:fiber lasers near 2 µm allow access to higher powers and different wavelength bands and may become more common as the technology advances [86–88]. Another possibility for generating a high power frequency comb at 2 µm is to combine an Er:fiber laser with amplification in Tm:fiber [89]. Several solid-state frequency combs exist including Ti:sapphire, which cover the 600-1000 nm range [90–92], and Cr:ZnSe and Cr:ZnS lasers, which produce frequency combs around 2.4 µm [93–95]; however, these lasers have free-space cavities, which make them more difficult to use for field

applications.

Additionally, the high peak powers possible with mode-locked lasers allows for efficient non-linear wavelength conversion. The spectral coverage of Er:fiber lasers can be extended via supercontinuum generation in non-linear fiber to cover any wavelength from 1 µm to 2 µm [59, 80] or in new integrated photonic platforms [96, 97] allowing even broader spectral coverage. To access longer wavelengths mode-locked lasers can be used to drive frequency conversion based on DFGs [83, 98, 99] or optical parametric oscillators [64, 81, 100–102] and allow for DCS with octave spanning (or greater) spectra anywhere from 1 µm to 25 µm.

Recently, a number of potentially more compact comb sources have emerged which are based on electro-optic (EO) modulators, semiconductor diodes, and microresonators. These sources are attractive for reducing the size, weight, and power (SWaP) of DCS systems. The most well-developed of these are based on quantum cascade laser (QCL) [103–106] and inter-band cascade laser (ICL) [107] frequency combs. These chip-based semiconductor sources emit high-power light in the MIR, LWIR, and THz without requiring a pump laser such as is used in DFG. They are also compact, robust, and commercially available. However, the bandwidth of these devices ($< 100\,\mathrm{cm}^{-1}$) combined with the large tooth spacing ($\sim$10 GHz or $0.33\,\mathrm{cm}^{-1}$) leads to $\sim$100 comb modes with sufficient SNR instead of the $\sim$100,000 available from a traditional mode-locked laser source. This combination of bandwidth and tooth spacing can be limiting for many atmospheric applications, but the relative simplicity of the technology may more than outweigh the negatives for some applications. For example, the large tooth spacing of these devices coupled with the high powers allows for impressively fast measurement times, which can provide information about dynamic events [69, 108]. QCL and ICL combs also have higher phase noise than mode-locked laser systems but increasingly this noise can be mitigated by digital correction techniques [109, 110].

Another type of semiconductor platform based on integrated external-cavity surface-emitting lasers (VECSELs and MIXSELs) [111] have recently been demonstrated for DCS [112]. Like other mode-locked systems these devices can have two offset combs sharing a single cavity, which mitigates much of the mutual phase noise between combs. Bandwidth is again quite limited but in principle the MIXSELs could be designed for many different wavelengths potentially allowing a MIXSEL system to effectively target a specific molecule with a compact robust sensor.

EO-based combs, which use EO modulation of a cw laser, are also emerging as an interesting source for DCS [113–117]. These systems have the significant advantage that the same cw laser can be used for both combs ensuring a high level of coherence between combs. Additionally the tooth spacing of these systems can be dynamically tuned from 10s of GHz to 1 MHz, agility that would be impossible in a mode-locked laser [113]. This control can even allow for acquisition (and imaging) on a very slow detector such as a camera [70]. The principal downside of EO combs is the challenge of generating a broad optical spectrum, which currently requires multiple stages of amplification, filtering, and pulse compression to generate an octave-spanning spectrum [118]. This added complexity results in a system with larger SWaP than an Er:fiber-comb-based system. Typical spectra without significant amplification are limited to tens of nanometers in the telecom region where state-of-the-art EO modulators are available. Non-linear conversion to the MIR is also possible but the bandwidth is again limited [119]. This limited bandwidth is a disadvantage in relation to the number of detectable species, but it is an advantage for speed. EO-DCS can be performed on the millisecond time scale with coherent averaging in the laboratory [120, 121]. The flexibility and potential reliability of these systems suggest that they will find an application space [122].

Finally, microresonator-based frequency combs rely on a cw laser coupled to a high-finesse resonator to drive non-linear frequency comb generation via the Kerr effect [123, 124] and have been demonstrated from the NIR [125] to the MIR [126]. These sources have the potential to provide compact, chip-scale frequency combs, but they face a challenging integration problem in order to couple the cw laser to the resonator and typically require a high power pump laser to generate sufficient comb power. In addition, their output comb power is typically quite limited and might not be sufficient for open-path measurements without additional external amplification, which increases the system SWaP. These comb sources can also have significant noise unless care is taken to achieve a quiet, mode-locked soliton state [123, 127]. Thus, there are relatively few dual-comb demonstrations [128–132]. As with the QCL and ICL combs, these systems work better at higher tooth spacing (10 GHz - 1 THz) and often have limited spectral bandwidth, leading to typically 10-100 comb modes available for spectroscopy.

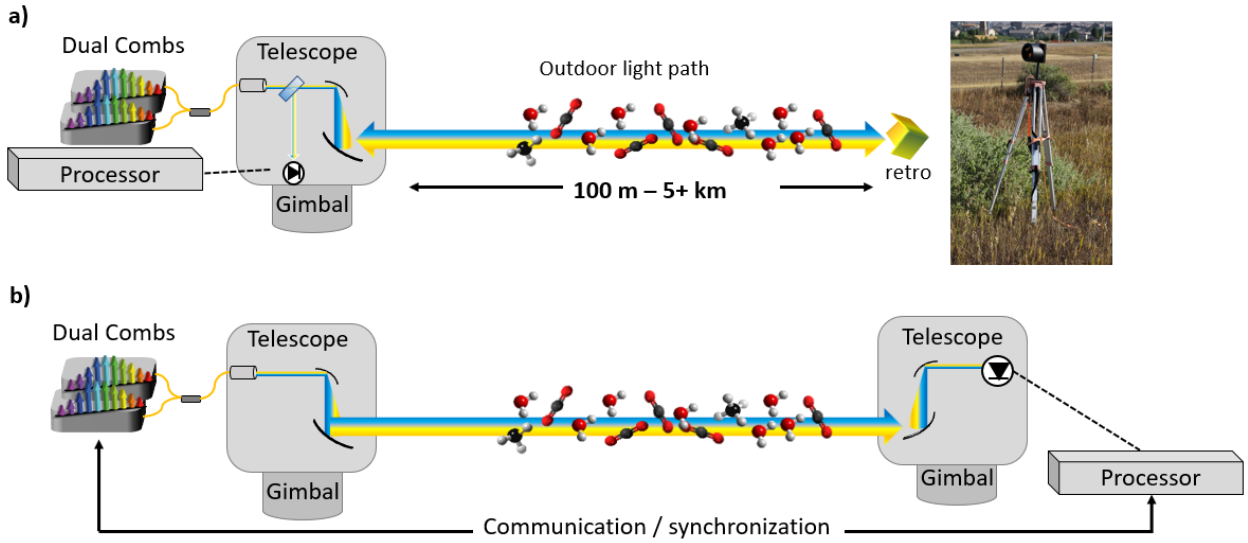

Figure 5: Open-path DCS in a a) monostatic and b) bistatic configuration.

2.4 Open-path sensing configuration

Open-path DCS requires a dual-comb spectrometer, telescope and detector systems, and an open-air path. To perform DCS, the combs can be combined either before or after the sample (here, the open-air path) but before the photodetector in either case, as shown in [12]. The case where both combs are combined before probing the atmosphere is shown in Figure 3. Combining the combs before the open-air path only allows absorption data to be collected but not phase data; however, it is often substantially easier to implement. In addition, when combining the combs on a beam splitter, two branches of light are produced. If one wishes to use two beam paths, for example measuring upwind and downwind of an emissions source, combining the combs prior to probing the sample conveniently provides light for each path. Further, the atmospheric path introduces both phase noise and beam breakup. Thus, combining the comb light as early as possible is advantageous as phase noise that is common to both combs does not degrade the measurement, and any beam breakup is common and therefore does not affect the spatial overlap between the two combs, which is required for heterodyne detection. On the other hand, if only a single comb is sent over the air, both the absorption and phase of the sample can be retrieved [62], which could potentially provide unique sensing opportunities. Another potential advantage of only sending one comb could be in the case of high-loss paths (for example, very long distance). Because the heterodyne signal power is proportional to $\sqrt{I_1 I_2}$, where I is the intensity of each comb, the SNR can be improved by having a high-power local oscillator comb. However, since I is limited to some I_{max} by detector saturation effects, the SNR is optimum if $I_1 \approx I_2 \approx I_{max}/2$; thus, if the losses from open-air propagation are not too large, combining both combs will provide a higher SNR.

The basic monostatic measurement configuration is shown in Figure 5a, with the comb system and telescope on the left and the retroreflector on the right. Figures 3a and 5b show the equivalent bistatic setup; however, this setup has not yet been used for open-path DCS due to challenges associated with coherent averaging (see Section 2.6) using a processing system spatially separated from the comb system. DCS instruments perform path-integrated measurements with relatively low powers at eye-safe levels (e.g. $< 10\,\mathrm{mW}$ typically). Despite the low light levels a reflective element that folds the optical path back enables interrogation of optical paths of hundreds of meters to tens of kilometers. Although the initial demonstrations used a flat mirror as the reflector [61, 62], it is common to use a corner-cube retroreflector, which reflects incoming light back to the source regardless of the angle of incidence. The use of a retroreflector significantly simplifies the setup because no active control of the retroreflector is necessary in contrast to a plane mirror. The use of a retroreflector also eliminates beam steering effects due to turbulence, which thus reduces the bandwidth required to servo the telescope pointing. Preliminary work based on EO-modulator combs for CO_2 sensing has also been carried out in the NIR looking at comb light back scattered from a natural target

[133].

Beyond these requirements, there is substantial flexibility in the measurement paths for a system. DCS can be used with a single path to obtain path-averaged concentrations for a particular area [61, 62, 67, 72], or can use two paths with separate telescopes to measure upwind and downwind of an emissions source [68]. A single telescope system can also be used to measure many paths to different retroreflectors in sequence to locate an emissions source [66, 134], and the retroreflector can be located on a unmanned aerial vehicle (UAV) for spatial scanning [65]. Examples of each of these setups are discussed in Section 3.

One important consideration is the desired path length because this in turn dictates the required launch aperture size, receive aperture size, and pointing requirements. Selecting a path length is a balance between many factors including line absorption strength, return signal, and desired scientific objectives. For example, in the NIR line strengths tend to be quite weak as these are from overtone bands. Therefore, long path lengths on the order of kilometers are helpful as they increase the interaction length between the light and the target molecules. However, these long kilometer-scale path lengths have low return power and are influenced more by atmospheric turbulence. In order to achieve these path lengths, comb launch power can be increased, though not infinitely, as it results in worsened SWaP due to the necessity of extra amplifier pump diodes, and can reach hard limits for eye safe light launch. Additionally, retroreflectors can be increased in size or retroreflector arrays can be used though with substantial increased cost, and telescopes can be made larger for increased return apertures though again at the cost of worsened SWaP and maneuverability.

In the MIR, line strengths are typically a factor of 100 stronger because this region probes fundamental ro-vibrational bands. This means that path lengths can be shorter and launched optical power can be lower. This is helpful because at present, MIR optics are less efficient than NIR components, leading to higher light losses in MIR systems. However, the line strengths are so strong that one-way path lengths beyond about 1 km can result in total light attenuation due to absorption by H_2O, CO_2, or CH_4 (depending on the spectral region, see also Figure 4). Looking in between these saturated lines for weaker absorbers can be very challenging.

Physical constraints such as weather conditions, geography, and site access permissions can also dictate path selection. One of the most important weather conditions is predominant wind direction. It is often desired to set up paths both upwind and downwind of potential sources and the selection of upwind and downwind requires knowledge of local wind data. Geography is important because DCS requires line-of-sight between the telescope and retroreflector. Further, highly local geography can influence airflow patterns and thus help determine the location of the downwind measurement path. Site access is an additional consideration for permissions as well as ease of troubleshooting the system in the field.

Finally, the choice of path length must depend not only on physical system parameters and light attenuation but also on the science problem. Several applications of DCS are discussed in Section 3, and different path lengths are needed for these problems. For example, one application is the quantification of urban GHG emissions on the city scale (Section 3.2). Cities are typically several to tens of kilometers across, so measuring trace gases across an entire city must be at the multi-kilometer scale, not the tens or hundreds of meters scale. However, emissions from oil and natural gas (Section 3.3) are typically very localized and measurements at the kilometer or hundred meter scale can be used to quantify such emissions. For vertical column measurements, several length scales are relevant. Close to sources, the plume only mixes up to 10s or 100 m, so <1 km path lengths can still be used. For applications such as urban GHG emissions quantification, it would be useful to measure trace gases up to the top of the PBL, which can be at least several km during summer days. Finally, vertical column measurements could potentially be performed into the stratosphere, which would necessitate path lengths of > 10 km.

2.4.1 Telescope design

A key component of open-path DCS systems is the launch/receive telescope system. This system should be optimized to maximize total efficiency so that the launched power can be minimized, which is beneficial in order to simplify the laser systems and also to keep the launched power at eye-safe levels below the ANSI Class 1 limit. Several factors need to be taken into account when designing the telescope system including desired spectral coverage, total path length, retroreflector size, and weight. Often, the best telescope system for one application is not necessarily the best for other applications. Several telescope designs are shown in Figure 6. These designs all use reflective optics, such as spherical mirrors or OAPs, instead of lenses in

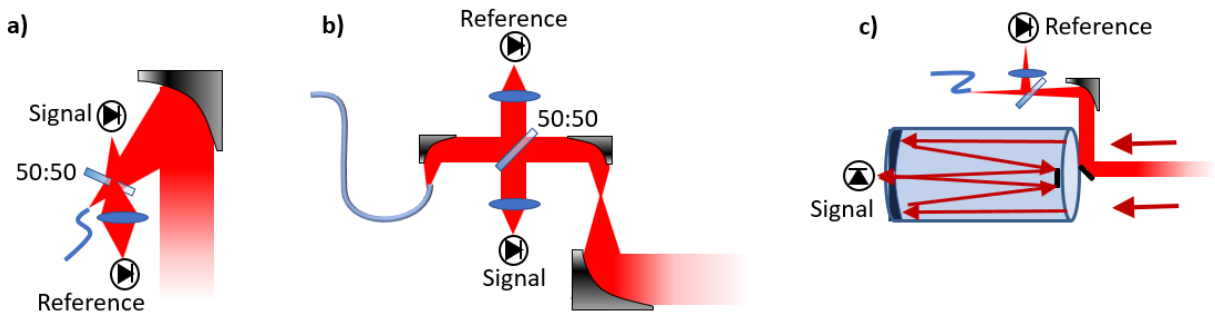

Figure 6: Several telescope designs used for open-path DCS. In all of these designs, the locations of the signal photodetector and optional reference photodetector are given. a) Single OAP design. Light is launched directly out of fiber, passes through a 50:50 beamsplitter, and is collimated by an OAP. Return light traces the same path, except is reflected off of the beamsplitter to a photodetector at the focus of the OAP. b) OAP beam expander. Light is first collimated, passes through the 50:50 beamsplitter, and is expanded by a pair of OAPs. Return light traces the same path, except is reflected off of the beamsplitter and is focused with an additional lens onto a photodetector. c) Modified commercial telescope. This design uses a commercial Ritchey-Chrétien telescope as the receiver optics. Because these telescopes (and similar designs) have a center occlusion from the secondary mirror, this area can be used for the launch optics without additional loss of power. To do this, the launch light is collimated, for example, with an OAP, and then is co-aligned along the center axis of the receive telescope using steering mirrors. A few-percent pickoff can be added in the launch for a reference measurement. The return light is collected by the commercial telescope and measured on a photodetector at the focus of the telescope.

order to avoid chromatic aberrations. This is important if the desired spectral coverage is greater than a few percent of the central wavelength. The use of all reflective optics also enables visible and/or NIR laser light to be used for alignment. However, alignment of OAPs, especially beam expanders, can be somewhat tricky. In addition, these designs show an optional reference detector, which can be used to normalize the measured transmission spectrum. However, for this to be useful, care must be taken to match the signal and reference spectra as much as possible. For this, it is best to have as few optics as possible in the light path between the signal and reference detectors and to reduce polarization sensitivity in the optics or to control the polarization of the light after the fiber.

In the design shown in Figure 6a, the launched beam size is set by the focal length of the OAP and is given by $2(\mathsf{NA})/(\mathsf{EFL})$, where NA is the numerical aperture of the fiber (typically around 0.1-0.2) and EFL is the effective focal length of the OAP. This design is simple and compact, but the use of a 50:50 beamsplitter results in a factor-of-4 loss. The design in Figure 6b adds a beam expander using a pair of OAPs, which provides some flexibility in the size of the launched beam because the initial collimated beam size and expansion ratio can both be varied. The fact that the laser beam is collimated in part of the telescope also provides some additional flexibility to add additional optics. For example, the 50:50 beamsplitter can be replaced with a polarizing beamsplitter and $\lambda/4$-waveplate to reduce the loss from the beamsplitter at the cost of additional complexity and the potential for etalons due to stray reflections. However, the alignment of the beam expander in particular can be challenging. The final design, shown in Figure 6c, differs from the other designs in that the launch and receive optics are decoupled from each other. This design allows for large collection apertures (⌀25.4 cm and ⌀30.5 cm are commercially available) and does not suffer from the inherent loss due to the 50:50 beamsplitter. However, the launch and receive optics need to be carefully co-aligned and can drift relative to each other due to, e.g., temperature changes. Another disadvantage of the large diameter telescopes is that they are heavy, which adds to the requirements for the pointing stage.

2.4.2 Telescope efficiency

As discussed in Section 2.5, it is typically desirable to collect ∼10-100 μW of power on the signal detector, depending on the detector. If we assume that ∼10 mW of light is launched (this corresponds to the ANSI

Class I limit for light > 1400 nm), then the total efficiency of the system from launch to receive needs to be $0.1 - 1\%$. In order to calculate the expected efficiency, it is necessary to fully model the Gaussian beam propagation and turbulence effects in the atmosphere [135–139]. However, in many cases the distance to the reflector is large compared to the Rayleigh range of the launched beam, in which case the beam size versus distance can be determined from the divergence angle (θ): $\theta = \frac{\lambda}{\pi w}$, where θ is the divergence relative to beam center, w is the beam waist ($1/e^2$ intensity radius), and λ is the wavelength. In addition, typically it is sufficient to estimate the average power, so the turbulence effects can be approximated as an additional long-term beam spread. With these assumptions, the total efficiency (E_t) can be estimated using an equation developed for laser ranging [139, 140]. Of particular note, the efficiency in this case increases with the square of the launched beam size and receive aperture diameter and increases with the fourth-power of the retroreflector diameter. The efficiency also decreases with the fourth power of the distance to the reflector. These scaling factors are only valid as long as the beam at the retroreflector and receiver is larger than retroreflector and receiver diameter, respectively. In practice, for kilometer-scale path lengths and moderate turbulence, a launched beam diameter of ∼10 cm (corresponding to a divergence angle of 10 µrad), collection aperture of ∼20 cm, and a ∼10 cm diameter retroreflector will give efficiencies of typically $1 - 10$ %.

2.5 Signal-to-noise (SNR) considerations

Open-path DCS has many of the same SNR considerations as DCS in general, see e.g. [141] and [12], and also has many of the same considerations as Fourier-transform spectroscopy (FTS) (see e.g. [142]). Because DCS relies on acquisition in the time-domain as opposed to frequency-domain multiplexing (e.g. using a dispersive spectrometer), the SNR of the magnitude spectrum which corresponds to the optical power spectrum is reduced from the temporal IGM SNR by the number of acquired spectral elements $M = \Delta\nu/f_r$ encompassed within the spectral bandwidth of the source, $\Delta\nu$ [141]. To understand this better, consider a time-domain measurement of a series of IGMs with a total of N points in the time series and a sampling rate of f_r. The discrete Fourier transform (DFT) of this time series has a measurement bandwidth of $1/N$ (in units of Nyquist frequency), so the spectral-domain noise σ_f can be related to the time-domain noise σ_t by $\sigma_f = \sigma_t\sqrt{N}$. On the other hand, the spectral-domain signal s_f (i.e., the height of a comb tooth after the DFT) is related to the time-domain signal s_t (given by the peak height of the IGM) by $s_f = s_t\frac{N}{M}$, where M is the number of spectral elements (comb teeth). Defining the SNR as $\mathrm{SNR} = \frac{s}{\sigma}$ and noting that $\frac{N}{f_r} = t_{\mathrm{meas}}$, where t_{meas} is the total measurement time, we can relate the frequency-domain SNR to the time-doman SNR:

$$\frac{\mathrm{SNR}_f}{\sqrt{t_{\mathrm{meas}}}} = \sqrt{f_r} \times \frac{\mathrm{SNR}_t}{M \times \beta}. \tag{5}$$

Here SNR_f is defined as the average frequency-domain SNR assuming a Gaussian spectrum. The proportionality constant β accounts for spectral chirp in the IGMs (i.e., different wavelengths occur at different times), which reduces the temporal SNR_t relative to the unchirped case without affecting the spectral SNR_f. If the IGMs are chirped, $\beta < 1$. If they are not chirped, $\beta = 1$. Note that Equation (5) requires the dual-comb tooth linewidth to be narrower than $1/t_{\mathrm{meas}}$, which is usually achieved with real-time or post-processing phase correction (see also section 2.6). To account for the dependence on M when comparing systems, it is often worthwhile to define a figure of merit (FOM)

$$\mathrm{FOM} = \frac{\mathrm{SNR}_f}{\sqrt{t_{\mathrm{meas}}}} \times M. \tag{6}$$

Typical FOM values range from 10^6 - 10^7 [12].

There are several limits to the attainable SNR. Figure 7 shows the achievable FOM versus optical power due to different noise sources. At very low measured optical powers, the SNR is typically limited by detector noise, given by the detector noise-equivalent power (NEP). In this case, the SNR scales linearly with increasing optical power. Because the detectors used for DCS often have a large rf bandwidth (in order to measure a broad spectrum), the NEP is typically limited by the transimpedance amplifier and not the noise of the photodiode itself. The NEP of 100-MHz-bandwidth InGaAs and extended InGaAs photodetectors in the 1.0-2.5 µm spectral region is typically on the order of 1-10 pW/Hz$^{1/2}$. In the MIR region, detectors are a bit worse; however, thermoelectrically cooled photovoltaic HgCdTe detectors are available in the 3-5 µm

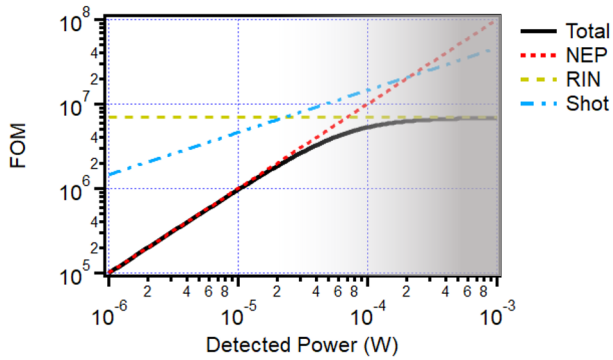

Figure 7: FOM versus detected power. The FOM is shown by the solid line, limiting cases are shown by broken lines. The detector noise is set at 10 pW/Hz$^{1/2}$ and the RIN is −140 dBc/Hz. The grey shading indicates the region where detector saturation effects occur (more shading indicates more potential effects). More details can be found in [141] and [12]

.

spectral region with an NEP of ∼15 pW/Hz$^{1/2}$. On the other hand, avalanche photodiodes (APDs) have significantly lower noise but at the cost of significantly lower saturation power.

As the optical power on the detector is increased, other noise sources dominate over the detector NEP. These include fundamental shot noise and laser relative intensity noise (RIN), which arises from fast (pulse-to-pulse) intensity noise in the combs. The RIN varies between laser systems (even ones with similar designs) and can be difficult to reduce. In addition, spectral broadening or other nonlinear processes can often result in increased RIN. Once the RIN limit is reached, the SNR remains constant with increasing optical power on the detector. Figure 7 shows the RIN limit for a typical level of −140 dBc/Hz, which results in a RIN-limited FOM of around 7×10^6. In principle, it is possible to cancel noise from RIN with balanced detection and reach FOM values $> 10^7$. This has been demonstrated in lab DCS measurements [59, 79, 80, 143]; however, this is complicated to accomplish for open-path DCS because of the required polarization elements and challenges associated with beam overlap.

Unfortunately, even for negligible RIN, it is not possible to increase the SNR by increasing the power on the detector indefinitely. In addition to the obvious limit of received laser power, there are inherent dynamic range limitations in the detection electronics. One potential limitation is the bit depth of the analog-to-digital converter (ADC); however, even for a 12-bit ADC, the ADC-limited FOM is $> 2 \times 10^7$ so is unlikely to be the primary limitation. Another source of dynamic range limitation is saturation, which is used here broadly for a nonlinear response versus input signal. Saturation can potentially arise in the photodetector as well as subsequent rf amplifiers and can result in mixing between comb teeth, the appearance of harmonics in the rf spectrum, and structure in the spectral baseline. These effects in turn result in distortion of the spectral lineshapes, which cause biases in the retrieved concentrations. As indicated by the shading in Figure 7, saturation does not occur only above a well-defined power level, even for a specific detector/amplifier configuration. Instead, the effects of saturation become progressively stronger at higher powers. Thus, the power level at which saturation becomes problematic depends on both the detector and amplifier configuration and also on the requirements of the particular application. For some applications, adding a small bias by running with some amount of detector saturation is acceptable for the increase in SNR. Because of this, it is best to characterize the saturation behavior of a system first before using it in an application. In general, commercially-available detectors in the NIR and MIR start to suffer from saturation around 20-200 μW.

2.6 Data acquisition and coherent averaging

As discussed in Section 2.2, the voltage signal resulting from superimposing both frequency combs on a photodiode is a series of interferograms which repeat every $1/\Delta f_r$ seconds (see Figure 3). The IGM is proportional to the cross-correlation between the electric field of both comb pulses. According to the Wiener-

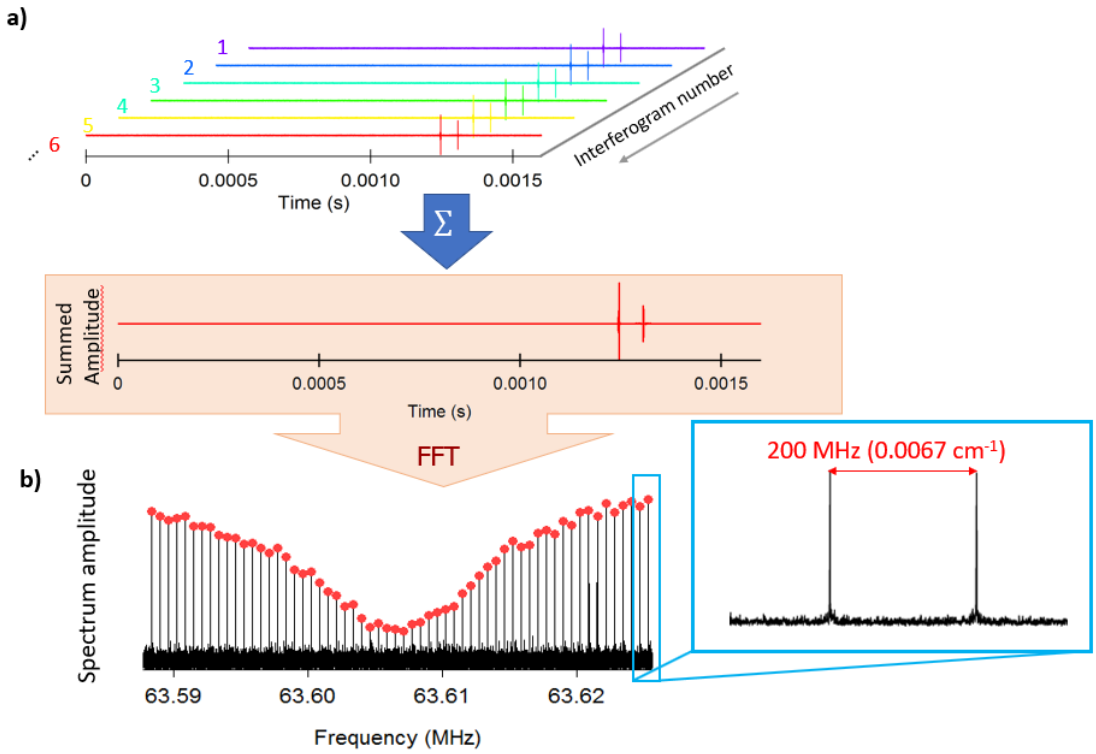

Figure 8: Illustration of coherent averaging of DCS interferograms. a) In the time domain, successive IGMs are summed to produce a single interferogram with higher SNR. b) In the frequency domain, coherent averaging results in a spectrum sampled just at each tooth. Here black is the spectrum with resolved teeth obtained by Fourier transforming a time series consisting of many IGMs and the red points are obtained by Fourier transforming the coherently averaged IGM. The inset on the right shows a zoom on two of the lines illustrating the negligible instrument lineshape.

Khintchin theorem, the Fourier transform of the IGM results in a spectrum which is proportional to the product of both comb spectra. This is analogous to an FTIR instrument, where the temporal cross-correlation of a light source is usually generated with a Michelson interferometer.

To obtain fully resolved DCS spectra, the relative tooth linewidths between both combs needs to stay below Δf_r during the entire measurement time to avoid crosstalk between adjacent pairs of rf comb teeth in the DCS downmixing process. One way to achieve this is tight phaselocking of both combs with a comb tooth integrated phase noise well below 1 radian and most of the optical power confined to the carrier [144].

While an individual IGM acquired over $1/\Delta f_r$ thus results in a fully resolved spectrum with point spacing of f_r, its SNR is often insufficient for many applications. It is thus standard practice in DCS to measure multiple consecutive interferograms [56, 145, 146], which ideally leads to an improvement of the SNR proportional to the square root of the measurement time as shown in Equation 5. Note that this only holds true if the relative tooth linewidth stays below Δf_r during the measurement time. For second-scale measurement times, this can be achieved through tight phase-locking of both combs [56]. While the measurement time of such tightly locked systems is often limited by slow phase drifts, it can easily be extended. The phase drift between consecutive saved interferograms can be extracted by either subtracting their phase in the spectral domain or calculating the cross-correlation between the initial IGM and each subsequent IGM. The calculated phase drift ϕ_{noise} can then be removed from the IGM by multiplying it with $e^{-i\phi_{noise}}$. To reduce the data and processing burdens, those phase coherent interferograms are often coherently averaged before being saved to disk and transformed into a spectrum [145]. Figure 8 shows the concept of coherent averaging. Individual IGMs are coadded for a desired averaging time before being written to disk. In the spectral domain, this is equivalent to sampling the spectrum at the peak of the comb teeth as shown in Figure 8b.

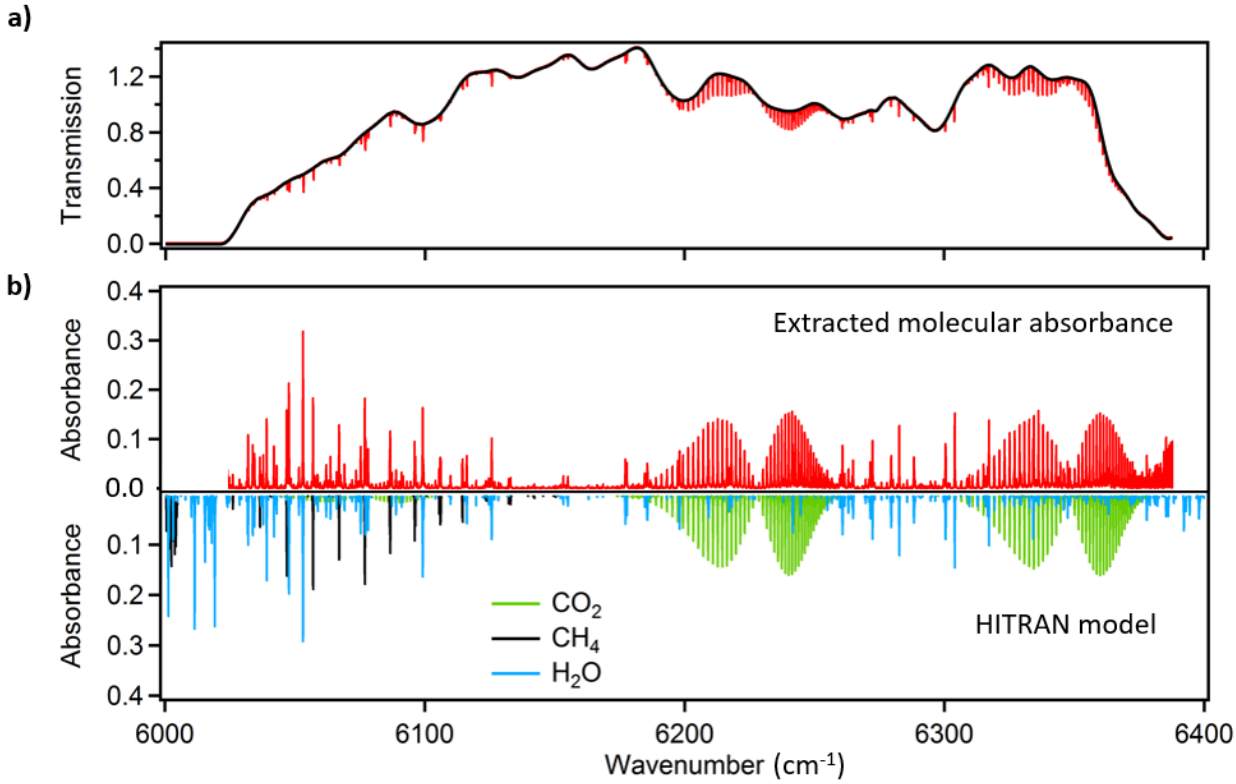

Figure 9: Example measured NIR, open-path DCS spectra for a 1-km one-way path. a) Raw transmission spectrum in red and fit baseline in black. b) Extracted absorption spectrum, $A(\nu)$, shown in red in the upper panel. The lower panel shows the model using HITRAN for each species (inverted for clarity).

DCS systems that use frequency combs with looser locks or are even completely free-running often exhibit linewidths exceeding Δf_r over the time span of a single IGM and require high-bandwidth phase drift (and also timing jitter) characterization and correction before co-adding. One approach is to measure the comb's differential phase noise (e.g. using a CEO signal and a heterodyne signal between the combs and a common cw laser) and subtract it in real-time signal processing through point-by-point rotation and resampling of the IGMs on an field-programmable gate array (FPGA) [99, 143]. Alternatively, an adaptive sampling clock can be used in an analog high-bandwidth phase correction scheme [147]. Yet another approach is to extract the phase noise from the measured interferograms using an augmented Kalman filter [148].

2.7 Extraction of species concentrations

Spectroscopic trace gas analysis typically relies on the Beer-Lambert law:

$$I(\nu) = I_0(\nu)e^{-\ell \sum_i \sigma_i(\nu)c_i} \tag{7}$$

where $I(\nu)$ is the measured spectrum, $I_0(\nu)$ is the reference spectrum in the absence of any absorbers, ℓ is the measurement path length, $\sigma_i(\nu)$ is the molecular cross section for trace gas i, and c_i is the path-averaged concentration of the trace gas. Here we focus on trace gas concentration retrievals, where typically $I(\nu)$, $I_0(\nu)$, and ℓ are measured, $\sigma(\nu)$ is a property of the trace gas, and the molecular concentration c is the quantity of interest and estimated through inversion of (7)[3]. An example open-path DCS spectrum and analysis is shown in Figure 9. Note that the DCS instrument can also be used to determine $\sigma(\nu)$ and has

[3]Technically, open-path DCS measures the path-integrated column density, $c_i\ell$, often given in units of a mixing ratio as ppm-m or ppb-m. Since the path length, ℓ, is known, this can be converted to path-averaged mixing ratio in ppm or ppb. We use both notations throughout the text.

been used to supplement databases [76, 149–152]. $\sigma(\nu)$ is often obtained from databases containing either line shape parameters or cross section spectra.

For most of this work, the path length ℓ is measured using either a Mach-Zehnder interferometer which has an uncertainty of ∼30 cm, or a laser range-finder which has an uncertainty of ∼50 cm, resulting in a sub-% error contribution for typical path lengths of 100s of meters. $I(\nu)$ is measured every $1/\Delta f_r$ seconds and recorded every ∼30 seconds, and $\sigma(\nu)$ is calculated from line shape parameters obtained from HITRAN (*hi*gh resolution *tran*smission molecular absorption database) [153–155]. However, it is challenging to measure $I_0(\nu)$ with the DCS system because of rapid spectral fluctuations causing baseline drift and complex telescope optics hindering the measurement of a precise duplicate of the probing spectrum $I_0(\nu)$. For rovibrationally-resolved lines with narrow spectral features, we estimate $I_0(\nu)$ by fitting $I(\nu)$ to a combination of a polynomial baseline and molecular transmission in small spectral chunks and stitching together the polynomials across all chunks. Later in this section we will discuss approaches for fitting larger molecules whose absorption cross section is no longer rovibrationally-resolved (broad absorbers).

2.7.1 Line parameters

HITRAN provides a list of lineshape parameters for small molecules that have rovibrationally-resolved spectra rather than molecular cross section data. For small molecules, open-path spectra are typically fit using the Voigt profile, which is the most complex lineshape that can be calculated using the standard HITRAN data. As of HITRAN 2016 [155], data for more complex lineshapes are being incorporated but at the time of analysis, this data was not available for the molecules of interest. Data in this chapter was typically fitted using HITRAN 2008 [156] as it was found to produce smaller residuals for methane than HITRAN 2012 [157] and, for most work, HITRAN 2016 [155] was not available for CO_2 and CH_4 at the time of analysis.

The Voigt profile is a convolution of Gaussian and Lorentzian line profiles [158] and is given by the equation:

$$F_V(\nu) = \int_0^\infty F_G(\nu - \nu_0, \Gamma_D) F_L(\nu - \nu_0, \Gamma) d\nu \tag{8}$$

where ν_0 is the line center, F_G is the Gaussian line function, F_L is the Lorentzian line function, Γ_D is the Gaussian half-width, and Γ is the Lorentzian half-width.

The Gaussian line profile is given by the function

$$F_G(\nu - \nu_0) = \sqrt{\frac{\ln(2)}{\pi}} \frac{1}{\Gamma_D} \exp\left(-\ln(2) \left(\frac{\nu - \nu_0}{\Gamma_D} \right)^2 \right) \tag{9}$$

where Γ_D is the Doppler half-width and is given by the equation:

$$\Gamma_D = \sqrt{\frac{2\ln(2)kT}{mc^2}} \nu_0 \tag{10}$$

where k is the Boltzmann constant, T is the measurement temperature in K, m is the molecular mass in kg, and c is the speed of light.

The Lorentzian profile is given by the equation:

$$F_L(\nu - \nu_0) = \frac{1}{\pi} \frac{\Gamma}{(\nu - \nu_0 - \delta)^2 + \Gamma^2} \tag{11}$$

where δ is the pressure-induced line shift and Γ is the Lorentzian half-width and is determined experimentally and obtained from HITRAN.

HITRAN provides the Voigt profile parameters S_i (linestrength), v_0 (vacuum line center), Γ (Lorentzian half width), and δ (line center pressure shift) as well as an additional parameter n (temperature-dependent exponent for the Lorentzian half-width). The Gaussian half width for a given molecule can be calculated for a given measurement temperature. An overview of Voigt line shape parameters are given in Figure 10.

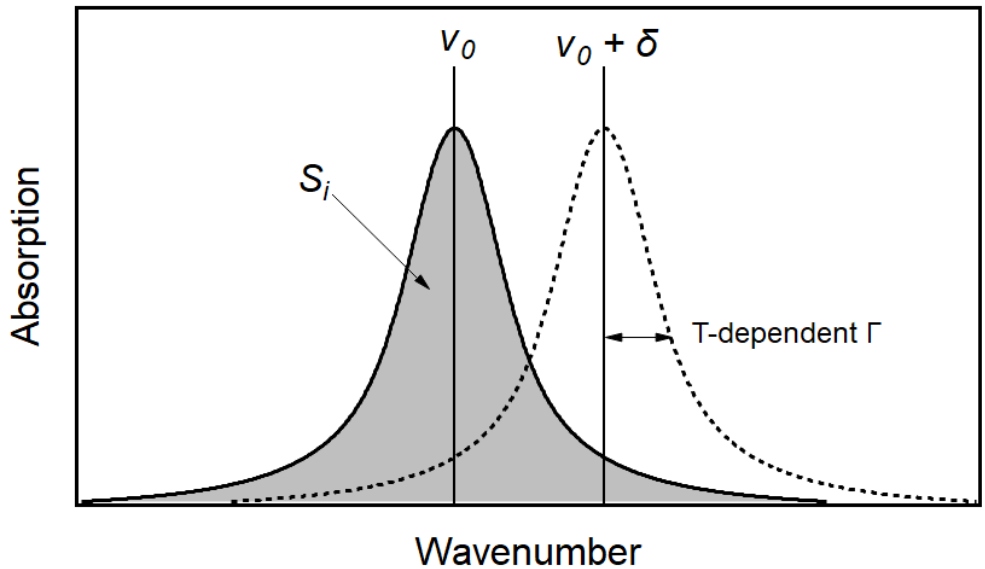

Figure 10: Voigt spectral line profile with several line shape parameters shown: S_i (linestrength), v_0 (vacuum line center), Γ (Lorentzian half width), and δ (line center pressure shift). Adapted from hitran.org.

2.7.2 Spectral fitting of ro-vibrationally resolved species

Much of the analysis discussed in the applications section (Section 3) results from fitting small molecules with isolated ro-vibrational lines such as CO_2, CH_4, and H_2O. An example open-path DCS spectrum of these species in the NIR is shown in Figure 9. As discussed above, it is difficult to measure an I_0 spectrum for DCS, so for these molecules we calculate a baseline as the I_0 spectrum. The calculation typically fits a 7th order polynomial to the spectrum in 0.3 THz (10 cm^{-1}) chunks. The baseline calculation is also informed by the line center positions and the strengths based on the estimated concentration, so the calculation is not distorted by absorption lines, even for strong absorption.

The measured $I(\nu)$ spectrum is then divided by this calculated $I_0(\nu)$ spectrum to produce an absorption spectrum $A(\nu) = -\ln(\frac{I}{I_0}) = -\ln\sum_i(\sigma_i(\nu)c_i\ell)$. Using HITRAN, $\sigma_i(\nu)$ is calculated for each species assuming Voigt line profiles as discussed above. Then, the species concentrations can be estimated from the measured absorbance spectrum through linear least-squares fitting. However, this is only an approximation as the molecular lineshapes change as a function of temperature, pressure, concentration of other gases, etc. Most of these other effects, such as self-pressure, air-pressure and water-pressure lineshape changes and linemixing, are either negligible in many cases or not sufficiently well known to include in the fit. Thus, we calculate $\sigma(\nu, T)$ for different temperatures T and, using nonlinear least-squares fitting, estimate both species concentrations c_i and measurement path-averaged temperature T from A.

This fitting uses spectral databases. This means that no calibration is necessary in the traditional sense where an instrument relies on bottles of calibrated gas standards. However, this can introduce systematic errors that are present in the database. For example, different databases can yield substantially different retrieved trace gas concentrations. The switch from HITRAN 2008 to HITRAN 2016 results in an 8% increase in retrieved CH_4 concentration at the 1.6 µm region due to changes in the linestrength values. Further, databases are sometimes lacking under certain conditions such as high pressures or very high temperatures. This makes it challenging to retrieve accurate concentrations under such conditions.

2.7.3 More complex fitting cases

As DCS moves beyond fitting small molecules with rovibrationally resolved spectra that are well-represented in HITRAN, additional fitting techniques are necessary. In particular, this is necessary in the MIR when fitting ethane, acetone, and other molecules with many C-H stretches as discussed in Section 3.6. These

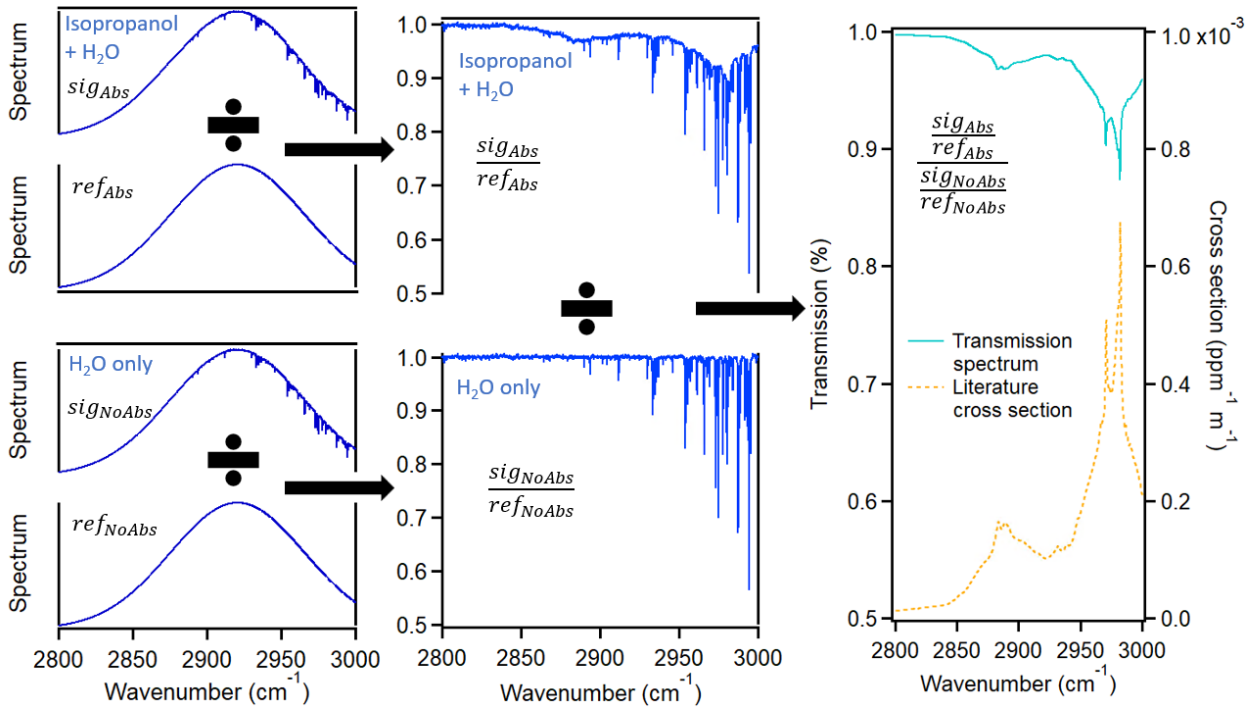

Figure 11: Schematic depicting change detection for broad absorbers. Here, water is a narrow absorber present in both sig spectra and isopropanol is a broad absorber present only in sig_{Abs}.

molecules do not have rotationally-resolved lines; rather they have broad spectra that are difficult to distinguish from the broad comb baseline structure. Therefore, it does not make sense to use lineshape profiles to model the overall absorption. Instead, these are fit using absorption cross sections from the Pacific Northwest National Laboratory (PNNL) Infrared Database [159] or with other measured cross sections. Ideally, the overall broad comb baseline structure could be removed by recording a signal and reference channel simultaneously as shown in the telescope designs in Figure 6. Here, the signal channel records the signal after passing through the analyte (for example, ambient air with acetone and isopropanol plumes), while the reference channel records the comb spectrum after passing through just centimeters of air. The transmission spectrum of the analyte can then be obtained by the simple ratio $\frac{sig}{ref}$. However, the telescope optics and retroreflector usually introduce additional broad structure in this ratio that can interfere with the fitting of broad absorption features, thus additional techniques are often required as discussed below.

One technique that can help separate the spectral baseline from the gas absorption lines is change detection. In this method, the ratio of signal to reference is further referenced to a ratio taken in the absence of any absorbers, i.e. the final data to be analyzed $= \frac{sig_{Abs}/ref_{Abs}}{sig_{NoAbs}/ref_{NoAbs}}$ where sig_{Abs} and ref_{Abs} are the signal and reference spectra in the presence of the broad absorbers and sig_{NoAbs} and ref_{NoAbs} are the signal and reference spectra in the absence of broad absorbers. This is shown schematically in Figure 11 with synthetic data. This works well for cases where a plume of a broad absorber is added artificially such as in [67] or when a time period exists where there are no broad absorbers of interest. In this case, the signal and reference measurements made during the time with no broad absorbers are the sig_{NoAbs} and ref_{NoAbs} spectra shown in Figure 11. This technique was used in [67] to retrieve acetone and isopropanol over a 162 m (one-way) path with sensitivities of 5.7 ppm-m and 2.4 ppm-m at one-minute averaging time and was limited by baseline variability not removed by the double ratio. However, this does not work for all cases for analyzing broad absorbers, for example, if there is no known period with no absorption from the species of interest.

A second technique that has been used for analysis of broad absorbers, especially for short time periods of an hour or less, is to use a "shorted path". This technique is conceptually similar to the idea of change detection above, but the spectrum in the absence of any absorbers is a very short open-air path that is

a meter or two long rather than the full-length path in the absence of the broad absorbers. Thus, the absorption on the short path is negligible. The fitted spectrum is therefore $\frac{sig_{Long}/ref_{Long}}{sig_{Short}/ref_{Short}}$ where sig_{Long} is the signal data measured over the long path and ref_{Long} is data measured at the same time but over the reference path. On the other hand, sig_{Short} is the signal data measured over the short path (e.g. few meters), and ref_{Short} is data measured at the same time, but over the reference path. The short and long path data are taken sequentially and then compared to each other. This technique allowed ethane to be detected at a concentration of 3.75 ppb with a sensitivity of 0.4 ppb at one-minute averaging times over measurement time periods of 30 minutes [67]. However, optical differences between the short and long path as well as temporal baseline variation can still result in spectral structure at the few-percent level.

A third method that has been used to fit data, especially broad absorbers, is differential fitting. This technique is borrowed from the DOAS technique [25]. The principle behind DOAS is that spectra can be decomposed into a broad polynomial component that varies slowly with wavelength and a narrow-structure component that varies rapidly with wavelength.

$$I(\lambda) = I_0 \times \exp\left[\sum_i \Big(- \sigma_i(\lambda) c_i \ell \Big) - \Big(\sigma_{Ray}(\lambda) + \sigma_{Mie}(\lambda)\Big)\ell\right] \tag{12}$$

where $\sigma_i(\lambda)$ is the wavelength-dependent cross section of molecular species i, c_i is the concentration of species i, ℓ is the path length, $\sigma_{Ray}(\lambda)$ is the wavelength-dependent Rayleigh scattering cross section, and $\sigma_{Mie}(\lambda)$ is the wavelength-dependent Mie scattering cross section. $\sigma_i(\lambda)$ is further broken up into a broadband component $\sigma_B(\lambda)$ and a narrow-band component $\sigma'(\lambda)$. The previous equation can then be expanded as:

$$I(\lambda) = I_0 \times \exp\left[\sum_i \Big(- (\sigma_{B,i}(\lambda) + \sigma'_i(\lambda)) c_i \ell \Big) - \Big(\sigma_{Ray}(\lambda) + \sigma_{Mie}(\lambda)\Big)\ell\right] \tag{13}$$

and the sum of all broadband components – $\sigma_{B,i}(\lambda)$, $\sigma_{Ray}(\lambda)$, and $\sigma_{Mie}(\lambda)$ – are fitted out as a polynomial. The resulting differential spectrum $I'_0(\lambda) = I_0 \times \exp\Big(\sum_i(-\sigma'_i(\lambda)c_i\ell)\Big)$ is fitted with the differential cross section $\sigma'_i(\lambda)$. In practice, this is done by fitting a baseline with the same parameters as the standard baseline fit to the broad absorber cross section, for example, fitting the cross section with the same baseline parameters as the baseline correction. This technique is most successful with molecules that have a significant narrow-band component. For example, this fitting technique is more successful with ethane than propane. This approach was used to fit the broadband VOCs discussed in Section 3.6.

A final technique that is used for fitting more complex data is time-domain or cepstral fitting of the molecular free induction decay [160, 161]. This technique relies on the fact that the centerburst of the IGMs produces the broad spectral structure, while the free induction decay far from the centerburst is what produces narrow absorption lines in the absorption spectra. To 'deconvolve' the spectrally broad baseline intensity from the spectrally narrow molecular response in the time domain, the fit is performed on the inverse Fourier transform of the logarithm of the measured spectrum $I(\lambda)$, also known as the cepstrum $\mathcal{F}^{-1}\{\ln(I(\lambda))\}$. The cepstrum is then masked up to a certain cut-off time that depends on overall spectral shape and absorber widths, but should roughly be shorter than the inverse absorber width. This is similar to applying a high-pass filter to the measured spectrum and suppresses the broad baseline. An advantage of this method is that it can speed up processing when compared to the computationally expensive standard piecewise polynomial baseline estimation discussed above.

2.8 Comparability

In addition to sensitivity, it is important to look at potential biases in DCS. While in principle DCS has high accuracy because of the lack of instrument lineshape, there are other potential effects that can lead to biases in the retrieved concentration. In order to look for these effects, two NIR DCS systems based on the same Er:fiber design but constructed by different groups were compared across an open path [38]. The two systems are referred to below as DCS A and DCS B. The light was launched from two neighboring telescopes (designs b and c in Figure 6) over adjacent open-air paths of approximately 2 kilometers round-trip to two retroreflectors separated by approximately 10 meters.

During initial testing, several issues were identified that can cause biases in the retrieved concentrations. In particular, differences were observed for the same signal split between different channels of the ADC and between different ADCs. This was eliminated by amplifying the signal to fill the voltage range of the ADC and by adding a low-frequency dither signal (∼1 kHz) to spread the IGM over a range of voltages. In addition, as discussed in Section 2.5, saturation can occur in any rf amplifier used after the detector. Saturation in standard low-power rf amplifiers (e.g., the Minicircuits ZFL series [162]) led to biases in the path-averaged concentration of a few ppm (∼1%) for CO_2, which were eliminated by using high-power rf amplifiers or fast voltage amplifiers (e.g. Stanford Research Systems amplifiers and Minicircuits ZHL-1-2W [162]). Smaller biases were observed due to etalons in optical components as well as light scattering from the reference path of the telescope being picked up on the signal detector (see telescope b in Figure 6), which looks like an etalon in the spectrum. In addition, optical nonlinear mixing can occur and lead to biases if the two frequency combs are combined in fiber at high optical power so care should be taken to spectrally filter the combs first before combining to reduce the total power. Finally, biases were observed for signals that were mapped to higher radio frequencies. This is believed to arise from the frequency response of the ADC. To remove this bias, the comb locks were adjusted to fit the entire spectrum in lower radio frequencies.

The instruments were compared over a two-week time period after removing the sources of bias discussed above. Three-hour-averaged spectra were compared between the two DCS instruments, as well as retrieved CO_2, CH_4, and H_2O concentrations over the full two weeks [38]. The two averaged spectra agreed to better than 10^{-3} and showed no residuals at any lines, indicating that the DCS instruments do have identical delta function lineshapes and that instrument lineshape does not contribute to biases. The magnitude of the difference between the two spectra was driven by an etalon on one of the telescopes. Without this etalon, the actual agreement was more than a factor of four better and dominated by white noise. Over the two week intercomparison period, the retrieved concentrations between the two DCS instruments agreed to better than 0.6 ppm of CO_2, 7 ppb CH_4, and 40 ppm H_2O over a temperature variation of 4.6 to 28.9 °C, 10 to 90 % relative humidity variations, and large return power fluctuations (retrieved data shown in Figure 12). All three differences show an approximately Gaussian distribution indicating that the differences are likely driven by white noise. This agreement is a factor of 10-100 better than other published open-path intercomparisons and is close to the World Meteorological Organization intercomparability goals for greenhouse gas instruments [163].

2.9 Long term operation and field deployment challenges

As mentioned in Section 1.1, one advantage of open-path measurements is that they can provide continuous monitoring of numerous area or point sources. However, in order to realize this advantage, the system must be able to run continuously with high SNR over the full time frame of the deployment. This in turn places stringent requirements on the stability and robustness of the DCS system. For long-term operation, any system ideally should be housed in a moderately temperature-controlled environment (e.g. small trailer with heating and air conditioning) and have access to a cellular network or internet connection for remote uploading of measurement data as well as for occasional troubleshooting and maintenance. Furthermore, the combs need to remain locked for long periods of time – preferably weeks to months – with minimal to no intervention and need to be relatively insensitive to temperature fluctuations since field sites have substantially worse temperature control than most metrology laboratories. All-fiber frequency comb designs such as the Er:fiber ones used in Section 3 are the most developed solution to this problem so far. These lasers are compact and are able to withstand significant vibrations without loss of locks [36, 37, 78]. Further, the all-fiber nature means that the alignment of the system will not drift with temperature changes. We have found that the addition of any free-space components (such as the optics used for the DFG systems discussed in Section 3.6) greatly increases the system sensitivity to environmental parameters and requires substantial effort to either temperature control the entire system or the entire field environment.

In addition to remaining locked for weeks to months at a time, the system must also be able to collect data over this time period. This essentially makes the coherent averaging described in Section 2.6 a necessary component of fieldable DCS systems for data reduction. For a system such as ours that collects an interferogram every 1.6 ms, 24 hours of data collection will produce 54 million interferograms without coherent averaging. Storing, transferring, and processing that much data is a substantial challenge, and one that cannot be met by streaming data on an oscilloscope as is done for a number of laboratory demonstrations of

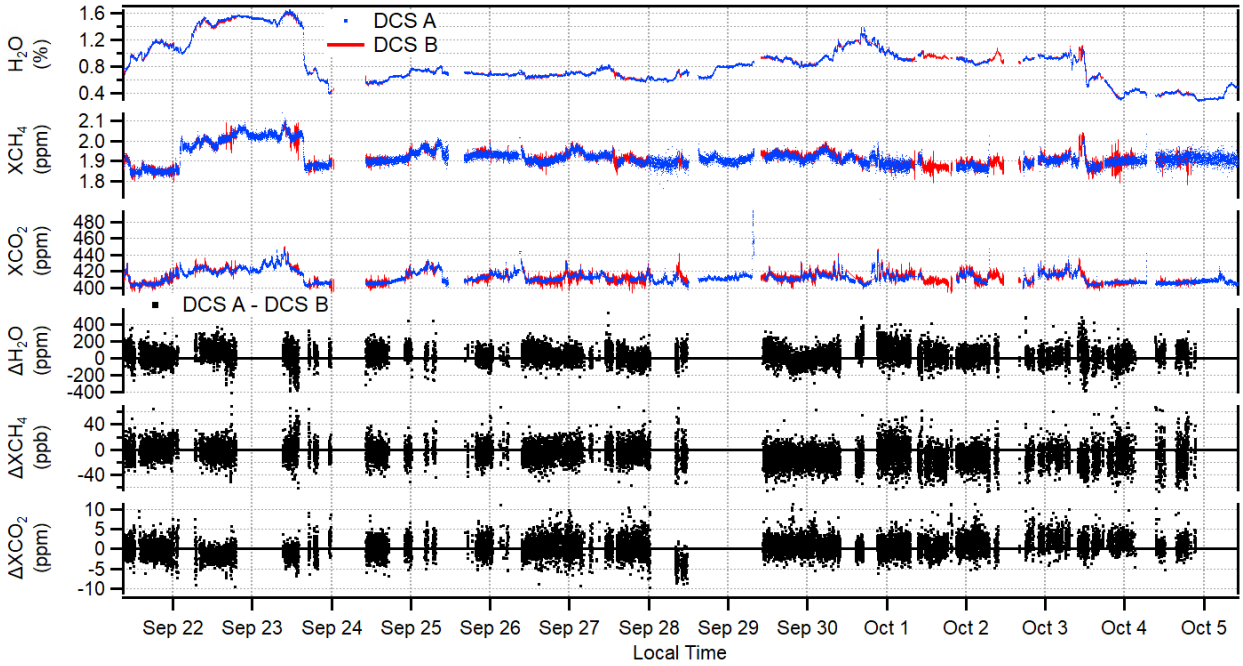

Figure 12: Comparison of data retrieved from two DCS systems (A and B) over approximately two weeks. The upper three time series show the retrieved concentrations overlaid; the lower three time series show the difference in retrieved concentrations. Adapted from [38].

DCS. However, with coherent averaging to 30 second time resolution, that same system will produce 2880 interferograms which requires much less disk space and much less time to process. Further, the coherent averaging enables increased SNR, which reduces the requirement for data averaging in the post-processing steps [145] and reduces bias that arises from processing low-SNR spectra [141].

Further important considerations for the field deployment of a DCS system include the space, power draw and equipment needed for a successful deployment in rugged conditions. A full fiber-laser-based, NIR DCS system will draw about 800 W of power and occupies approximately one 18U 19-inch rack mount (not including the telescope system). This power draw includes all lasers and pump diodes, temperature controllers, power supplies, control electronics, computers, data acquisition, and gimbal control; however, it does not include external temperature control of the environment. The MIR system used in Section 3.6 currently requires more space and power. In addition, the telescope and pointing stage need to be mounted outside with connections to the electronics inside (typically an optical fiber, power, and USB or ethernet for the camera). The telescope/stage can be placed on a tripod, mounted to the roof of a building or trailer (note that mounting to the roof of a trailer will require a faster pointing servo to account for movement of the trailer due to wind, etc.), or mounted on a tower (which will require ∼10-20 m^2 of ground space for securing the tower).

Another challenge of long-term operation is maintaining the telescope/reflector alignment even in possibly adverse outdoor conditions. While the use of a corner-cube retroreflector eliminates issues with pointing drift of the reflector, the telescope pointing can still drift. Because the divergence angle of the launched beam is typically small in order to reduce the required launch power, the tolerance for pointing errors is also small. Thus, in order to enable long-term operation, an active pointing servo is typically required. This is accomplished by mounting the telescope on a motorized stage or gimbal. For kilometer-scale path lengths, this stage usually needs $0.01 - 1$ mrad pointing precision and needs to be able to support the weight of the telescope systems, which can be > 20 kg for large-aperture systems like that shown in Figure 6c. In addition, for active control it is desirable to have as low of hysteresis and backlash as possible and is important that these effects are repeatable across a range of environmental parameters.

Several options exist for obtaining the error signal to use to feedback to the telescope pointing. The

simplest option is to maximize the collected power; however, there are difficulties with this approach. First, the collected power can vary significantly over short timescales due to atmospheric turbulence [61, 62, 164, 165]. This can lead to confusion in the optimization routine unless care is taken to average the returned power values for long enough to smooth out these variations. Second, a simple measurement of the collected power does not provide directional information, i.e., low power does not tell you if the pointing is off left, right, up, or down. This can be addressed in principle by slightly dithering the pointing of the telescope or launched beam at two frequencies (one for horizontal and one for vertical) and then using lock-in detection to obtain an error signal. However, this adds significant complexity both in applying a modulation at a good frequency and in demodulating the return power. It also modulates the data, which can cause issues in DCS if the modulation frequency is too close to δf_r. Alternatively, one can perform a search routine to optimize the power. A drawback to this is that some data interruption occurs during the search routine, so care must be taken to develop an efficient routine that is not applied too frequently. Finally, if the signal is completely lost, it can be very difficult to regain alignment by just using the received power.

An alternative method is to use a camera co-aligned with the telescope to provide two-dimensional alignment feedback [65]. While it is in principle possible to just use the camera image to identify the location of the reflector, this process can be simplified by including a light source that is detectable by the camera. Then the location of the reflector in the camera image can be readily identified by selecting the bright spot arising from the reflected light. High-brightness, NIR LED flashlights (emitting light at ∼850 nm with ∼ 1 W of power) are readily available and work well for this. These light sources have significantly higher divergence angles (∼10 degrees), thus the pointing feedback has a wide capture range. One challenge with this method is that stray reflections or bright spots on the camera can lead to errors in the spot detection routine. Adding a bandpass filter in front of the camera helps significantly but occasional problems still arise. In addition, for path lengths beyond a few kilometers especially with high turbulence, the amount of light collected is low and fluctuates significantly, which can result in problems with this simple scheme. With a bit of added complexity, it is possible to do a simple lock-in detection by turning the LED on and off and looking at the difference between successive camera images. Perhaps the biggest challenge with the camera-based method is that the alignment of the camera relative to the telescope can drift, resulting in a drop in the received spectroscopy light power. To compensate for this, it is often useful to add a slower feedback using the collected power.

3 Applications

In this section, we discuss recent applications of open-path DCS to measurements of urban greenhouse gases (Section 3.2), measurements of emissions of methane from oil and gas (Section 3.3), measurements using a mobile retroreflector on a UAV (Section 3.4), measurement of emissions from agriculture (Section 3.5), and measurement of VOCs (Section 3.6). For many of these applications, the goal is to determine emission rates of gases from sources, which requires meteorological measurements as well as an atmospheric model in many cases. This is discussed in Section 3.1.

3.1 Emission rate determination

Traditionally, emission rates have been determined using point-sensor-based concentration measurements [166, 167]. There exist several methods to accomplish this including eddy covariance e.g. [168–171] and flux gradient for area sources [172, 173]; tracer release e.g. [174–179] and EPA Other Test Method (OTM) 33a e.g. [180–183] for point sources; and numerical inversion techniques for point and area sources (see references below). Numerical inversions can also be used with path-integrated measurements. This method relates concentration measurements (at m locations) to the source strength (from n sources) with a matrix equation [184]

$$\boldsymbol{C} = \boldsymbol{C_{bg}} + \boldsymbol{G}\boldsymbol{Q}. \tag{14}$$

Here, $\boldsymbol{C}$ is a matrix of concentrations with dimensions of $m \times 1$, $\boldsymbol{C_{bg}}$ is a matrix of background concentrations with dimensions of $m \times 1$, $\boldsymbol{Q}$ is a length-n vector of source strengths, and $\boldsymbol{G}$ is an $m \times n$ matrix that relates the source strength at one point to a concentration at a sensor. $\boldsymbol{Q}$ is often called the influence function and is typically determined with an atmospheric dispersion model which is represented by $\boldsymbol{G}$. Alternatively,

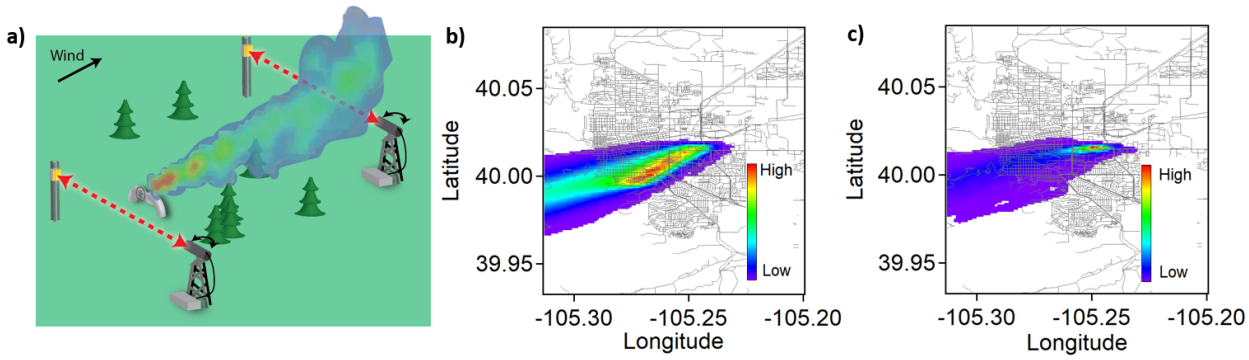

Figure 13: Emission rate measurements using long path. a) Configuration using two measurement paths, one upwind and one downwind of a source. b) Example footprint for a single hour measurement. c) Same but for a point sensor. The color scale in b and c is the contribution to the footprint and is linear and spans two orders of magnitude.

the influence function can be expressed as a sensor footprint, which gives the influence of a source at each grid point in the measurement domain on the sensor measurement. Finally, various methods can be used to invert Equation 14 and determine an estimate of $\boldsymbol{Q}$, see, e.g., [184–190]. Note that this equation can also be run "forwards" to calculate $\boldsymbol{C}$ if $\boldsymbol{Q}$ is prescribed.

However, these point-sensor-based methods all have limitations. For example, eddy covariance and flux gradient techniques are challenging to apply in complex terrain and have limited spatial footprints [167, 191, 192]. Tracer release measurements and OTM 33a require site access and knowledge of the location of the emission and cannot be used for continuous measurements. In addition, the accuracy of OTM 33 depends substantially on the layout of the site [193]. Finally, numerical inversions rely heavily on a dispersion model to determine an emission rate and when using data from point sensors are sensitive to wind variations, which can lead to high errors [167]. Determining fluxes not from point sensors but from an integrated line sensor like open-path DCS can overcome many of these challenges.

A simple, idealized example of emissions quantification using open-path measurements is shown in Figure 13a. Here, two measurement paths are used, with one located upwind of the source to be characterized and one located downwind. Enhancements on the downwind path relative to the upwind path can be directly related to sources and sinks within the contained area. Note that these paths can be upwind and downwind of an entire well pad or landfill, and thus do not necessarily require site access. Trace gas enhancements are then combined with simple models or atmospheric inversions to determine source or sink characteristics, e.g., [17, 66, 134, 166, 194–198]. Compared to similar techniques using a point sensor, open-path measurements have several potential advantages. First, open-path measurements can be applied for both point and area sources and also have wide flexibility in coverage by changing the path length. Second, because of the distributed measurement path, they are less sensitive to loss of data due to wind direction shifts and to measurement biases due to errors in the wind direction measurement. Third, the distributed measurement path increases the measurement footprint (the upwind fetch or source area the measurement is sensitive to), which allows for measurement sensitivity to a larger upwind area. This is illustrated in Figure 13 where the footprint of an open path measurement is shown in b compared to that of a point measurement in c. Warmer colors represent a greater contribution to the footprint and cooler colors represent a smaller contribution to the footprint. These images show that the footprint from the open-path measurement is broader and more uniform than that from a point sensor. Open-path measurements can also be used in other configurations beyond this simple, idealized configuration. One configuration utilized in several applications discussed below is to use radial beam paths that originate from a central location, see e.g. [17, 18, 66, 134, 199]. The beam paths can originate from multiple co-located transmitters or from a single transmitter that is scanned between reflectors. Depending on the wind direction, different beam paths can then be used to represent the upwind and downwind measurements from a source. This configuration has the advantage that the the transmitter or transmitters and spectrometer are all co-located, which reduces setup and operational complexity. Other configurations for open-path measurements include flux gradient, which use two vertically

separated beam paths [172, 200], vertical radial plume mapping using five beam paths [31, 201] as well as tomographic reconstructions using many beam paths [202–205].

Several challenges can arise from the use of open-path measurements to characterize trace gas sources and sinks. For example, locations of measurement paths can be limited by terrain features, given that line-of-sight is necessary between the telescope and the retroreflector. Second, as with the point-sensor techniques listed above, the choice of model used for determination of emission rate can be a challenge. One possibility is to use a basic box model where the source is considered to be inside a box with background air entering on the upwind side and background plus emissions exiting on the downwind side [206]. This can work well if the downwind measurement path is far enough downwind from sources to consider the emissions fully mixed up to the height of the box (typically assumed to be the height of the atmospheric boundary layer). Otherwise, many dispersion models exist [207–210], including Gaussian plume and puff models [206, 211], forward and backward Lagrangian models such WindTrax [194] and STILT [212, 213], as well as more advanced computational fluid dynamics models. The choice of model depends on many factors, including the size of area to be modeled, complexity of terrain (including buildings or other obstructions), as well as computational resources available. A full treatment of available dispersion models is beyond the scope of this review. Recently, a technique for flux quantification without the use of a dispersion model was developed - that method is described in Section 3.4.

3.2 Urban greenhouse gas emissions

One example use case for frequency comb-based emissions estimation is a recent demonstration of vehicle CO_2 quantification in Boulder, Colorado, USA [68]. Urban areas contribute significantly to total anthropogenic GHG emissions [214, 215], with a large fraction of urban emission coming from the transportation sector. Because many cities have aggressive GHG emissions reduction targets, it is important to develop tools for monitoring, reporting, and verification of GHG emissions in order to track progress towards the reduction targets. While a number of different techniques are being developed using networks of sensors, e.g., [216–219], many of these methods rely on an inversion model with well-known priors and high-resolution atmospheric models. Long-horizontal-path measurements could help by increasing the measurement footprint of a single sensor (see Figure 13), and by reducing representation error by spatial averaging [20] which enables emissions measurements with reduced requirements on priors and atmospheric models. A similar long-path LIDAR technique has also recently been tested in downtown Paris [204, 205]; however, this technique uses cw lasers and is thus limited to measuring one species. Here, we used DCS to measure multiple species simultaneously with high time resolution.

The city of Boulder is contained in a relatively small area: approximately 8 km east-to-west by 12 km north-to-south. This area is a good fit for the current range of frequency comb path lengths. Boulder is bordered by mountains to the west and plains to the north, east, and south. A DCS system was installed in a laboratory at the western edge of the city (Figure 14). One beam path extended to the west to sample air entering the city from the mountains over a 1-km one-way path, and a second beam extended to the north-east to measure air containing emissions from the city over a 3.35 km one-way path.

In this work, we use the Er:fiber laser system described previously. It measured between 6023 and 6376 cm^{-1} (1.57 and 1.66 μm) to capture CO_2 and CH_4 as well as H_2O lines as can be seen in Figure 9. Measurements were performed in a monostatic configuration (configuration a in Figure 5). The reference path used a 5 cm home-built OAP telescope (telescope b in Figure 6 but without a reference channel) while the over-city path used a modified 25.4 cm diameter Ritchey-Chrétien telescope (telescope c in Figure 6 but without the reference channel). The choice of telescope was dictated primarily by the measurement path length – the ∼2 km reference path allowed for a smaller telescope than the 6.7 km over-city path due to much higher return power. Spectra were coherently averaged for 32 seconds per data point. This spectral region contains only narrow absorbers at concentrations detectable by the DCS, so data was fitted using the procedure described in Section 2.7.2 using data from HITRAN 2008.

The system measured near-continuously for seven and a half weeks. CO_2, CH_4, and H_2O concentration measurements were collected over both paths simultaneously. This data is shown in Figure 14 and shows that the system measured nearly continuously for the 7.5 weeks except for a several-day gap due to bad weather. The reference path data is shown in red and the over-city path is shown in black, corresponding to the path colors in Figure 14. The water data over the two paths agrees well, but clear and consistent enhancements

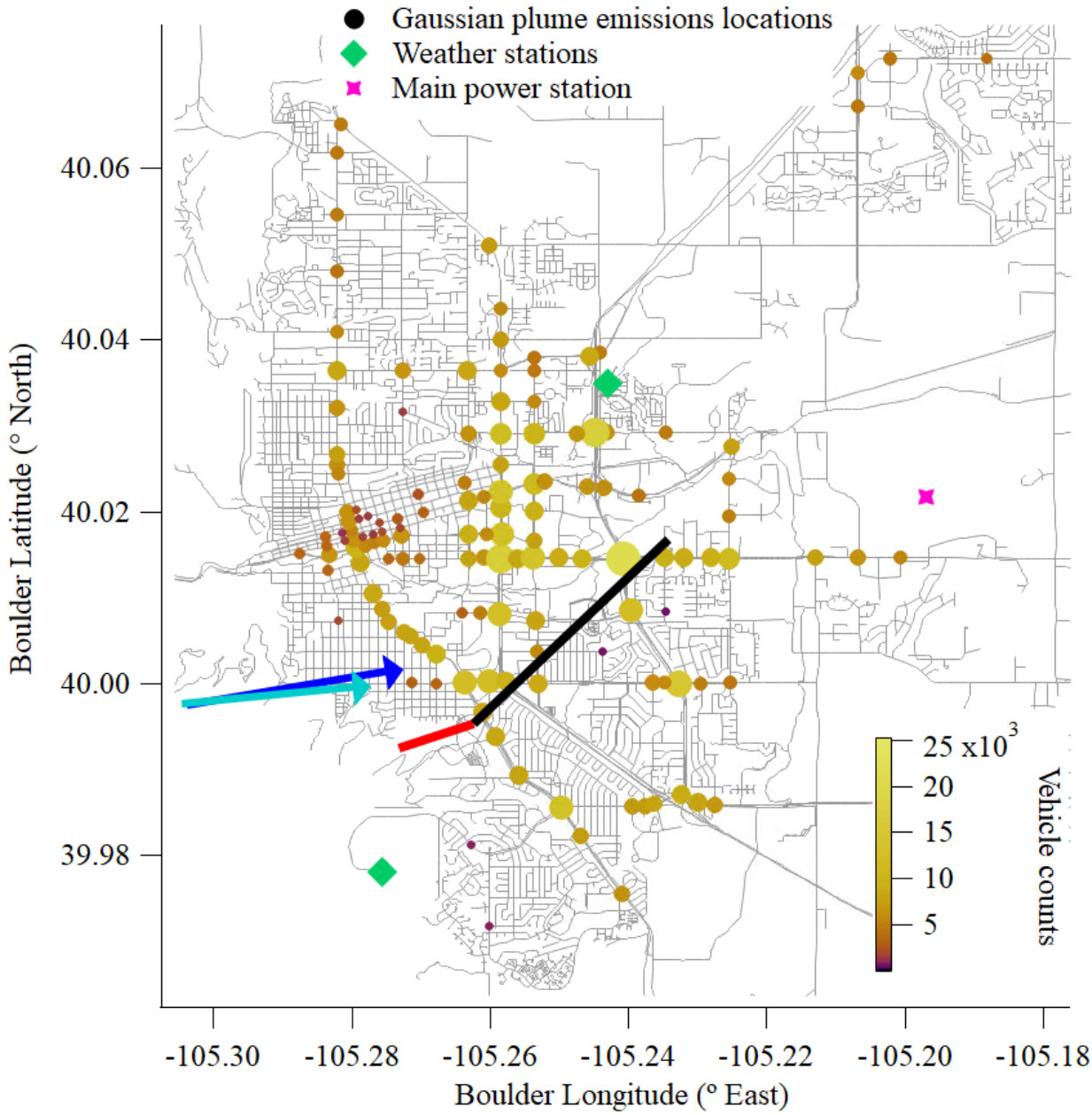

Figure 14: Diagram of measurements over the city of Boulder, Colorado for CO_2 emissions quantification. The DCS was located at the intersection of west-looking red beam path and the northeast-looking black beam path. Meteorological measurements were made at the DCS location as well as the two green diamonds. Mean wind during two case study days are given by the blue and aqua arrows. Gaussian plume emissions locations are given by the circles, colored and sized by the emissions strength as determined from vehicle traffic counts. Adapted from Figure 1 in [68].

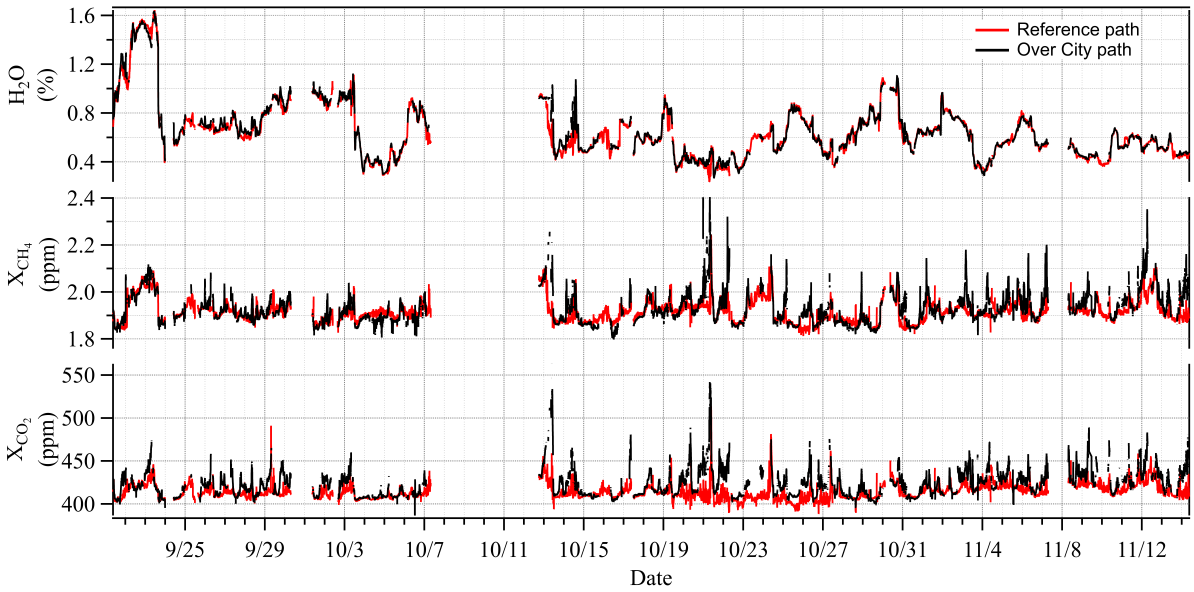

Figure 15: Time series of Boulder data over nearly eight weeks. Red: data from reference path in Figure 14. Black: data from over-city path in Figure 14. Substantial CO_2 and CH_4 enhancement is visible in the over-city data relative to the reference data.

in CO_2 and CH_4 are observed on the over-city path relative to the reference path with maxima of almost 550 ppm CO_2 and 2.4 ppm CH_4. This indicates that the city of Boulder is emitting both of these gases. Much of the enhancement occurs at night when gases are trapped in the descending boundary layer.

The 7.5-week dataset was filtered for west winds (ensuring that the west-looking path could be used as a clean air reference), and daytime enhancements in over-city CO_2. This choice was made to simplify modeling requirements, as simulation of nighttime boundary layer dynamics is more uncertain than for the daytime boundary layer. Data filtering for these criteria yielded two full days of measurements - one weekday, and one weekend day. This filtering ensured that the enhancement in the over-city path was due primarily to vehicle emissions, with minor contributions from heating/cooling and small nearby power plants with minimal impacts due to meteorology. Biological CO_2 was deemed an unlikely source of the observed enhancement, given the time of day and season, location, and wind direction. Further, power plant contributions were deemed unlikely under west wind conditions because the over-city beam path excluded emissions from the main power plant east of Boulder under these wind conditions.

To calculate emissions from the observed CO_2 enhancement, a Gaussian plume model was used. The STILT-R [213] dispersion model was also tested, but found to be highly sensitive to parameterizations of vertical dispersion. Traffic measurement locations logged by the city of Boulder were used as point source locations for the Gaussian plumes, shown as colored circles in Figure 14. More plumes were emitted in areas with high traffic and fewer in parts of the city with less traffic. Each emissions location was further scaled by the fraction of traffic counts at that location to provide a more accurate source strength (circle size and color in Figure 14). When the calculated emissions were scaled up to a year to compare with the city traffic emissions inventory, they agreed within a factor of 1.6. This is within the error bars calculated for the dual-comb-based emissions (the city inventory does not include error bars). This example shows the potential to use open-path DCS to quantify emissions in support of or potential replacement of bottom-up estimates with top-down measurements.

3.3 Industrial oil & gas methane emissions

Another practical field application of open-path DCS is the detection, attribution and quantification of methane emissions from oil and gas production and storage. Several aspects of upstream natural gas and

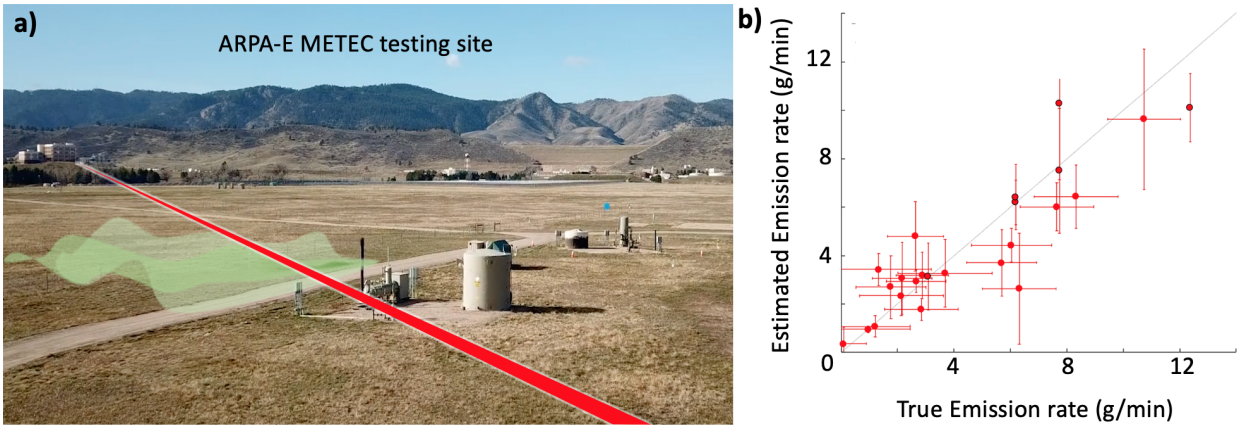

Figure 16: Using DCS to detect methane leaks from oil and gas infrastructure. a) image showing Colorado State University's METEC test facility and DCS system, located 1.1 km away at the far left, at initiation point of red beam in schematic. During single-blind METEC testing (only test administrators knew emission locations and rates), retroreflectors were stationed on the METEC test site and interrogated with DCS laser beams. Toggling between multiple beam paths yields background and enhancement information necessary to quantify the leak. b) The CU/NIST DCS sensor detected 100% of leaks and quantified emission rates to within 27% of the true rate, on average. The smallest quantified leak was 3 standard cubic feet per hour (approximately 0.02 g/s).

underground natural gas storage make these sectors of the supply chain amenable to emissions quantification with frequency comb technology. First, emissions are typically from a large number of point sources [181, 220], from which discrete plumes are readily detectable with path-integrated measurements. Second, emissions can be episodic and/or intermittent in time [221–225], so that the ability to perform continuous measurements with high stability through time is critically important. Third, potential emission sources can be widely distributed across large areas (tens to hundreds of km^2), making long (km-scale), open-path measurements an ideal sensing modality. For example, in the Denver-Julesburg Basin, one of the major natural gas production regions in the US, a relatively high-density region might only contain 1-2 wells per km^2. To reliably provide efficient, continuous monitoring of intermittent events with high sensitivity, it would be necessary to station multiple point sensors at or near each pad [226, 227]. Depending on the desired sensitivity, this rapidly becomes cost prohibitive. When appropriately configured, the dual-comb spectrometer can circumvent this problem by using a single instrument to monitor all facilities within a certain radius. For example, field experiments have demonstrated measurements along 2 km beams, which offers a radius capable of covering roughly 20 well pads with a single instrument. Here, we describe several recent examples of a fielded open-path DCS system deployed for the observation of emissions from the oil and natural gas sector.

First, a series of single-blind validation tests were performed at the Methane Emissions Technology Evaluation Center (METEC, see [228]) in Fort Collins, Colorado [134]. This site was established for the evaluation of technologies and monitoring methodologies designed to detect and quantify emissions from upstream natural gas production. Multiple natural gas "pads", or gravel staging areas for the above-ground elements involved in production (e.g., tanks, well heads and separators), are arrayed across a 0.03 km^2 area, each with a set of equipment such as could be found on a real production pad. During tests that last from one to several hours in duration, controlled releases can be performed, using carefully placed hidden flow lines to simulate emissions from realistic points on each piece of equipment. Test difficulty at the site can range from a single steady emission to multiple episodic or intermittent emissions occurring in different locations.

To simulate a realistic upstream oil and gas observation setting, the dual-comb spectrometer, housed in a mobile laboratory trailer, was situated >1 km away from the METEC facility, as shown in Figure 16a. This spectrometer again uses Er:fiber frequency combs to measure the CH_4 band around 6050 cm^{-1}. Retroreflectors were placed in the field on the METEC site. A gimbal was used to control the telescope (Figure 6a) and scanned through each retroreflector in a fixed, sequential sampling pattern with about 2 min spent per beam path. Throughout the course of a given test, DCS was used to sample open paths through

the atmosphere near the equipment being observed. The tests were single-blind, meaning that the METEC site managers were aware of the emission locations and rates but the engineers taking and analyzing the DCS measurements did not know either the emission locations or rates. Micrometeorological measurements of atmospheric properties, such as wind speed and direction were used with concentration measurements in an inversion model to estimate emission locations and rates (Figure 16b). Overall, in the first round of testing, 18 leaks were detected correctly over leak rates ranging from 0 to 10.7 g/min. All leaks were localized to the correct well pad and two-thirds of the leaks were localized to the correct piece of equipment. All leaks were quantified to within 3.7 g/min, and 94% were quantified to within 2.8 g/min [134]. The results of the METEC tests provided the validation necessary to demonstrate dual frequency comb spectroscopy as an effective means for detecting, attributing and quantifying emissions of methane from typical natural gas production site layouts.

Other field testing of Er:fiber-based DCS measurements for identifying and estimating emissions have taken place in both controlled field settings (Boulder Atmospheric Observatory, former NOAA site in North Central Colorado; and the Table Mountain Test Facility outside of Boulder, Colorado) and in active oil and gas producing and storage areas (two sites in the Denver-Julesburg Basin; one site in the Pacific region of the US; and one site in Alberta, Canada) [225]. The DCS systems used have been deployed in a van, where measurements were conducted within an hour of driving the van to a site, and in a small trailer for months unattended. These sites have confirmed the technical feasibility of making remote (no operator or control personnel on site) and temporally continuous observations in rugged field sites and through a wide variety of weather conditions [66, 197, 225].

3.4 DCS with an airborne retroreflector

In the previous applications, the measurement paths have all been static in time. Recently, the ability to scan the measurement path using a retroreflector on a quadcopter UAV has been demonstrated [65]. Figure 17a shows the basic setup. In order to track the UAV during flight, the telescope system was designed to be reasonably lightweight so that it could be used with a fast azimuth-elevation stage. The image-processing-based pointing servo described earlier was used to feed back to the stage at a rate of ∼20 Hz [65]. Figure 17b shows the UAV used to carry the retroreflector. In addition to the retroreflector, the UAV also carried several sondes (self-contained instruments) to measure temperature, pressure, humidity, and GPS location, as well as real-time kinematic (RTK) GPS for high-precision relative GPS location of the UAV.

The ability to scan the measurement path enables new measurement possibilities. One exciting possibility is to perform vertical profile measurements, which could aid in understanding the mixing of trace gases in the PBL. However, standard flight restrictions limit the altitude to 120 m, which is well below the PBL height in daytime conditions. Spatial scanning in the horizontal instead of vertical direction can provide a rapid method to look for point sources, such as CH_4 leaks from oil and gas as discussed in Section 3.3. Figure 17c shows an example measurement of a controlled CH_4 leak at the location indicated with a blue 'X'. Each measurement path from the static DCS system to the moving UAV is shown as a line and is color coded by the path-averaged CH_4 concentration (black is background and yellow is 4 ppm). The wind direction is indicated by the blue arrow and is coming from the top-right of the figure. Note that the methane enhancement is large just downwind of the source and decreases as the paths move further downwind from the source. This illustrates how the existence of a plume can be rapidly identified. Of course, due to the path-integrated nature of the measurements, a more complex flight pattern would be needed for localization in two or three dimensions.

Another possible application of DCS with a airborne retroflector is to perform rapid flux measurements of point or small-area sources. This can be accomplished by flying a vertical profile downwind of the source as shown in Figure 17d to determine the path-averaged concentration enhancement (ΔX) for species X versus height (z). The flux, F, can then be determined by integration using a micrometeorological mass balance approach [166, 229, 230]:

$$F = \frac{d}{L} \int_0^Z U_N(\Delta X) L dz, \tag{15}$$

where d is the distance from the telescope to the approximate center of the plume, L is the path length, U_N is the wind speed perpendicular to the plane of measurement, and Z is the maximum height. Note the addition of the $\frac{d}{L}$ pre-factor, which is necessary to convert the height of the UAV into height of the slant column at

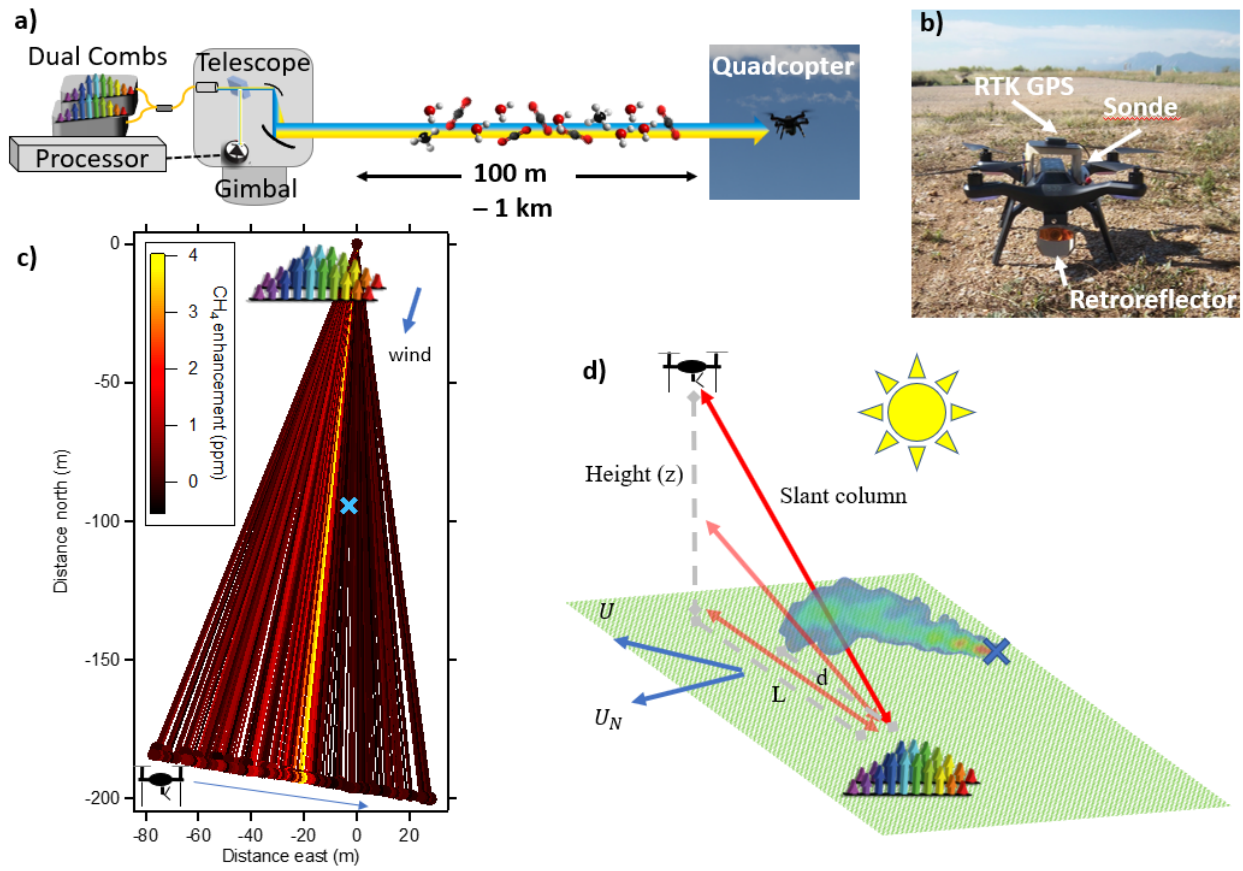

Figure 17: Spatially scanned DCS using a quadcopter UAV. a) Overview of system. b) Picture of quadcopter showing RTK GPS for accurate path length determination; sonde for temperature, pressure, and relative humidity; and retroreflector. c) Example of localization of a test CH_4 leak (leak location denoted by blue 'X') by sweeping the measurement path horizontally. Each measurement path is colored by the path-averaged concentration with black being low (background) and yellow being high (4 ppm). d) Flux determination method by flying a vertical profile downwind of a source.

the plume intersection. d can be determined from the location of plume source (which can in turn come from a horizontal scan as discussed above) and wind direction. One advantage of this technique is that it does not require any plume model. In addition, it can be accomplished rapidly. We have tested this method in the field using controlled releases of methane and acetylene. These preliminary tests suggest that the flux can be determined to ± 30 % in a single flight of $\sim$10-minute duration. For comparison, standard techniques can reach $\pm 5 - 10$ % [167]; however, these techniques require extensive setup and long measurement times. The ability to rapidly quantify emission rates will enable new applications such as rapid surveys of many sources or quantification of emissions from short temporal duration events. Furthermore, this technique is easily expandable to other wavelength regions such as the MIR, which would allow for rapid quantification of species such as VOCs (see Section 3.6).

3.5 Agricultural emissions

Open-path DCS can be used to understand agricultural emissions which are a significant contributor to global GHG emissions [231, 232]. However, the GHG sources and sinks associated with agriculture are not fully understood and there are some interesting questions that frequency combs might be well suited to address. For instance, enteric fermentation in livestock is considered the largest contributor to U.S. CH_4 emissions [233], however this estimate is based primarily on measurements taken in feed lots or barns and extrapolated

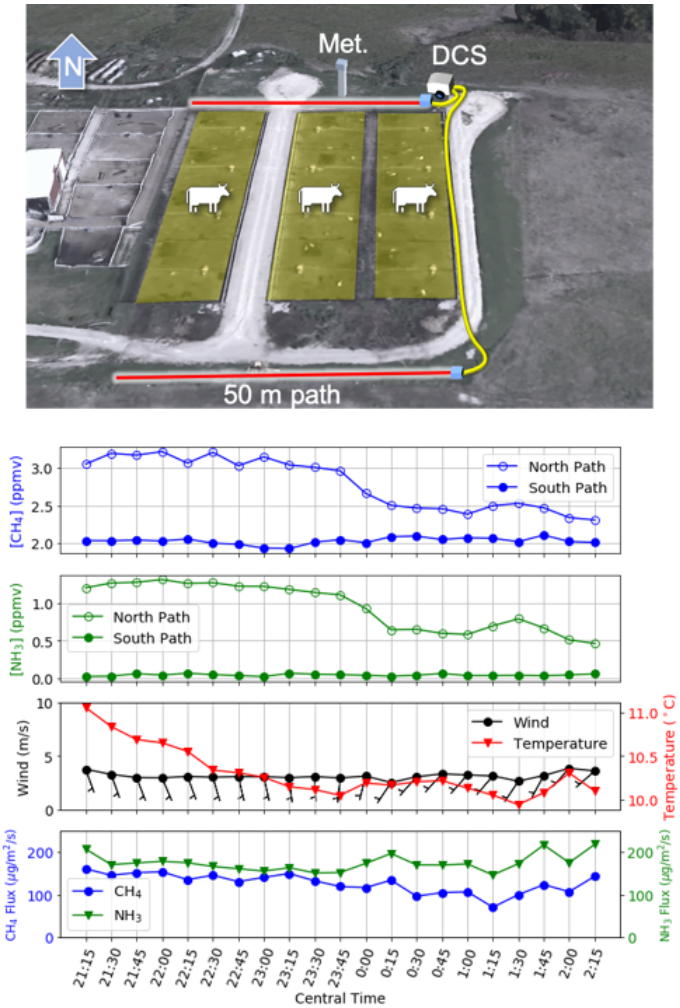

Figure 18: Setup for DCS measurements of methane and ammonia emissions at a beef stocker site at Kansas State University. North and south paths provide measurements of predominately downwind and upwind concentrations, respectively. Incorporating these measurements and wind information into an inversion model (WindTrax in this case) allows estimation of emission rates for both gases.

to pasture environments. This extrapolation to pasture environments misses both variation in feed and the potentially significant carbon uptake from the pasture itself (page 22 of [234]). Since the fact that U.S. cattle spend part of their life in pastures and only part in feed lots, this could lead to an overestimate of methane emissions [235]. Unfortunately, direct measurement of emissions from pasture cattle is challenging since the flux density is much lower than in feedlots, and for point sensors there is an additional sampling problem associated with the fact that the cattle are unevenly distributed and move often. DCS, with its ability to measure small fluxes of methane over long integrated paths that are well matched to pasture length scales, might be an ideal source to address some of these questions.

Nitrous oxide (N_2O) also presents an interesting measurement opportunity for open-path DCS. The third most problematic GHG, anthropogenic N_2O is largely generated in crop fertilization and land management practices [231, 233, 236]. A sensor that could sensitively measure N_2O at reasonable cost could provide real-time feedback in fertilization practices, minimizing over fertilization and N_2O emission while increasing farm efficiency. While DCS might not be the ideal solution, currently N_2O sensor technology is not as developed as CO_2 and CH_4 sensors, so DCS may be able to make an impact.

Another significant nitrogen source from agriculture is ammonia (NH_3). While it not a GHG, NH_3 can negatively impact air quality and lead to the production of N_2O. While understanding emission of NH_3 is important to help minimize its production, the situation is complicated somewhat by the large potential matrix of drivers including feed type, temperature, and precipitation [237]. This is further complicated by the fact that NH_3 is a reactive, sticky gas that can be hard to measure in sampling systems. DCS can be sensitive to ammonia both in the technologically convenient 1.5 μm region as well as the 2-2.5 μm region making it a potentially useful tool for understanding these emissions as well.

Figure 18 shows a preliminary effort to apply frequency combs to measure the emissions of cattle in the Kansas State University stocker facility. The DCS system here used Er:fiber combs to detect CH_4, NH_3, CO_2, and H_2O in the NIR between 6000-7000 cm^{-1} across two beam paths. Because of the relatively small size of the site, it was possible to employ the two-path configuration illustrated in Figure 13a. Optical fiber was used to connect the DCS system, housed in a trailer, to the telescopes, which allowed the beam paths to be located on the north and south sides of the site. The telescopes were simplified versions of the design in Figure 6a without the 50:50 beam splitter and detector. Instead, a fiber-based beam splitter was placed before the telescope that allowed for the detectors to be located in the trailer instead of being on the telescope. The system could simultaneously measure 5 minute averaged, ppm-level concentrations of both ammonia and methane over hours. When coupled with a backward Lagrangian stochastic inversion model (WindTrax [194]) using meteorological measurements from a sonic anemometer located on site, the DCS concentration measurements provided methane and ammonia fluxes from ∼400 cattle that agreed with previous studies [237, 238]. One particularly attractive aspect of the DCS in this context is that the beam path can easily surround the facility when deployed through fiber but does not interfere with vehicle access or feed distribution, which will likely be a requirement of any long-term monitoring of a working agricultural site.

3.6 Volatile organic compound (VOC) measurements

Atmospheric VOCs are important from a public health perspective because some, like benzene, are regulated health hazards [239, 240]. Additionally, many are photochemically reactive and lead to increased O_3 production [241–246], which is another regulated health criteria pollutant. VOCs are emitted from a variety of sources [206, 241, 247, 248] including oil and gas operations [182, 249], forest fires [250–252], vehicle traffic [253], and industrial processes; however, the emissions strength from many of these sources is not well known. This makes developing efficient regulations challenging and highlights the need for additional measurements of VOCs. Many VOC measurements are made with point sensors, so DCS has the potential to make significant contributions to these measurements as the path-integrated measurements allow it to be less sensitive to location than point sensors, and it can measure along multiple beam paths to pick up emissions under varying wind directions as discussed in Sections 1.1 and 3.1.

As shown in Figure 4, an atmospheric transparency window exists between 3-4 μm. This range corresponds with the fundamental C-H vibrational stretch frequency, which enables sensitive measurements of organic species. However, as discussed in Section 2.3, laser systems in this region are more complex than the NIR systems used in the above applications. For the work shown here, DFG was used to produce comb

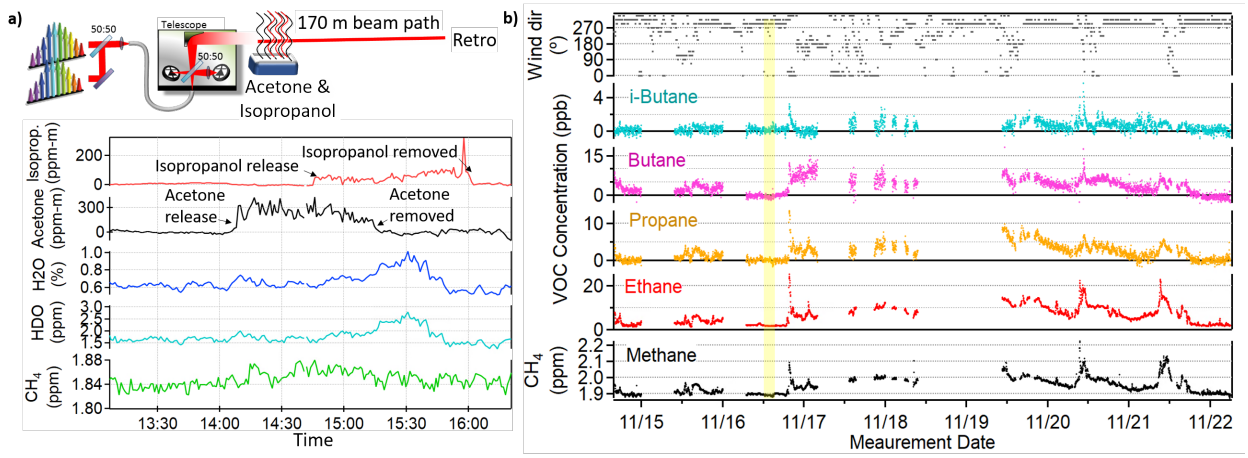

Figure 19: MIR DCS measurements. a) Setup and data from controlled release of acetone and isopropanol. b) Data from a week of measurements over a 1-km atmospheric path. The highlighted region indicates a region with flat concentration measurements that was used for sensitivity analysis.

light around 3 µm from light at 1 and 1.5 µm. The 1 and 1.5 µm branches originate from the same robust Er:fiber lasers used for the applications discussed above [99]. One of the challenges with measurements of organic species in this spectral region is that most species larger than ethane have spectra with only broad features, which makes it difficult to distinguish these features from spectral baseline variations as well as to identify many components in a mixture. Several ways of dealing with these challenges are discussed in more detail in Section 2.7.

Figure 19 shows results from two experiments using MIR DCS and is adapted from [67]. First, the ability to detect multiple VOCs was demonstrated with semi-controlled acetone and isopropanol releases over short (150-meter one-way) paths. For these measurements, change detection was used to deal with the spectral baseline (see Section 2.7). Trays of acetone and isopropanol were sequentially placed below the open beam path and then removed. As shown in 19a, acetone and isopropanol could be measured simultaneously with minimal crosstalk between retrieved concentrations as evidenced by the clear step changes in concentration as the trays are added and removed. The 1-σ sensitivities for 1-min averaging are 5.7 ppm-m for acetone and 2.4 ppm-m for isopropanol. However, it is also clear that change detection is not a perfect long-term solution as the noise at the end of the measurement period is substantially higher than the noise at the beginning of the measurement period. This is expected as the baseline drifts over several hours.

The system was also used to measure ethane and propane from oil and natural gas drilling over a 1-km path located on the western edge of Boulder, CO (this is the same as the red path in Figure 14). For these measurements, the DCS system was located in a laboratory. Data was collected for about one week with one large gap of several days due to poor weather. In order to determine VOC concentrations for the entire time period, the change-detection approach could not be used, so instead, a high-pass filter was used to remove the baseline from the spectra. The same filter was also applied to the reference cross sections before fitting (see Section 2.7). This approach reduces the VOC sensitivity because it removes most of the broad structure from the VOC spectrum; however, for ethane, propane, and isobutane the sensitivity was still high enough to observe concentration variation as shown in Figure 19. These species originate from primarily oil and natural gas extraction activities in the Denver-Julesburg basin [243, 249, 254–257], the edge of which is located ∼20-km east and north-east of Boulder. The VOC concentrations track changes in methane and are all enhanced when the wind is out of the east/north-east, which suggests that the majority of the measured methane enhancement arises from oil and gas activity as well. By using a time period when the wind is primarily bringing clean air out of the west (highlighted), the 1-σ sensitivities for 2-min averaging can be estimated to be 0.15 ppb (0.3 ppm-m) for ethane and 0.25 ppb (0.5 ppm-m) for propane and isobutane.

The DFG system used for the previous measurements provides high-power (∼100 mW), tunable MIR light but is too complex, is too large, and consumes too much power to work well as a fieldable system. A new design based on a waveguide PPLN has been demonstrated with significantly lower SWaP. This system

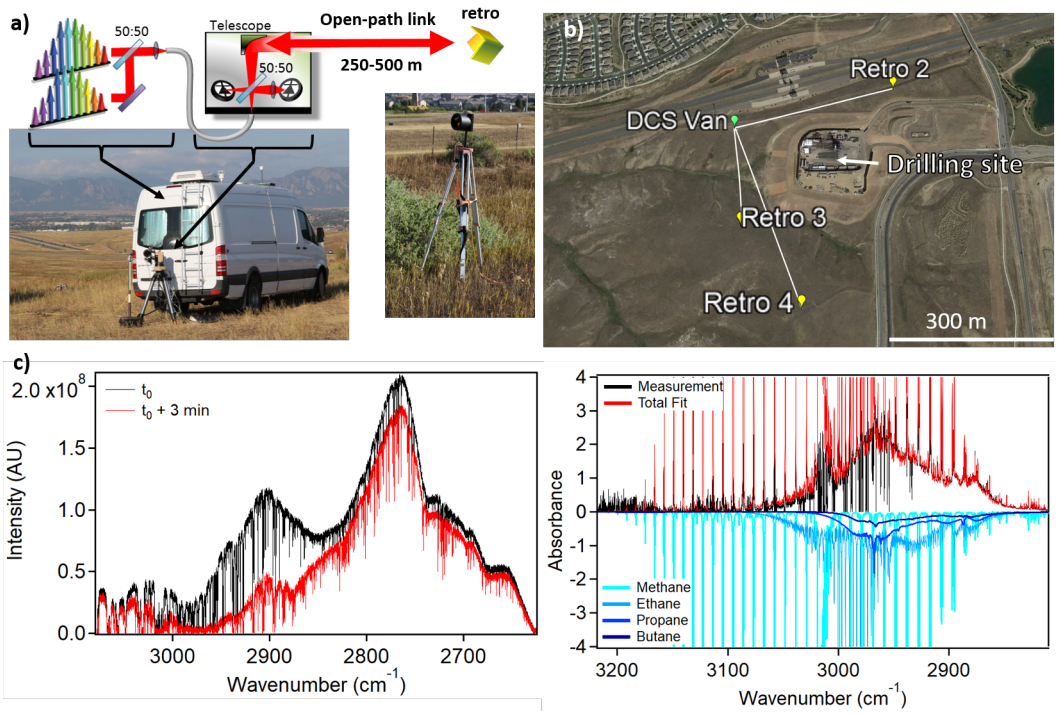

Figure 20: Setup and example spectra for measurements at an oil and gas drilling site outside of Denver, Colorado. a) The comb system is deployed in a van and connected via fiber to a telescope outside of the van. The light is launched from the telescope to a retroreflector on a tripod. b) Measurement site layout showing three DCS measurement paths to the north and west of the drilling site. Only one beam path was measured at a time. c) (left) Two DCS transmission spectra, separated by 3 minutes, taken before a plume event (black) and during a plume event (red). The significant drop in transmission at 3.3-3.5 µm is due to gas absorption in the plume. This absorbance is shown on the right in black and the sum of cross sections are shown in red. Individual absorption cross sections (from the PNNL IR database [159]) are shown inverted.

generates a few mW of light covering ∼3200-3900 nm (3100-2560 cm^{-1}) simultaneously, which covers most of the C-H stretch region. As a preliminary demonstration, this system has recently been deployed in a van at an active oil and gas drilling site in order to measure VOC emissions. An overview of the setup is shown in Figure 20a and b. Here the setup is based on the radial measurement configuration discussed in Section 3.1 and similar to that used for the oil and gas methane emissions measurements in Section 3.3. Three beam paths ranging from ∼250 m to ∼480 m one-way were set up to the north and west of the well pad to measure emitted VOCs when the winds were out of the south and east. During measurements, the telescope was toggled between different beam paths depending on the wind direction. Measurements were taken during the drilling, fracking, and mill out phases of hydraulic fracturing as well as the initial weeks of well production. Preliminary measurements from this system detected substantial plumes of methane and ethane from the well pad, including plumes of methane up to 19 ppm or ten times the regional background concentrations of methane. Figure 20c shows example spectra during one of these plume events. The left panel shows two measured transmission spectra collected on one path and separated by 3 minutes. During this time, a plume from the drilling operation crossed the beam path. Thus, the large difference between the two is due to absorption from gases emitted from the drilling site. This absorption is shown more clearly in the right panel where natural log of the ratio of the two transmission spectra is plotted. This absorption can be compared to the reference cross sections from the PNNL database [159], some of which are shown inverted in the bottom right panel. Absorption features from methane, ethane, propane, and butane can all be observed, indicating that the DCS system is capable of detecting multiple broad species simultaneously.

4 What is next in DCS based sensing?

4.1 Extending the spectral region beyond 1.5 μm and 3 μm

This section discusses possibilities for extending measurements outside of the narrow regions at 1.5 μm and 3 μm. Some regions are easier to access with existing technology than others, and some have greater applicability to atmospheric measurements than others.

Heading to ultraviolet and visible wavelengths, electronic transitions in molecules are typically very strong (as strong or stronger than fundamental vibrational transition) and thus can also provide very high sensitivity. While many of the electronic transitions are deep in the vacuum ultraviolet (10-200 nm), there are accessible transitions in the visible to ultraviolet for a number of molecules such as aromatics (240-300 nm), halogen oxides (280-500 nm), aldehydes (280-500 nm), NO_2 (300-500 nm), SO_2 (250-300 nm), O_3 (250-280 nm), OH (308 nm), and HONO (300-400 nm). Many of these species are measured using DOAS techniques; however, these techniques do have some limitations. Since most DOAS systems use grating spectrometers, they have low spectral resolution and must trade off spectral bandwidth for higher resolution, which limits the number of species that can be detected at once. While many absorption features in this region are broad, some species such as ClO, BrO, and especially OH have rotationally resolved spectra and thus benefit from high resolution. In addition, light sources for active DOAS systems in this spectral region have some challenges. These systems typically either use arc lamps, which are bulky, or LEDs, which have a limited bandwidth. In principle, open-path DCS could provide broad coverage across the entire 250-500 nm region with high spectral resolution, which is not possible with DOAS systems. The primary challenge though is generating broadband frequency comb light in the short-wave visible and ultraviolet. Some promising approaches have been demonstrated recently [125, 258–260]; however, more work is needed to develop efficient techniques using robust lasers and to push towards shorter wavelengths.

In the NIR, the 1.5 μm region has been described throughout this chapter, but the 2-2.5 μm spectral region has been relatively unexplored for atmospheric measurements. This is partially because generating broadband light in this region is not straightforward and partly because standard silica fiber results in significant attenuation past 2.3 μm. However, this region contains absorption for a number of species including CO_2, CH_4, NH_3, CO, weak N_2O, HCl, and HF as well as isotopologues of many of these species. One option to generate light in this region is to start with a 1.5 μm laser and broaden in highly non-linear fiber; however, it is difficult to cover the full spectral band and the broadening process typically results in significantly degraded RIN [261–263]. Tm:fiber lasers generate frequency combs around 2 μm, but spectral broadening in a specialty non-linear fiber is still required to cover the full spectral range. A promising approach based on Er:fiber combs has recently been demonstrated using spectral broadening in

silicon nitride photonic waveguides [97, 264], which results in significantly lower RIN than broadening in standard highly non-linear fiber. While these demonstrations so far have been confined to the laboratory, more robust coupling into and out of the waveguide should enable field applications soon.

In addition, the spectral region from 4.5-5 μm provides access to strong transitions from several important gases including the GHGs CO_2 and N_2O as well as criteria pollutants CO and O_3. As discussed in Section 3.5, N_2O measurements are important for understanding agricultural emissions. The ability to measure CO and CO_2 simultaneously would be a beneficial addition for the urban GHG emissions measurements discussed in Section 3.2 because CO is a tracer for combustion sources. By comparing excess CO and CO_2, it is possible to determine the fossil-fuel and biosphere contributions to the total CO_2 excess [265, 266]. This same method could also be used for understanding N_2O excess, which would help distinguish combustion and agricultural N_2O sources. For urban air quality studies, joint measurements of CO and O_3 could provide valuable information about the sources contributing to O_3, for example, by using CO to track the influence of wildfires on urban air quality [267]. Using the high-power DFG-based DCS system discussed in Section 3.6, we have recently demonstrated open-air measurements of all of these species across a 300-m-long one-way path (as well as a 1-km path) with estimated sensitivities of 1 ppm for CO_2, 1 ppb for N_2O, 7 ppb for CO, and 4 ppb for O_3 for a 2-minute averaging time. It is expected that further improvements to the system (such as in robustness and size) will lead to applications in monitoring urban air quality as well as in precision agriculture.

As evident from Section 3.6, there is a need for high sensitivity detection of VOCs; however, the presence of overlapping C-H vibrational bands from all species in the 3-4 μm region makes it difficult to identify many components in a complex spectrum. Thus, there is a need to continue to explore additional spectral regions. As shown in Figure 4, there is another atmospheric transparency window in the 10 μm spectral region. This window lies in the molecular fingerprint region where many fundamental stretching vibrations occur. These vibrational features are much more distinctive of specific molecules, which makes this region promising for mixture analysis. The same DFG concept used in our MIR system can be applied to make combs in this region; however, the crystals for doing efficient nonlinear wavelength conversion have not been as extensively developed for this wavelength region as compared to the 3-5 μm region. Recently, several frequency comb sources have been demonstrated in this spectral region using non-linear conversion of NIR combs (DFG and OPO) [64, 83, 268]. In addition, as discussed in Section 2.3, QCL combs have also been demonstrated in this region. However, for open-path DCS applications in the 10 μm spectral region, these sources still need to be further developed.

Finally, at even longer wavelengths, the terahertz or submillimeter region provides access to molecular rotational and low energy vibrational transitions. One intriguing aspect of THz radiation is that it is significantly less attenuated due to smoke or aerosol than shorter wavelength radiation. Several different methods for DCS in the THz region have been demonstrated [269–272]; however, there are significant technical challenges (e.g., beam launch and collection as well as efficient THz generation) that make open-path THz spectroscopy very difficult. Thus, it is likely that the best application of THz spectroscopy is as a point sensor or in the laboratory.

4.2 Instrument performance

All potential applications would benefit from DCS systems with reduced SWaP, thus, this is an active area of research. For example, the SWaP of traditional comb sources such as Er:fiber combs can be reduced by incorporating photonic waveguides for efficient spectral broadening [273] as well as by utilizing different locking schemes that do not require direct measurement of f_0 [274]. In addition, new comb sources with lower SWaP are being developed such as QCL-based combs, microresonator Kerr combs, and EO combs(Section 2.3).

Another future direction for open-path DCS is to push towards longer path lengths. As shown earlier, the fact that the frequency comb sources are bright and spatially coherent enabled one-way path lengths of several kilometers (Section 3.2); however, even longer path lengths would be beneficial for a variety of applications. For example, path lengths in excess of 10 km would enable monitoring of GHG emissions from larger cites. Even longer distances could enable vertical column measurements to a retroreflector on a weather balloon or high-altitude UAV or even satellite-to-ground or satellite-to-satellite column measurements. The primary challenge associated with longer path length is the reduction in collection efficiency. There are several

potential ways of overcoming this challenge. First, the collection efficiency can be improved by increasing the diameter of the receiver, decreasing the launched beam divergence, and increasing the diameter of the corner cube (see Section 2.4.1). Second, in some applications, it could be possible to convert to a one-way path by replacing the corner cube with a receiver (the bistatic configuration shown in Figure 5). Third, sending a single comb over the air could be beneficial as discussed in Section 2.4. Finally, a lower noise photodetector could be used. As shown in Figure 7 with a detector NEP of 10 pW/Hz$^{1/2}$, the measurement SNR is limited by detector noise at an incident power of ∼50 μW. By reducing the NEP to 1 pW/Hz$^{1/2}$, the same FOM could be obtained with about an order-of-magnitude lower incident power. As discussed in Section 2.5, this reduction could potentially be achieved with improved detection electronics or with an APD; however, the linearity and saturation performance of APDs need to be verified for use with DCS. With these improvements, path lengths of 10s of km or even 100s of km should be possible. Of course, increased path length also results in more challenging pointing requirements that will also need to be solved.

4.3 Data analysis

In addition to technical improvements, there are several future directions on the analysis side. First, as discussed some in Section 2.7, DCS presents a complex fitting challenge due to the simultaneous fit of the varying instrument baseline and absorption from multiple trace species. While the current fitting methods have already enabled many applications, improvements could still be made, especially in the areas of removing baseline structure and detecting multiple species with broad absorption features. These challenges also exist in FTS, so similar techniques could be applied to treat DCS data. For baseline removal, one possibility is to use Legendre polynomials instead of the current piece-wise polynomial functions. Legendre polynomials provide an orthogonal basis set and have been used with some success in various spectroscopy applications [275–278]. Another interesting direction would be to apply matrix deconvolution techniques such as principle component analysis or target factor analysis to the analysis of DCS data as has been done for FTIR data [279]. These methods have been used both to identify molecules in spectra [280, 281] and identify emissions sources [282, 283]. Another intriguing possibility is to try to obtain spatial information from open-path measurements. A potential technique for this – time gating – has been recently proposed and illustrated with laboratory measurements [284]. The high spectral resolution from DCS provides possibilities for extracting additional information from well-resolved spectral lines. For instance, it should be possible to determine vertical profiles of trace gases from vertical column measurements combined with a spectral inversion [285, 286].

As shown in Section 2.7, the accuracy of DCS is set by the spectral database used for analysis. DCS has the potential to assist with this in two ways. First, as the primary data product from DCS is a high-resolution spectrum (rather than a concentration), old data can be reanalyzed with new database and lineshape parameters to validate databases. Second, DCS can be used to obtain parameters for databases as has been discussed above [76, 149–152]. For example, there is a growing body of data indicating that the Voigt profile is insufficient for modeling strong lines, as a pure Voigt results in substantial residuals especially in high-resolution data [38, 158, 287, 288]. The Hartmann-Tran profile (also known as the 'partially Correlated quadratic-Speed-Dependent Nelkin-Ghatak profile') is now the recommended lineshape profile [158]. This profile requires several additional parameters beyond the Voigt profile. DCS is well-positioned to both provide and validate parameters for this profile because of the lack of instrument lineshape and the high spectral resolution. Another advantage of DCS is that the same instrument can be used both in the lab to measure reference gases in a multipass cell and in atmospheric air. Therefore, traceability between laboratory and ambient atmospheric data can be realized with the same instrument.

4.4 Summary

As outlined in this chapter, DCS is a very promising novel measurement method for open-path atmospheric sensing. It combines advantages of cw lasers, namely high spectral resolution and accuracy as well as low divergence optical probing, with broad spectral bandwidth approaching that of traditional thermal sources. As shown here, DCS sensing is already well established in the NIR and there is significant interest in extending it towards other wavelength ranges and to incorporate path-averaged DCS trace gas concentration measurements in field campaigns.

5 Acronyms

ADC analog-to-digital converter

APD avalanche photodiode

cw continuous-wave

DCS dual-comb spectroscopy

DFG difference frequency generation

DIAL differential absorption LIDAR

DOAS differential optical absorption spectroscopy

EO electro-optic

FOM figure of merit

FPGA field-programmable gate array

FTIR Fourier-transform infrared

FTS Fourier-transform spectroscopy

GHG greenhouse gas

ICL inter-band cascade laser

IGM interferogram

LED light emitting diode

LWIR long-wave infrared

MIR mid-infrared

NEP noise-equivalent power

NIR near-infrared

OAP off-axis parabolic mirror

OPO optical parametric oscillator

PBL planetary boundary layer

QCL quantum cascade laser

RIN relative intensity noise

SNR signal-to-noise ratio

SWaP size, weight, and power

TDLAS tunable diode laser absorption spectroscopy

UAV unmanned aerial vehicle

VOC volatile organic compound

References

(1) Cundiff, S. T.; Ye, J. *Reviews of Modern Physics* **2003**, *75*, 325–342.

(2) Telle, H. R.; Steinmeyer, G.; Dunlop, A. E.; Stenger, J.; Sutter, D. H.; Keller, U. *Applied Physics B* **1999**, *69*, 327–332.

(3) Reichert, J.; Holzwarth, R.; Udem, T.; Hänsch, T. W. *Optics Communications* **1999**, *172*, 59–68.

(4) Holzwarth, R.; Udem, T.; Hänsch, T. W.; Knight, J. C.; Wadsworth, W. J.; Russell, P. S. J. *Physical Review Letters* **2000**, *85*, 2264–2267.

(5) Diddams, S. A.; Jones, D. J.; Ye, J.; Cundiff, S. T.; Hall, J. L.; Ranka, J. K.; Windeler, R. S.; Holzwarth, R.; Udem, T.; Hänsch, T. W. *Physical Review Letters* **2000**, *84*, 5102–5105.

(6) Udem, T.; Diddams, S. A.; Vogel, K. R.; Oates, C. W.; Curtis, E. A.; Lee, W. D.; Itano, W. M.; Drullinger, R. E.; Bergquist, J. C.; Hollberg, L. *Physical Review Letters* **2001**, *86*, 4996–4999.

(7) Newbury, N. R. *Nature Photonics* **2011**, *5*, 186–188.

(8) Diddams, S. A. *Journal of the Optical Society of America B* **2010**, *27*, B51–B62.

(9) Fortier, T.; Baumann, E. *Communications Physics* **2019**, *2*, 1–16.

(10) Hall, J. L. *Reviews of Modern Physics* **2006**, *78*, 1279–1295.

(11) Hänsch, T. W. *Reviews of Modern Physics* **2006**, *78*, 1297–1309.

(12) Coddington, I.; Newbury, N.; Swann, W. *Optica* **2016**, *3*, 414–426.

(13) Adler, F.; Thorpe, M. J.; Cossel, K. C.; Ye, J. *Annual Review of Analytical Chemistry* **2010**, *3*, 175–205.

(14) Maslowski, P.; Cossel, K. C.; Foltynowicz, A.; Ye, J. In *Cavity-Enhanced Spectroscopy and Sensing*; Springer Berlin Heidelberg: 2014, pp 271–321.

(15) Weichman, M. L.; Changala, P. B.; Ye, J.; Chen, Z.; Yan, M.; Picqué, N. *Journal of Molecular Spectroscopy* **2019**, *355*, 66–78.

(16) Picqué, N.; Hänsch, T. W. *Nature Photonics* **2019**, *13*, 146–157.

(17) Flesch, T.; Harper, L.; Desjardins, R.; Gao, Z.; Crenna, B. *Boundary-Layer Meteorology* **2009**, *132*, 11–30.

(18) Schäfer, K.; Grant, R. H.; Emeis, S.; Raabe, A.; von der Heide, C.; Schmid, H. P. *Atmospheric Measurement Techniques* **2012**, *5*, 1571–1583.

(19) Lin, C.-H.; Grant, R. H.; Heber, A. J.; Johnston, C. T. *Atmospheric Measurement Techniques* **2019**, *12*, 3403–3415.

(20) Ciais, P.; Rayner, P.; Chevallier, F.; Bousquet, P.; Logan, M.; Peylin, P.; Ramonet, M. *Climatic Change* **2010**, *103*, 69–92.

(21) Marshall, T. L.; Chaffin, C. T.; Hammaker, R. M.; Fateley, W. G. *Environmental Science & Technology* **1994**, *28*, 224A–232A.

(22) Russwurm, G. M.; Childers, J. W. In *Handbook of Vibrational Spectroscopy*; John Wiley & Sons, Ltd: 2006, pp 1750–1773.

(23) Griffith, D. W. T.; Pöhler, D.; Schmitt, S.; Hammer, S.; Vardag, S. N.; Platt, U. *Atmospheric Measurement Techniques* **2018**, *11*, 1549–1563.

(24) Platt, U.; Perner, D. In *Optical and Laser Remote Sensing*, Killinger, D. D. K., Mooradian, D. A., Eds.; Springer Series in Optical Sciences 39; Springer Berlin Heidelberg: 1983, pp 97–105.

(25) Platt, U.; Stutz, J., *Differential Absorption Spectroscopy*; Physics of Earth and Space Environments; Springer Berlin Heidelberg: 2008.

(26) Stutz, J.; Wong, K. W.; Lawrence, L.; Ziemba, L.; Flynn, J. H.; Rappenglück, B.; Lefer, B. *Atmospheric Environment* **2010**, *44*, 4099–4106.

(27) Johnson, W.; Repasky, K. S.; Carlsten, J. L. *Applied Optics* **2013**, *52*, 2994–3003.

(28) Gibert, F.; Edouart, D.; Cénac, C.; Mounier, F. L.; Dumas, A. *Optics Letters* **2015**, *40*, 3093–3096.

(29) Wagner, G. A.; Plusquellic, D. F. *Applied Optics* **2016**, *55*, 6292–6310.

(30) Ku, R. T.; Hinkley, E. D.; Sample, J. O. *Applied Optics* **1975**, *14*, 854–861.

(31) Thoma, E. D.; Shores, R. C.; Thompson, E. L.; Harris, D. B.; Thorneloe, S. A.; Varma, R. M.; Hashmonay, R. A.; Modrak, M. T.; Natschke, D. F.; Gamble, H. A. *Journal of the Air & Waste Management Association* **2005**, *55*, 658–668.

(32) Nikodem, M.; Wysocki, G. *Sensors* **2012**, *12*, 16466–16481.

(33) Bailey, D. M.; Adkins, E. M.; Miller, J. H. *Applied Physics B* **2017**, *123*, 245.

(34) Kühnreich, B.; Wagner, S.; Habig, J. C.; Möhler, O.; Saathoff, H.; Ebert, V. *Applied Physics B* **2015**, *119*, 177–187.

(35) Seidel, A.; Wagner, S.; Dreizler, A.; Ebert, V. *Atmospheric Measurement Techniques* **2015**, *8*, 2061–2068.

(36) Sinclair, L. C.; Coddington, I.; Swann, W. C.; Rieker, G. B.; Hati, A.; Iwakuni, K.; Newbury, N. R. *Optics Express* **2014**, *22*, 6996–7006.

(37) Lezius, M. et al. *Optica* **2016**, *3*, 1381–1387.

(38) Waxman, E. M.; Cossel, K. C.; Truong, G.-W.; Giorgetta, F. R.; Swann, W. C.; Coburn, S.; Wright, R. J.; Rieker, G. B.; Coddington, I.; Newbury, N. R. *Atmospheric Measurement Techniques* **2017**, *10*, 3295–3311.

(39) Webb, E. K.; Pearman, G. I.; Leuning, R. *Quarterly Journal of the Royal Meteorological Society* **1980**, *106*, 85–100.

(40) Rella, C. W.; Chen, H.; Andrews, A. E.; Filges, A.; Gerbig, C.; Hatakka, J.; Karion, A.; Miles, N. L.; Richardson, S. J.; Steinbacher, M.; Sweeney, C.; Wastine, B.; Zellweger, C. *Atmospheric Measurement Techniques* **2013**, *6*, 837–860.

(41) Nara, H.; Tanimoto, H.; Tohjima, Y.; Mukai, H.; Nojiri, Y.; Katsumata, K.; Rella, C. W. *Atmospheric Measurement Techniques* **2012**, *5*, 2689–2701.

(42) Burba, G.; Anderson, T.; Komissarov, A. *Global Change Biology* **2019**, *25*, 2189–2202.

(43) Assan, S.; Baudic, A.; Guemri, A.; Ciais, P.; Gros, V.; Vogel, F. R. *Atmospheric Measurement Techniques* **2017**, *10*, 2077–2091.

(44) Reum, F.; Gerbig, C.; Lavric, J. V.; Rella, C. W.; Göckede, M. *Atmospheric Measurement Techniques* **2019**, *12*, 1013–1027.

(45) Warneke, C.; Veres, P.; Holloway, J. S.; Stutz, J.; Tsai, C.; Alvarez, S.; Rappenglueck, B.; Fehsenfeld, F. C.; Graus, M.; Gilman, J. B.; de Gouw, J. A. *Atmospheric Measurement Techniques* **2011**, *4*, 2345–2358.

(46) Lin, C.-H.; Grant, R. H.; Heber, A. J.; Johnston, C. T. *Atmospheric Measurement Techniques* **2020**, *13*, 2001–2013.

(47) Van der Weide, D.; Murakowski, J.; Keilmann, F. *IEEE Transactions on Microwave Theory and Techniques* **2000**, *48*, 740–743.

(48) Wu, Q.; Zhang, X.-C. *Applied Physics Letters* **1997**, *71*, 1285–1286.

(49) Leitenstorfer, A.; Hunsche, S.; Shah, J.; Nuss, M. C.; Knox, W. H. *Applied Physics Letters* **1999**, *74*, 1516–1518.

(50) Huber, R.; Brodschelm, A.; Tauser, F.; Leitenstorfer, A. *Applied Physics Letters* **2000**, *76*, 3191–3193.

(51) Schiller, S. *Optics Letters* **2002**, *27*, 766–768.

(52) Lee, S.-J.; Widiyatmoko, B.; Kourogi, M.; Ohtsu, M. *Japanese Journal of Applied Physics* **2001**, *40*, L878–L880.

(53) Keilmann, F.; Gohle, C.; Holzwarth, R. *Optics Letters* **2004**, *29*, 1542–1544.

(54) Schliesser, A.; Brehm, M.; Keilmann, F.; van der Weide, D. *Optics Express* **2005**, *13*, 9029–9038.

(55) Yasui, T.; Kabetani, Y.; Saneyoshi, E.; Yokoyama, S.; Araki, T. *Applied Physics Letters* **2006**, *88*, 241104.

(56) Coddington, I.; Swann, W. C.; Newbury, N. R. *Physical Review Letters* **2008**, *100*, 013902.

(57) Giaccari, P.; Deschênes, J.-D.; Saucier, P.; Genest, J.; Tremblay, P. *Optics Express* **2008**, *16*, 4347–4365.

(58) Baumann, E.; Giorgetta, F.; Coddington, I.; Swann, W.; Newbury, N. In *Conference on Lasers and Electro-Optics*, 2010, CMN5.

(59) Zolot, A. M.; Giorgetta, F. R.; Baumann, E.; Nicholson, J. W.; Swann, W. C.; Coddington, I.; Newbury, N. R. *Optics Letters* **2012**, *37*, 638–640.

(60) Boudreau, S.; Levasseur, S.; Perilla, C.; Roy, S.; Genest, J. *Optics Express* **2013**, *21*, 7411–7418.

(61) Rieker, G. B.; Giorgetta, F. R.; Swann, W. C.; Kofler, J.; Zolot, A. M.; Sinclair, L. C.; Baumann, E.; Cromer, C.; Petron, G.; Sweeney, C.; Tans, P. P.; Coddington, I.; Newbury, N. R. *Optica* **2014**, *1*, 290–298.

(62) Giorgetta, F. R.; Rieker, G. B.; Baumann, E.; Swann, W. C.; Sinclair, L. C.; Kofler, J.; Coddington, I.; Newbury, N. R. *Physical Review Letters* **2015**, *115*, 103901.

(63) Schroeder, P. J.; Wright, R. J.; Coburn, S.; Sodergren, B.; Cossel, K. C.; Droste, S.; Truong, G. W.; Baumann, E.; Giorgetta, F. R.; Coddington, I.; Newbury, N. R.; Rieker, G. B. *Proceedings of the Combustion Institute* **2017**, *36*, 4565–4573.

(64) Kara, O.; Maidment, L.; Gardiner, T.; Schunemann, P. G.; Reid, D. T. *Optics Express* **2017**, *25*, 32713–32721.

(65) Cossel, K. C.; Waxman, E. M.; Giorgetta, F. R.; Cermak, M.; Coddington, I. R.; Hesselius, D.; Ruben, S.; Swann, W. C.; Truong, G.-W.; Rieker, G. B.; Newbury, N. R. *Optica* **2017**, *4*, 724–728.

(66) Coburn, S.; Alden, C. B.; Wright, R.; Cossel, K.; Baumann, E.; Truong, G.-W.; Giorgetta, F.; Sweeney, C.; Newbury, N. R.; Prasad, K.; Coddington, I.; Rieker, G. B. *Optica* **2018**, *5*, 320–327.

(67) Ycas, G.; Giorgetta, F. R.; Cossel, K. C.; Waxman, E. M.; Baumann, E.; Newbury, N. R.; Coddington, I. *Optica* **2019**, *6*, 165–168.

(68) Waxman, E. M.; Cossel, K. C.; Giorgetta, F.; Truong, G.-W.; Swann, W. C.; Coddington, I.; Newbury, N. R. *Atmospheric Chemistry and Physics* **2019**, *19*, 4177–4192.

(69) Pinkowski, N. H.; Ding, Y.; Strand, C. L.; Hanson, R. K.; Horvath, R.; Geiser, M. *Measurement Science and Technology* **2020**, *31*, 055501.

(70) Martín-Mateos, P.; Khan, F. U.; Bonilla-Manrique, O. E. *Optica* **2020**, *7*, 199–202.

(71) Westberg, J.; Teng, C. C.; Chen, Y.; Liu, J.; Patrick, L.; Soskind, M.; Shen, L.; Wysocki, G. In *OSA Optical Sensors and Sensing Congress*, Vancouver, BC, 2020, EM1C.3.

(72) Nugent-Glandorf, L.; Giorgetta, F. R.; Diddams, S. A. *Applied Physics B* **2015**, *119*, 327–338.

(73) Zhu, F.; Xia, J.; Bicer, A.; Bounds, J.; Kolomenskii, A.; Strohaber, J.; Johnson, L.; Amani, M.; Schuessler, H. *Applied Optics* **2017**, *56*, 6311–6316.

(74) Kara, O.; Sweeney, F.; Rutkauskas, M.; Farrell, C.; Leburn, C. G.; Reid, D. T. *Optics Express* **2019**, *27*, 21358–21366.

(75) Lee, J.; Lee, K.; Yang, J.; Kim, Y.-J.; Kim, S.-W. *Optics Express* **2019**, *27*, 9088–9096.

(76) Zolot, A.; Giorgetta, F.; Baumann, E.; Swann, W.; Coddington, I.; Newbury, N. *Journal of Quantitative Spectroscopy and Radiative Transfer* **2013**, *118*, 26–39.

(77) Giorgetta, F. R.; Coddington, I.; Baumann, E.; Swann, W. C.; Newbury, N. R. *Nature Photonics* **2010**, *4*, 853–857.

(78) Sinclair, L. C.; Deschênes, J.-D.; Sonderhouse, L.; Swann, W. C.; Khader, I. H.; Baumann, E.; Newbury, N. R.; Coddington, I. *Review of Scientific Instruments* **2015**, *86*, 081301.

(79) Truong, G.-W.; Waxman, E. M.; Cossel, K. C.; Baumann, E.; Klose, A.; Giorgetta, F. R.; Swann, W. C.; Newbury, N. R.; Coddington, I. *Optics Express* **2016**, *24*, 30495–30504.

(80) Okubo, S.; Iwakuni, K.; Inaba, H.; Hosaka, K.; Onae, A.; Sasada, H.; Hong, F.-L. *Applied Physics Express* **2015**, *8*, 082402.

(81) Muraviev, A. V.; Smolski, V. O.; Loparo, Z. E.; Vodopyanov, K. L. *Nature Photonics* **2018**, *12*, 209–214.

(82) Ycas, G.; Giorgetta, F.; Baumann, E.; Coddington, I. R.; Herman, D.; Diddams, S.; Newbury, N. In, OSA: 2017, JTh5A.10.

(83) Timmers, H.; Kowligy, A.; Lind, A.; Cruz, F. C.; Nader, N.; Silfies, M.; Ycas, G.; Allison, T. K.; Schunemann, P. G.; Papp, S. B.; Diddams, S. A. *Optica* **2018**, *5*, 727–732.

(84) Droste, S.; Ycas, G.; Washburn, B. R.; Coddington, I.; Newbury, N. R. *Nanophotonics* **2016**, *5*, 196–213.

(85) Lee, J.; Lee, K.; Jang, Y.-S.; Jang, H.; Han, S.; Lee, S.-H.; Kang, K.-I.; Lim, C.-W.; Kim, Y.-J.; Kim, S.-W. *Scientific Reports* **2014**, *4*, 5134.

(86) Fermann, M. E.; Hartl, I. *IEEE J. Sel. Topics in Quantum Electron.* **2009**, *15*, 191–206.

(87) Fermann, M. E.; Hartl, I. *Nature Photonics* **2013**, *7*, 868–874.

(88) Ruehl, A.; Marcinkevicius, A.; Fermann, M. E.; Hartl, I. *Optics Letters* **2010**, *35*, 3015–3017.

(89) Adler, F.; Diddams, S. A. *Optics Letters* **2012**, *37*, 1400–1402.

(90) Fortier, T. M.; Jones, D. J.; Cundiff, S. T. *Optics Letters* **2003**, *28*, 2198–2200.

(91) Fortier, T. M.; Bartels, A.; Diddams, S. A. *Optics Letters* **2006**, *31*, 1011–1013.

(92) Matos, L.; Kleppner, D.; Kuzucu, O.; Schibli, T. R.; Kim, J.; Ippen, E. P.; Kaertner, F. X. *Optics Letters* **2004**, *29*, 1683–1685.

(93) Sorokin, E.; Naumov, S.; Sorokina, I. *IEEE Journal of Selected Topics in Quantum Electronics* **2005**, *11*, 690–712.

(94) Bernhardt, B.; Sorokin, E.; Jacquet, P.; Thon, R.; Becker, T.; Sorokina, I. T.; Picqué, N.; Hänsch, T. W. *Applied Physics B* **2010**, *100*, 3–8.

(95) Vasilyev, S.; Smolski, V.; Peppers, J.; Moskalev, I.; Mirov, M.; Barnakov, Y.; Mirov, S.; Mirov, S.; Gapontsev, V. *Optics Express* **2019**, *27*, 35079–35087.

(96) Guo, H.; Herkommer, C.; Billat, A.; Grassani, D.; Zhang, C.; Pfeiffer, M. H. P.; Weng, W.; Brès, C.-S.; Kippenberg, T. J. *Nature Photonics* **2018**, 1.

(97) Baumann, E.; Hoenig, E. V.; Perez, E. F.; Colacion, G. M.; Giorgetta, F. R.; Cossel, K. C.; Ycas, G.; Carlson, D. R.; Hickstein, D. D.; Srinivasan, K.; Papp, S. B.; Newbury, N. R.; Coddington, I. *Optics Express* **2019**, *27*, 11869–11876.

(98) Zhu, F.; Bicer, A.; Askar, R.; Bounds, J.; Kolomenskii, A. A.; Kelessides, V.; Amani, M.; Schuessler, H. A. *Laser Physics Letters* **2015**, *12*, 095701.

(99) Ycas, G.; Giorgetta, F. R.; Baumann, E.; Coddington, I.; Herman, D.; Diddams, S. A.; Newbury, N. R. *Nature Photonics* **2018**, *12*, 202–208.

(100) Adler, F.; Cossel, K. C.; Thorpe, M. J.; Hartl, I.; Fermann, M. E.; Ye, J. *Optics Letters* **2009**, *34*, 1330–1332.

(101) Leindecker, N.; Marandi, A.; Byer, R. L.; Vodopyanov, K. L. *Optics Express* **2011**, *19*, 6296.

(102) Abbas, M. A.; Pan, Q.; Mandon, J.; Cristescu, S. M.; Harren, F. J. M.; Khodabakhsh, A. *Scientific Reports* **2019**, *9*, 1–9.

(103) Faist, J.; Villares, G.; Scalari, G.; Rösch, M.; Bonzon, C.; Hugi, A.; Beck, M. *Nanophotonics* **2016**, *5*, 272–291.

(104) Villares, G.; Hugi, A.; Blaser, S.; Faist, J. *Nature Communications* **2014**, *5*, 5192.

(105) Westberg, J.; Sterczewski, L. A.; Wysocki, G. *Applied Physics Letters* **2017**, *110*, 141108.

(106) Yang, Y.; Burghoff, D.; Hayton, D. J.; Gao, J.-R.; Reno, J. L.; Hu, Q. *Optica* **2016**, *3*, 499–502.

(107) Sterczewski, L. A.; Westberg, J.; Bagheri, M.; Frez, C.; Vurgaftman, I.; Canedy, C. L.; Bewley, W. W.; Merritt, C. D.; Kim, C. S.; Kim, M.; Meyer, J. R.; Wysocki, G. *Optics Letters* **2019**, *44*, 2113–2116.

(108) Klocke, J. L.; Mangold, M.; Allmendinger, P.; Hugi, A.; Geiser, M.; Jouy, P.; Faist, J.; Kottke, T. *Analytical Chemistry* **2018**, *90*, 10494–10500.

(109) Burghoff, D.; Yang, Y.; Hu, Q. *Science Advances* **2016**, *2*, e1601227.

(110) Sterczewski, L. A.; Sterczewski, L. A.; Sterczewski, L. A.; Westberg, J.; Wysocki, G. *Optics Express* **2019**, *27*, 23875–23893.

(111) Maas, D.; Bellancourt, A.-R.; Rudin, B.; Golling, M.; Unold, H.; Südmeyer, T.; Keller, U. *Applied Physics B* **2007**, *88*, 493–497.

(112) Link, S. M.; Maas, D. J. H. C.; Waldburger, D.; Keller, U. *Science* **2017**, *356*, 1164–1168.

(113) Long, D. A.; Fleisher, A. J.; Douglass, K. O.; Maxwell, S. E.; Bielska, K.; Hodges, J. T.; Plusquellic, D. F. *Optics Letters* **2014**, *39*, 2688–2690.

(114) Martin-Mateos, P.; Ruiz-Llata, M.; Posada-Roman, J.; Acedo, P. *IEEE Photonics Technology Letters* **2015**, *27*, 1309–1312.

(115) Fleisher, A. J.; Long, D. A.; Reed, Z. D.; Hodges, J. T.; Plusquellic, D. F. *Optics Express* **2016**, *24*, 10424.

(116) Millot, G.; Pitois, S.; Yan, M.; Hovhannisyan, T.; Bendahmane, A.; Hänsch, T. W.; Picqué, N. *Nature Photonics* **2016**, *10*, 27–30.

(117) Martín-Mateos, P.; Jerez, B.; Largo-Izquierdo, P.; Acedo, P. *Optics Express* **2018**, *26*, 9700–9713.

(118) Carlson, D. R.; Hickstein, D. D.; Zhang, W.; Metcalf, A. J.; Quinlan, F.; Diddams, S. A.; Papp, S. B. *Science* **2018**, *361*, 1358–1363.

(119) Yan, M.; Luo, P.-L.; Iwakuni, K.; Millot, G.; Hänsch, T. W.; Picqué, N. *Light: Science & Applications* **2017**, *6*, e17076.

(120) Guay, P.; Genest, J.; Fleisher, A. J. *Optics Letters* **2018**, *43*, 1407–1410.

(121) Fdil, K.; Michaud-Belleau, V.; Hébert, N. B.; Guay, P.; Fleisher, A. J.; Deschênes, J.-D.; Genest, J. *Optics Letters* **2019**, *44*, 4415–4418.

(122) Jerez, B.; Martín-Mateos, P.; Walla, F.; de Dios, C.; Acedo, P. *ACS Photonics* **2018**, *5*, 2348–2353.

(123) Kippenberg, T. J.; Gaeta, A. L.; Lipson, M.; Gorodetsky, M. L. *Science* **2018**, *361*, eaan8083.

(124) Kippenberg, T. J.; Holzwarth, R.; Diddams, S. A. *Science* **2011**, *332*, 555–559.

(125) Lee, S. H.; Oh, D. Y.; Yang, Q.-F.; Shen, B.; Wang, H.; Yang, K. Y.; Lai, Y.-H.; Yi, X.; Li, X.; Vahala, K. *Nature Communications* **2017**, *8*, 1295.

(126) Yu, M.; Okawachi, Y.; Griffith, A. G.; Lipson, M.; Gaeta, A. L. *Optica* **2016**, *3*, 854.

(127) Herr, T.; Brasch, V.; Jost, J. D.; Wang, C. Y.; Kondratiev, N. M.; Gorodetsky, M. L.; Kippenberg, T. J. *Nature Photonics* **2014**, *8*, 145–152.

(128) Suh, M.-G.; Yang, Q.-F.; Yang, K. Y.; Yi, X.; Vahala, K. J. *Science* **2016**, *354*, 600–603.

(129) Pavlov, N. G.; Lihachev, G.; Koptyaev, S.; Lucas, E.; Karpov, M.; Kondratiev, N. M.; Bilenko, I. A.; Kippenberg, T. J.; Gorodetsky, M. L. *Optics Letters* **2017**, *42*, 514–517.

(130) Dutt, A.; Joshi, C.; Ji, X.; Cardenas, J.; Okawachi, Y.; Luke, K.; Gaeta, A. L.; Lipson, M. *Science Advances* **2018**, *4*, e1701858.

(131) Yu, M.; Okawachi, Y.; Griffith, A. G.; Picqué, N.; Lipson, M.; Gaeta, A. L. *Nature Communications* **2018**, *9*, 1869.

(132) Gaeta, A. L.; Lipson, M.; Kippenberg, T. J. *Nature Photonics* **2019**, *13*, 158.

(133) Plusquellic, D. F.; Wagner, G. A.; Fleisher, A. J.; Long, D. A.; Hodges, J. T. In *Conference on Lasers and Electro-Optics (2017), Paper AM1A.5*, Optical Society of America: 2017, AM1A.5.

(134) Alden, C. B.; Coburn, S. C.; Wright, R. J.; Baumann, E.; Cossel, K.; Perez, E.; Hoenig, E.; Prasad, K.; Coddington, I.; Rieker, G. B. *Environmental Science & Technology* **2019**, *53*, 2908–2917.

(135) Siegman, A. E., *Lasers*; University Science Books: 1986.

(136) Fante, R. L. *Proceedings of the IEEE* **1975**, *63*, 1669–1692.

(137) Andrews, L. C.; Al-Habash, M. A.; Hopen, C. Y.; Phillips, R. L. *Waves in Random Media* **2001**, *11*, 271–291.

(138) Andrews, L. C.; Phillips, R. L., *Laser Beam Propagation through Random Media*, Second; SPIE: Bellingham, WA, 2005.

(139) Cole, W. P.; Marciniak, M. A.; Haeri, M. B. *Optical Engineering* **2008**, *47*, 126001-126001–11.

(140) Cole, W. P.; Marciniak, M. A. *Applied Optics* **2009**, *48*, 4256.

(141) Newbury, N. R.; Coddington, I.; Swann, W. C. *Optics Express* **2010**, *18*, 7929–7945.

(142) Griffiths, P. R.; Haseth, J. A., *Fourier Transform Infrared Spectrometry*; Wiley-Interscience: 2007.

(143) Roy, J.; Deschênes, J.-D.; Potvin, S.; Genest, J. *Optics Express* **2012**, *20*, 21932–21939.

(144) Hall, J.; Zhu, M. In *Laser Manipulation of Atoms and Ions/Manipolazione Col Laser Di Atomi E Ioni (Proceedings of the International School of Physics), 'Enrico Fermi' Course*; North-Holland: 1993; Vol. CXVIII.

(145) Coddington, I.; Swann, W. C.; Newbury, N. R. *Optics Letters* **2009**, *34*, 2153–2155.

(146) Coddington, I.; Swann, W. C.; Newbury, N. R. *Phys. Rev. A* **2010**, *82*, 043817.

(147) Ideguchi, T.; Poisson, A.; Guelachvili, G.; Picqué, N.; Hänsch, T. W. *Nature Communications* **2014**, *5*, 3375.

(148) Burghoff, D.; Han, N.; Shin, J. H. *Optics Letters* **2019**, *44*, 2966–2969.

(149) Baumann, E.; Giorgetta, F. R.; Swann, W. C.; Zolot, A. M.; Coddington, I.; Newbury, N. R. *Physical Review A* **2011**, *84*, 062513.

(150) Schroeder, P. J.; Pfotenhauer, D. J.; Yang, J.; Giorgetta, F. R.; Swann, W. C.; Coddington, I.; Newbury, N. R.; Rieker, G. B. *Journal of Quantitative Spectroscopy and Radiative Transfer* **2017**, *203*, 194–205.

(151) Schroeder, P. J.; Cich, M. J.; Yang, J.; Swann, W. C.; Coddington, I.; Newbury, N. R.; Drouin, B. J.; Rieker, G. B. *Physical Review A* **2017**, *96*, 022514.

(152) Schroeder, P. J.; Cich, M. J.; Yang, J.; Giorgetta, F. R.; Swann, W. C.; Coddington, I.; Newbury, N. R.; Drouin, B. J.; Rieker, G. B. *Journal of Quantitative Spectroscopy and Radiative Transfer* **2018**, *210*, 240–250.

(153) McClatchey, R. A.; Benedict, W. S.; Clough, S. A.; Burch, D. E.; Calfee, R. F.; Fox, K.; Rothman, L. S.; Garing, J. S. *Optical Physics Laboratory, Project 7670. Environmental Research Papers No. 434. AFCRL-TR-73-0096. 78 pages.* **1973**.

(154) Rothman, L. S.; Gamache, R. R.; Goldman, A.; Brown, L. R.; Toth, R. A.; Pickett, H. M.; Poynter, R. L.; Flaud, J.-M.; Camy-Peyret, C.; Barbe, A.; Husson, N.; Rinsland, C. P.; Smith, M. A. H. *Applied Optics* **1987**, *26*, 4058–4097.

(155) Gordon, I. E. et al. *Journal of Quantitative Spectroscopy and Radiative Transfer* **2017**, *203*, 3–69.

(156) Rothman, L. S. et al. *Journal of Quantitative Spectroscopy and Radiative Transfer* **2009**, *110*, 533–572.

(157) Rothman, L. S. et al. *Journal of Quantitative Spectroscopy and Radiative Transfer* **2013**, *130*, 4–50.

(158) Tennyson, J. et al. *Pure and Applied Chemistry* **2014**, *86*, 1931–1943.

(159) Sharpe, S. W.; Johnson, T. J.; Sams, R. L.; Chu, P. M.; Rhoderick, G. C.; Johnson, P. A. *Applied Spectroscopy* **2004**, *58*, 1452–1461.

(160) Childers, D.; Skinner, D.; Kemerait, R. *Proceedings of the IEEE* **1977**, *65*, 1428–1443.

(161) Cole, R. K.; Makowiecki, A. S.; Hoghooghi, N.; Rieker, G. B. *Optics Express* **2019**, *27*, 37920.

(162) Disclaimer The Use of Tradenames in This Manuscript Is Necessary to Specify Experimental Results and Does Not Imply Endorsement by the National Institute of Standards and Technology.

(163) Tans, P.; Zellweger, C. *18th WMO/IAEA Meeting on Carbon Dioxide, Other Greenhouse Gases and Related Tracers Measurement Techniques*; GAW 229; La Jolla, CA, USA, 2015, p 137.

(164) Bergeron, H.; Sinclair, L. C.; Swann, W. C.; Nelson, C. W.; Deschênes, J.-D.; Baumann, E.; Giorgetta, F. R.; Coddington, I.; Newbury, N. R. *Optica* **2016**, *3*, 441.

(165) Sinclair, L. C.; Swann, W. C.; Bergeron, H.; Baumann, E.; Cermak, M.; Coddington, I.; Deschênes, J.-D.; Giorgetta, F. R.; Juarez, J. C.; Khader, I.; Petrillo, K. G.; Souza, K. T.; Dennis, M. L.; Newbury, N. R. *Applied Physics Letters* **2016**, *109*, 151104.

(166) Denmead, O. T. *Plant and Soil* **2008**, *309*, 5–24.

(167) Feitz, A. et al. *International Journal of Greenhouse Gas Control* **2018**, *70*, 202–224.

(168) Baldocchi, D. D.; Hincks, B. B.; Meyers, T. P. *Ecology* **1988**, *69*, 1331–1340.

(169) Baldocchi, D. et al. *Bulletin of the American Meteorological Society* **2001**, *82*, 2415–2434.

(170) Nemitz, E.; Hargreaves, K. J.; McDonald, A. G.; Dorsey, J. R.; Fowler, D. *Environmental Science & Technology* **2002**, *36*, 3139–3146.

(171) Velasco, E.; Perrusquia, R.; Jiménez, E.; Hernández, F.; Camacho, P.; Rodríguez, S.; Retama, A.; Molina, L. T. *Atmospheric Environment* **2014**, *97*, 226–238.

(172) Wilson, J. D.; Flesch, T. K. *Agricultural and Forest Meteorology* **2016**, *220*, 170–176.

(173) Flesch, T. K.; Baron, V. S.; Wilson, J. D.; Griffith, D. W. T.; Basarab, J. A.; Carlson, P. J. *Agricultural and Forest Meteorology* **2016**, *221*, 111–121.

(174) Lamb, B.; Westberg, H.; Allwine, G. *Atmospheric Environment (1967)* **1986**, *20*, 1–8.

(175) Lamb, B. K.; McManus, J. B.; Shorter, J. H.; Kolb, C. E.; Mosher, B.; Harriss, R. C.; Allwine, E.; Blaha, D.; Howard, T.; Guenther, A.; Lott, R. A.; Siverson, R.; Westburg, H.; Zimmerman, P. *Environmental Science & Technology* **1995**, *29*, 1468–1479.

(176) Czepiel, P. M.; Mosher, B.; Harriss, R. C.; Shorter, J. H.; McManus, J. B.; Kolb, C. E.; Allwine, E.; Lamb, B. K. *Journal of Geophysical Research: Atmospheres* **1996**, *101*, 16711–16719.

(177) Allen, D. T.; Torres, V. M.; Thomas, J.; Sullivan, D. W.; Harrison, M.; Hendler, A.; Herndon, S. C.; Kolb, C. E.; Fraser, M. P.; Hill, A. D.; Lamb, B. K.; Miskimins, J.; Sawyer, R. F.; Seinfeld, J. H. *Proceedings of the National Academy of Sciences* **2013**, *110*, 17768–17773.

(178) Roscioli, J. R.; Yacovitch, T. I.; Floerchinger, C.; Mitchell, A. L.; Tkacik, D. S.; Subramanian, R.; Martinez, D. M.; Vaughn, T. L.; Williams, L.; Zimmerle, D.; Robinson, A. L.; Herndon, S. C.; Marchese, A. J. *Atmospheric Measurement Techniques* **2015**, *8*, 2017–2035.

(179) Marchese, A. J.; Vaughn, T. L.; Zimmerle, D. J.; Martinez, D. M.; Williams, L. L.; Robinson, A. L.; Mitchell, A. L.; Subramanian, R.; Tkacik, D. S.; Roscioli, J. R.; Herndon, S. C. *Environmental Science & Technology* **2015**, *49*, 10718–10727.

(180) Thoma, E. D.; DeWees, J. *Draft Other Test Method 33A: Geospatial Measurement of Air Pollution, Remote Emissions Quantification - Direct Assessment*; EPA Draft Other Test Method; Air Emissions Measurement Center: Environmental Protection Agency, 2014.

(181) Brantley, H. L.; Thoma, E. D.; Squier, W. C.; Guven, B. B.; Lyon, D. *Environmental Science & Technology* **2014**, *48*, 14508–14515.

(182) Brantley, H. L.; Thoma, E. D.; Eisele, A. P. *Journal of the Air & Waste Management Association* **2015**, *65*, 1072–1082.

(183) Robertson, A. M.; Edie, R.; Snare, D.; Soltis, J.; Field, R. A.; Burkhart, M. D.; Bell, C. S.; Zimmerle, D.; Murphy, S. M. *Environmental Science & Technology* **2017**, DOI: `10.1021/acs.est.7b00571`.

(184) Crenna, B. P.; Flesch, T. K.; Wilson, J. D. *Atmospheric Environment* **2008**, *42*, 7373–7383.

(185) Flesch, T. K.; Wilson, J. D.; Yee, E. *Journal of Applied Meteorology* **1995**, *34*, 1320–1332.

(186) Humphries, R.; Jenkins, C.; Leuning, R.; Zegelin, S.; Griffith, D.; Caldow, C.; Berko, H.; Feitz, A. *Environmental Science & Technology* **2012**, *46*, 1739–1746.

(187) Bréon, F. M.; Broquet, G.; Puygrenier, V.; Chevallier, F.; Xueref-Remy, I.; Ramonet, M.; Dieudonné, E.; Lopez, M.; Schmidt, M.; Perrussel, O.; Ciais, P. *Atmos. Chem. Phys.* **2015**, *15*, 1707–1724.

(188) Nathan, B. J.; Lauvaux, T.; Turnbull, J. C.; Richardson, S. J.; Miles, N. L.; Gurney, K. R. *Journal of Geophysical Research: Atmospheres* **2018**, *123*, 13, 611–13, 621.

(189) Nickless, A.; Rayner, P. J.; Engelbrecht, F.; Brunke, E.-G.; Erni, B.; Scholes, R. J. *Atmospheric Chemistry and Physics* **2018**, *18*, 4765–4801.

(190) Wu, K.; Lauvaux, T.; Davis, K. J.; Deng, A.; Coto, I. L.; Gurney, K. R.; Patarasuk, R. *Elementa: Science of the Anthropocene* **2018**, *6*, DOI: `10.1525/elementa.138`.

(191) Wilson, J. D.; Flesch, T. K.; Harper, L. A. *Agricultural and Forest Meteorology* **2001**, *107*, 207–225.

(192) Järvi, L.; Rannik, Ü.; Kokkonen, T. V.; Kurppa, M.; Karppinen, A.; Kouznetsov, R. D.; Rantala, P.; Vesala, T.; Wood, C. R. *Atmospheric Measurement Techniques* **2018**, *11*, 5421–5438.

(193) Bell, C.; Vaughn, T.; Zimmerle, D.; Herndon, S.; Yacovitch, T.; Heath, G.; Pétron, G.; Edie, R.; Field, R.; Murphy, S.; Robertson, A.; Soltis, J. *Elementa: Science of the Anthropocene* **2017**, *5*, DOI: `10.1525/elementa.266`.

(194) Flesch, T. K.; Wilson, J. D.; Harper, L. A.; Crenna, B. P.; Sharpe, R. R. *Journal of Applied Meteorology* **2004**, *43*, 487–502.

(195) Bai, M.; Suter, H.; Lam, S. K.; Sun, J.; Chen, D. *Atmospheric Environment* **2014**, *94*, 687–691.

(196) Ni, K.; Köster, J. R.; Seidel, A.; Pacholski, A. *European Journal of Agronomy* **2015**, *71*, 115–122.

(197) Alden, C. B.; Ghosh, S.; Coburn, S.; Sweeney, C.; Karion, A.; Wright, R.; Coddington, I.; Rieker, G. B.; Prasad, K. *Atmospheric Measurement Techniques* **2018**, *11*, 1565–1582.

(198) Cartwright, L.; Zammit-Mangion, A.; Bhatia, S.; Schroder, I.; Phillips, F.; Coates, T.; Negandhi, K.; Naylor, T.; Kennedy, M.; Zegelin, S.; Wokker, N.; Deutscher, N. M.; Feitz, A. *Atmospheric Measurement Techniques* **2019**, *12*, 4659–4676.

(199) Hirst, B.; Randell, D.; Jones, M.; Jonathan, P.; King, B.; Dean, M. *Energy Procedia* **2017**, *114*, 3716–3728.

(200) Bai, M.; Suter, H.; Lam, S. K.; Flesch, T. K.; Chen, D. *Atmospheric Measurement Techniques* **2019**, *12*, 1095–1102.

(201) Hashmonay, R. A.; Natschke, D. F.; Wagoner, K.; Harris, D. B.; Thompson, E. L.; Yost, M. G. *Environmental Science & Technology* **2001**, *35*, 2309–2313.

(202) Todd, L. A.; Ramanathan, M.; Mottus, K.; Katz, R.; Dodson, A.; Mihlan, G. *Atmospheric Environment* **2001**, *35*, 1937–1947.

(203) Hartl, A.; Song, B. C.; Pundt, I. *Atmospheric Chemistry and Physics* **2006**, *6*, 847–861.

(204) Dobler, J. T.; Zaccheo, T. S.; Pernini, T. G.; Blume, N.; Broquet, G.; Vogel, F.; Ramonet, M.; Braun, M.; Staufer, J.; Ciais, P.; Botos, C. *Journal of Applied Remote Sensing* **2017**, *11*, 014002.

(205) Lian, J.; Bréon, F.-M.; Broquet, G.; Zaccheo, T. S.; Dobler, J.; Ramonet, M.; Staufer, J.; Santaren, D.; Xueref-Remy, I.; Ciais, P. *Atmospheric Chemistry and Physics* **2019**, *19*, 13809–13825.

(206) Seinfeld, J. H.; Pandis, S. N., *Atmospheric Chemistry and Physics: From Air Pollution to Climate Change*; Wiley: 2006.

(207) Vardoulakis, S.; Fisher, B. E. A.; Pericleous, K.; Gonzalez-Flesca, N. *Atmospheric Environment* **2003**, *37*, 155–182.

(208) Caputo, M.; Giménez, M.; Schlamp, M. *Atmospheric Environment* **2003**, *37*, 2435–2449.

(209) Holmes, N. S.; Morawska, L. *Atmospheric Environment* **2006**, *40*, 5902–5928.

(210) Leelőssy, Á.; Lagzi, I.; Kovács, A.; Mészáros, R. *Journal of Environmental Radioactivity* **2018**, *182*, 20–33.

(211) Turner, D. B. Workbook of Atmospheric Dispersion Estimates, 1970.

(212) Lin, J. C.; Gerbig, C.; Wofsy, S. C.; Andrews, A. E.; Daube, B. C.; Davis, K. J.; Grainger, C. A. *Journal of Geophysical Research: Atmospheres* **2003**, *108*, DOI: 10.1029/2002JD003161.

(213) Fasoli, B.; Lin, J. C.; Bowling, D. R.; Mitchell, L.; Mendoza, D. *Geoscientific Model Development* **2018**, *11*, 2813–2824.

(214) Marcotullio, P. J.; Sarzynski, A.; Albrecht, J.; Schulz, N.; Garcia, J. *Climatic Change* **2013**, *121*, 621–634.

(215) Seto, K. C.; Bigio, A.; Bento, A.; Cervero, R.; Christensen, P. In *Climate Change 2014: Mitigation of Coimate Change. Contribution of Working Group III to the Fifth Assessment Report of the Intergovernmental Panel on Climate Change*, 2014, p 78.

(216) Davis, K. J. et al. *Elementa: Science of the Anthropocene* **2017**, *5*, 21.

(217) McKain, K.; Wofsy, S. C.; Nehrkorn, T.; Eluszkiewicz, J.; Ehleringer, J. R.; Stephens, B. B. *Proceedings of the National Academy of Sciences* **2012**, *109*, 8423–8428.

(218) Shusterman, A. A.; Teige, V. E.; Turner, A. J.; Newman, C.; Kim, J.; Cohen, R. C. *Atmospheric Chemistry and Physics* **2016**, *16*, 13449–13463.

(219) Karion, A.; Callahan, W.; Stock, M.; Prinzivalli, S.; Verhulst, K. R.; Kim, J.; Salameh, P. K.; Lopez-Coto, I.; Whetstone, J. *Earth System Science Data* **2020**, *12*, 699–717.

(220) Harriss, R.; Alvarez, R. A.; Lyon, D.; Zavala-Araiza, D.; Nelson, D.; Hamburg, S. P. *Environmental Science & Technology* **2015**, *49*, 7524–7526.

(221) Zavala-Araiza, D. et al. *Proceedings of the National Academy of Sciences* **2015**, *112*, 15597–15602.

(222) Nathan, B. J.; Golston, L. M.; O'Brien, A. S.; Ross, K.; Harrison, W. A.; Tao, L.; Lary, D. J.; Johnson, D. R.; Covington, A. N.; Clark, N. N.; Zondlo, M. A. *Environmental Science & Technology* **2015**, *49*, 7896–7903.

(223) Alvarez, R. A. et al. *Science* **2018**, 186–188.

(224) Lavoie, T. N.; Shepson, P. B.; Cambaliza, M. O. L.; Stirm, B. H.; Conley, S.; Mehrotra, S.; Faloona, I. C.; Lyon, D. *Environmental Science & Technology* **2017**, *51*, 8001–8009.

(225) Alden, C. B.; Wright, R. J.; Coburn, S. C.; Caputi, D.; Wendland, G.; Rybchuk, A.; Conley, S.; Faloona, I.; Rieker, G. B. *in review* **2020**.

(226) Zhou, X.; Amaral, V.; Albertson, J. D. In *2017 IEEE International Conference on Big Data (Big Data)*, 2017, pp 4621–4629.

(227) van Kessel, T. G.; Ramachandran, M.; Klein, L. J.; Nair, D.; Hinds, N.; Hamann, H.; Sosa, N. E. In *2018 IEEE SENSORS*, 2018, pp 1–4.

(228) Ravikumar, A. P.; Sreedhara, S.; Wang, J.; Englander, J.; Roda-Stuart, D.; Bell, C.; Zimmerle, D.; Lyon, D.; Mogstad, I.; Ratner, B.; Brandt, A. R. *Elementa: Science of the Anthropocene* **2019**, *7*, 37.

(229) Desjardins, R. L.; Denmead, O. T.; Harper, L.; McBain, M.; Massé, D.; Kaharabata, S. *Atmospheric Environment* **2004**, *38*, 6855–6866.

(230) Gao, Z.; Desjardins, R. L.; Flesch, T. K. *Agricultural and Forest Meteorology* **2009**, *149*, 891–898.

(231) IPCC, *Climate Change 2013: The Physical Science Basis. Contribution of Working Group I to the Fifth Assessment Report of the Intergovernmental Panel on Climate Change*; Cambridge University Press: Cambridge, UK and New York, NY, USA, 2013.

(232) 2019 Refinement to the 2006 IPCC Guidelines for National Greenhouse Gas Inventories, https://www.ipcc-nggip.iges.or.jp/public/2019rf/index.html.

(233) Agency, U. E. P. *EPA430-R-10-001* **2019**.

(234) EPA **2019**.

(235) Prajapati, P.; Santos, E. A. *Agricultural and Forest Meteorology* **2018**, *258*, 18–28.

(236) Hénault, C.; Grossel, A.; Mary, B.; Roussel, M.; Léonard, J. *Pedosphere* **2012**, *22*, 426–433.

(237) Todd, R. W.; Cole, N. A.; Rhoades, M. B.; Parker, D. B.; Casey, K. D. *Journal of Environmental Quality* **2011**, *40*, 1090–1095.

(238) Todd, R. W.; Altman, M. B.; Cole, N. A.; Waldrip, H. M. *Journal of Environmental Quality* **2014**, *43*, 1125–1130.

(239) McMullin, T. S.; Bamber, A. M.; Bon, D.; Vigil, D. I.; Van Dyke, M. *International Journal of Environmental Research and Public Health* **2018**, *15*, 1500.

(240) McKenzie, L. M.; Blair, B.; Hughes, J.; Allshouse, W. B.; Blake, N. J.; Helmig, D.; Milmoe, P.; Halliday, H.; Blake, D. R.; Adgate, J. L. *Environmental Science & Technology* **2018**, DOI: 10.1021/acs.est.7b05983.

(241) von Schneidemesser, E.; Monks, P. S.; Allan, J. D.; Bruhwiler, L.; Forster, P.; Fowler, D.; Lauer, A.; Morgan, W. T.; Paasonen, P.; Righi, M.; Sindelarova, K.; Sutton, M. A. *Chemical Reviews* **2015**, *115*, 3856–3897.

(242) Atkinson, R. *Atmospheric Environment. Part A. General Topics* **1990**, *24*, 1–41.

(243) McDuffie, E. E. et al. *Journal of Geophysical Research: Atmospheres* **2016**, *121*, 8712–8729.

(244) Abeleira, A. J.; Farmer, D. K. *Atmospheric Chemistry and Physics* **2017**, *17*, 6517–6529.

(245) Cheadle, L. C.; Oltmans, S. J.; Petron, G.; Schnell, R. C.; Mattson, E. J.; Herndon, S. C.; Thompson, A. M.; Blake, D. R.; McClure-Begley, A. *Elementa: Science of the Anthropocene* **2017**, *5*, 61.

(246) Bien, T.; Helmig, D. *Elementa: Science of the Anthropocene* **2018**, *6*, 55.

(247) Watson, J. G.; Chow, J. C.; Fujita, E. M. *Atmospheric Environment* **2001**, *35*, 1567–1584.

(248) Field, R. A.; Goldstone, M. E.; Lester, J. N.; Perry, R. *Atmospheric Environment. Part A. General Topics* **1992**, *26*, 2983–2996.

(249) Gilman, J. B.; Lerner, B. M.; Kuster, W. C.; de Gouw, J. A. *Environmental Science & Technology* **2013**, *47*, 1297–1305.

(250) Goode, J. G.; Yokelson, R. J.; Susott, R. A.; Ward, D. E. *Journal of Geophysical Research: Atmospheres* **1999**, *104*, 21237–21245.

(251) Wooster, M. J.; Freeborn, P. H.; Archibald, S.; Oppenheimer, C.; Roberts, G. J.; Smith, T. E. L.; Govender, N.; Burton, M.; Palumbo, I. *Atmospheric Chemistry and Physics* **2011**, *11*, 11591–11615.

(252) Christian, T. J.; Kleiss, B.; Yokelson, R. J.; Holzinger, R.; Crutzen, P. J.; Hao, W. M.; Shirai, T.; Blake, D. R. *Journal of Geophysical Research: Atmospheres* **2004**, *109*, DOI: 10.1029/2003JD003874.

(253) Ammoura, L.; Xueref-Remy, I.; Gros, V.; Baudic, A.; Bonsang, B.; Petit, J.-E.; Perrussel, O.; Bonnaire, N.; Sciare, J.; Chevallier, F. *Atmospheric Chemistry and Physics* **2014**, *14*, 12871–12882.

(254) Pétron, G. et al. *Journal of Geophysical Research: Atmospheres* **2014**, *119*, 2013JD021272.

(255) Abeleira, A.; Pollack, I. B.; Sive, B.; Zhou, Y.; Fischer, E. V.; Farmer, D. K. *Journal of Geophysical Research: Atmospheres* **2017**, *122*, 3595–3613.

(256) Tzompa-Sosa, Z. A. et al. *Journal of Geophysical Research: Atmospheres* **2019**, *124*, 1148–1169.

(257) Helmig, D. *Elem Sci Anth* **2020**, *8*, 4.

(258) Yoon Oh, D.; Yang, K. Y.; Fredrick, C.; Ycas, G.; Diddams, S. A.; Vahala, K. J. *Nature Communications* **2017**, *8*, 13922.

(259) Ravi, A.; Beck, M.; Phillips, D. F.; Bartels, A.; Sasselov, D.; Szentgyorgyi, A.; Walsworth, R. L. *Journal of Lightwave Technology* **2018**, *36*, 5309–5315.

(260) Fan, R.; Wu, C.-L.; Lin, Y.-Y.; Liu, C.-Y.; Hwang, P.-S.; Liu, C.-W.; Qiao, J.; Shih, M.-H.; Hung, Y.-J.; Chiu, Y.-J.; Chu, A.-K.; Lee, C.-K. *Optics Letters* **2019**, *44*, 1512–1515.

(261) Newbury, N. R.; Washburn, B. R.; Corwin, K. L.; Windeler, R. S. *Optics Letters* **2002**, *28*, 944–946.

(262) Corwin, K. L.; Newbury, N. R.; Dudley, J. M.; Coen, S.; Diddams, S. A.; Washburn, B. R.; Weber, K.; Windeler, R. S. *Applied Physics B* **2003**, *77*, 269–277.

(263) Corwin, K. L.; Newbury, N. R.; Dudley, J. M.; Coen, S.; Diddams, S. A.; Weber, K.; Windeler, R. S. *Physical Review Letters* **2003**, *90*, 113904.

(264) Guo, H.; Weng, W.; Liu, J.; Yang, F.; Hansel, W.; Bres, C. S.; Thevenaz, L.; Holzwarth, R.; Kippenberg, T. J. *arXiv e-prints* **2019**, arXiv:1908.00871.

(265) Newman, S.; Jeong, S.; Fischer, M. L.; Xu, X.; Haman, C. L.; Lefer, B.; Alvarez, S.; Rappenglueck, B.; Kort, E. A.; Andrews, A. E.; Peischl, J.; Gurney, K. R.; Miller, C. E.; Yung, Y. L. *Atmospheric Chemistry and Physics* **2013**, *13*, 4359–4372.

(266) Turnbull, J. C.; Sweeney, C.; Karion, A.; Newberger, T.; Lehman, S. J.; Tans, P. P.; Davis, K. J.; Lauvaux, T.; Miles, N. L.; Richardson, S. J.; Cambaliza, M. O.; Shepson, P. B.; Gurney, K.; Patarasuk, R.; Razlivanov, I. *Journal of Geophysical Research: Atmospheres* **2015**, *120*, 292–312.

(267) Jaffe, D. A.; Wigder, N. L. *Atmospheric Environment* **2012**, *51*, 1–10.

(268) Iwakuni, K.; Porat, G.; Bui, T. Q.; Bjork, B. J.; Schoun, S. B.; Heckl, O. H.; Fermann, M. E.; Ye, J. *Applied Physics B* **2018**, *124*, 128.

(269) Good, J. T.; Holland, D. B.; Finneran, I. A.; Carroll, P. B.; Kelley, M. J.; Blake, G. A. *Review of Scientific Instruments* **2015**, *86*, 103107.

(270) Finneran, I. A.; Good, J. T.; Holland, D. B.; Carroll, P. B.; Allodi, M. A.; Blake, G. A. *Physical Review Letters* **2015**, *114*, 163902.

(271) Jerez, B.; Walla, F.; Betancur, A.; Martín-Mateos, P.; de Dios, C.; Acedo, P. *Optics Letters* **2019**, *44*, 415–418.

(272) Scalari, G.; Faist, J.; Picqué, N. *Applied Physics Letters* **2019**, *114*, 150401.

(273) Manurkar, P.; Perez, E. F.; Hickstein, D. D.; Carlson, D. R.; Chiles, J.; Westly, D. A.; Baumann, E.; Diddams, S. A.; Newbury, N. R.; Srinivasan, K.; Papp, S. B.; Coddington, I. *OSA Continuum* **2018**, *1*, 274–282.

(274) Guay, P.; Tourigny-Plante, A.; Bourbeau Hébert, N.; Michaud-Belleau, V.; Larouche, S.; Fdil, K.; Genest, J. *arXiv e-prints* **2019**, arXiv:1909.09715.

(275) Lipkus, A. H. *Applied Spectroscopy* **1988**, *42*, 395–400.

(276) Cadet, F. *Spectroscopy Letters* **1996**, *29*, 937–951.

(277) Wunch, D.; Toon, G. C.; Sherlock, V.; Deutscher, N. M.; Liu, C.; Feist, D. G.; Wennberg, P. O. **2015**, DOI: `10.14291/tccon.ggg2014.documentation.r0/1221662`.

(278) Frankenberg, C.; Köhler, P.; Magney, T. S.; Geier, S.; Lawson, P.; Schwochert, M.; McDuffie, J.; Drewry, D. T.; Pavlick, R.; Kuhnert, A. *Remote Sensing of Environment* **2018**, *217*, 523–536.

(279) Saarinen, P.; Kauppinen, J. *Applied Spectroscopy* **1991**, *45*, 953–963.

(280) Bangalore, A. S.; Small, G. W.; Combs, R. J.; Knapp, R. B.; Kroutil, R. T. *Analytica Chimica Acta* **1994**, *297*, 387–403.

(281) Shao, L.; Griffiths, P. R. *Analytical Chemistry* **2007**, *79*, 2118–2124.

(282) Chang, P.-E. P.; Yang, J.-C. R.; Den, W.; Wu, C.-F. *Environmental Science and Pollution Research* **2014**, *21*, 10852–10866.

(283) Yang, J.-C.; Chang, P.-E.; Chie, W.-C.; Liu, J.-P.; Wu, C.-F. *Process Safety and Environmental Protection* **2016**, *104*, 382–394.

(284) Chen, X.; Zhang, W.; Zhang, Y.; Lu, M.; Li, Y.; Wei, H. *Sensors* **2020**, *20*, 1566.

(285) Connor, B. J.; Sherlock, V.; Toon, G.; Wunch, D.; Wennberg, P. O. *Atmospheric Measurement Techniques* **2016**, *9*, 3513–3525.

(286) Ramanathan, A. K.; Nguyen, H. M.; Sun, X.; Mao, J.; Abshire, J. B.; Hobbs, J. M.; Braverman, A. J. *Atmospheric Measurement Techniques* **2018**, *11*, 4909–4928.

(287) Long, D. A.; Bielska, K.; Lisak, D.; Havey, D. K.; Okumura, M.; Miller, C. E.; Hodges, J. T. *J. Chem. Phys.* **2011**, *135*, 064308.

(288) Bui, T. Q.; Long, D. A.; Cygan, A.; Sironneau, V. T.; Hogan, D. W.; Rupasinghe, P. M.; Ciuryło, R.; Lisak, D.; Okumura, M. *The Journal of Chemical Physics* **2014**, *141*, 174301.